

Inferring Axon Diameters Using Magnetic Resonance Imaging
Oscillating Gradient Spin Echo Sequences

by

Sheryl Lyn Herrera

A thesis submitted to the Faculty of Graduate Studies of
The University of Manitoba
in partial fulfilment of the requirements of the degree of

DOCTOR OF PHILOSOPHY

Department of Physics & Astronomy
University of Manitoba
Winnipeg

Copyright © 2018 Sheryl Lyn Herrera

Abstract

A new diffusion magnetic resonance imaging method was developed and optimized to probe the smallest structures to date ($0.54 \pm 0.06 \mu\text{m}$), micron-sized tissue structures, such as small axon diameters (AxD). This method relies on probing the shortest possible diffusion time scales.

Current temporal diffusion spectroscopy methods cannot distinguish small structures because the pulse sequences limit the ability to probe the shortest diffusion times. This method circumvents those limitations using oscillating gradients in lieu of pulsed gradients and will have important neuroscience applications such as probing AxD distributions. The required imaging time will need to be shortened in order for the method to be clinically useful.

The thesis presents three sets of experiments that guided the selection of pulse sequence and imaging parameters needed for measuring micron-sized restrictions. Measurements were made on water diffusing between $3 \mu\text{m}$ polystyrene spheres. The gradient frequencies and amplitudes used were appropriate to infer the pore sizes between the $3 \mu\text{m}$ beads while the fit results indicated a better signal-to-noise ratio would help make the results more accurate. Measurements made on water diffusing inside various tubes indicated the gradient frequency range was not appropriate for inferences of tube diameters that were $250 \mu\text{m}$ and larger.

The second set of experiments used information from the first set to choose imaging and gradient parameters for measurements of water diffusing between 3 , 6 , and $10 \mu\text{m}$ beads and $150 \mu\text{m}$ tubes. Pore sizes, surface-to-volume ratio and diameters could be inferred from these samples with this method. The results indicated that the method had a resolution limit which is greater than $0.5 \mu\text{m}$ given that the pore sizes between the $3 \mu\text{m}$ and $6 \mu\text{m}$ beads were indistinguishable.

The more accurate inferences of diameters of the bead rather than diameters of the tubes suggest the method is better optimized for micron-sized samples rather than 150 μm -sized samples.

The final experiment tested the method on human corpus callosum. The results suggest that the resolution limit of the method needs to be decreased and careful attention to the axon direction would be needed. Suggestions for improvements to the model are made.

Acknowledgements

I would first like to thank Dr. Melanie Martin for taking me on as an undergraduate student, and for continuing to do so for my graduate studies. You have been a great mentor, and friend, and I thank you for all the support, advice, headaches and laughter for all these years.

To my committee members: Dr. Esmat Elhami, Dr. Francis Lin, and Dr. Doug Goltz, thank you for agreeing to be part of my committee, and for all the guidance and encouragement you have given me all of these years. Thank you to Dr. Marty Pagel for agreeing to be my external examiner, and for providing me with a lot of helpful information for this project and in my dissertation.

Many thanks to Dr. Richard Buist for teaching me how to operate the magnet and for your role in enhancing my knowledge and understanding of MRI.

To my fellow lab members past and present, thank you for all your help and advice: Morgan Mercredi, Vanessa Palmer, Dr. Jonathan Thiessen, Trevor Vincent. I would especially like to thank Morgan for running all the simulations and the performing all the curve fitting for my experiments.

Thank you to Dr. Doug Craig, Dr. Doug Goltz, and Dr. Dom Di Curzio for your assistance with helping me prepare my phantoms. Thank you also to Dr. Kant Matsuda for allowing us to use the human brain sample, for help with its preparation for MRI, and for performing the electron microscopy needed for the experiment.

Thank you to the administrative staff and faculty in the Department of Physics and Astronomy for your guidance throughout my studies. To the faculty of the Department of Physics at the University of Winnipeg, many thanks for all of your support and encouragement.

Funding for this project was provided by the Natural Sciences and Engineering Council of Canada, Canadian Foundation for Innovation, Research Manitoba, the University of Winnipeg, and the University of Manitoba. I am also appreciative of the McCrorie-West Family Fellowship for Alzheimer Research for funding my education.

Last, but most importantly, thank you to my friends, and Teddy, who have put up with all of my crazy and for continuing to do so. And lastly, to my parents and brother for your love, support and patience in allowing me to pursue the things that drive me.

Contents

Abstract	iii
Acknowledgments	v
Contents	vii
List of Figures	xiii
List of Tables	xv
1. Introduction	1
1.1 Axons	1
1.2 Rationale for this Study	3
1.3 Goals	7
1.4 Thesis Organization	9
References	11
2. Magnetic Resonance Imaging - Basics and Related Imaging Sequences	15
2.1 Nuclear Magnetic Resonance	15
2.1.1 Nuclear Magnetic Moments	16
2.1.2 Bulk Magnetization	22
2.1.3 Net Magnetization Vector	25
2.1.4 Inhomogeneities in the Magnetic Field	27
2.2 Magnetic Resonance Signal	28
2.2.1 Radio-Frequency Pulse	28
2.2.2 Rotating Frame of Reference	30
2.2.3 Bloch Equation	32
2.2.4 Flip Angle	35
2.3 Free Induction Decay	37
2.4 Signal Detection	38

2.5	Gradients	40
2.5.1	Slice Selective Gradients	42
2.5.2	Phase Encoding Gradients	47
2.5.3	Frequency Encoding Gradients	48
2.6	Relaxation	50
2.7	Pulse Sequences	55
2.7.1	Spin Echo.....	57
2.7.2	T ₂ -weighting	61
2.8	k-space Data Acquisition and Image Reconstruction	62
	References	67
3.	Diffusion	69
3.1	Diffusion of Water in the Body.....	69
3.2	Diffusion-Weighted Imaging	70
3.2.1	Self-Diffusion	71
3.2.2	Isotropic, Anisotropic, Unrestricted and Restricted Diffusion	72
3.2.3	Bloch-Torrey Equation	75
3.2.4	Pulsed Gradient Spin Echo	78
3.3	Apparent Diffusion Coefficient, Diffusion Anisotropy, Diffusion Tensor	83
3.3.1	Apparent Diffusion Coefficient	84
3.3.2	Mean Diffusivity	84
3.3.3	Diffusion Tensor.....	85
3.3.4	Fractional Anisotropy	87
3.4	Temporal Diffusion Spectroscopy	88
3.4.1	AxCaliber Method	89
3.4.2	ActiveAx Method	91
3.5	Oscillating Gradient Spin Echo (OGSE)	92
3.5.1	Short Diffusion Times in the PGSE	93
3.5.2	Oscillating Gradient Spin Echo Sequences	94
3.5.3	Temporal Diffusion Spectroscopy with OGSE	96

3.5.4	Connected Spherical Pore Extracellular Model.....	98
3.5.5	Short-Time or High Frequency Model	101
References	103
4.	First OGSE Diffusion Spectroscopy Experiments	107
4.1	Methods	108
4.1.1	Description of the Samples.....	109
4.1.1.1	3 μm Beads.....	109
4.1.1.2	Microcapillary Pipettes.....	110
4.1.1.3	Microfluidic Device	111
4.1.2	MRI Parameters.....	112
4.1.2.1	Bead Phantom Parameters.....	113
4.1.2.2	Tube Phantom Parameters.....	114
4.1.2.3	Microfluidic Device Parameters.....	114
4.1.3	Image Registration.....	115
4.1.4	Image Analysis	117
4.1.4.1	Bead Phantom Analysis.....	117
4.1.4.2	Tube Phantom Analysis.....	118
4.1.4.3	Microfluidic Device Analysis	118
4.1.5	Signal Extraction and Fit	119
4.1.5.1	Bead Phantoms Fit.....	120
4.1.5.2	Tubes Phantom and Microfluidic Device Fits.....	121
4.2	Results	121
4.2.1	Bead Phantom Results	121
4.2.2	Tube Phantom Results	122
4.2.3	Microfluidic Device Results.....	123
4.3	Discussion	124
4.3.1	Preparation of the Smaller Tube Phantom.....	125
4.3.1.1	Filling the Tubing (First Attempt).....	125
4.3.1.2	Filling the Tubing (Second Attempt)	126

4.4	Conclusions	128
	References	129
5.	Inferring Diameters of Spheres and Cylinders using Extracellular Water	131
5.1	Methods	133
5.1.1	Description of the Samples	134
5.1.1.1	3 μm Beads	135
5.1.1.2	6 and 10 μm Beads	135
5.1.1.3	Microcapillary Tubing	136
5.1.2	MRI parameters	138
5.1.2.1	3 μm Bead Phantom Parameters	138
5.1.2.2	6 and 10 μm Bead Phantom Parameters	138
5.1.2.3	Tube Phantom Parameters	139
5.1.3	Image Registration	140
5.1.4	Image Analysis	140
5.1.4.1	3 μm Bead Phantom Analysis	141
5.1.4.2	6 and 10 μm Bead Phantom Analysis	142
5.1.4.3	Tube Phantom Analysis	143
5.1.5	Signal Extraction and Fit	144
5.1.5.1	Bead Phantoms Fit	144
5.1.5.2	Tube Phantom Fit	145
5.2	Results	145
5.2.1	Bead Phantoms Results	145
5.2.2	Tube Phantom Results	149
5.3	Discussion	151
5.4	Conclusion	155
	References	157

6.	Axon Diameter Measurements in the Human Corpus Callosum using OGSE	161
6.1	Background	161
6.2	Methods	163
6.2.1	Tissue Sample Preparation	164
6.2.2	MRI Parameters.....	165
6.2.3	Image Registration.....	166
6.2.4	Image Analysis	167
6.2.5	Signal Extraction and Fit	168
6.2.6	Histology	168
6.3	Results	171
6.3.1	MR/Fit Results.....	171
6.3.2	Histology Results.....	172
6.4	Discussion	173
6.5	Conclusions	175
	References	177
7.	Conclusions and Future Directions	179
7.1	Conclusions	179
7.2	Improvements for Future Experiments	181
7.2.1	A Water Tube	181
7.2.2	Evaporation of Water.....	182
7.2.3	Temperature.....	183
7.2.4	Securing the Sample in the Magnet Bore	183
7.2.5	Monitoring Sample and Imaging throughout Experiment.....	184
7.2.6	Preparation of the Bead Phantom	185
7.2.7	Preparation of the Tube Phantom	186
7.2.8	Resolution Limit of the Method	189
7.2.9	Preparation of the Brain Sample.....	190
7.2.10	Improvements of the Coding in the Pulse Sequence.....	191
7.2.11	Quality Assurance	192

7.2.12	Considerations for Live Brain Experiments.....	192
7.3	Improvements to the Model	193
7.3.1	Axon Orientation Dispersion and Axon Undulation	193
7.3.2	Shortening Imaging Time Toward a Clinically Relevant Time	194
7.3.3	Diffusion Tensor Imaging (DTI)	195
7.4	Final Conclusions.....	196
References	197
List of Abbreviations		199
List of Symbols		201
Appendix A	203
A.1	Schematic of Experimental Setup.....	203
Appendix B	204
B.1	Calculation of Points.....	204
B.1.1	Bead Phantoms and Microfluidic Device.....	206
B.1.2	Microcapillary Pipettes.....	207
B.1.3	Tube Phantom.....	208
B.1.4	Corpus Callosum	209

List of Figures

1.1	Neuron diagram	2
1.2	Axon diagram.....	3
2.1	Proton spin	17
2.2	Orientation of nuclear magnetic moment vectors	20
2.3	Precession of the nuclear magnetic moment.....	20
2.4	Zeeman splitting for a spin-1/2 system with B_0	23
2.5	RF Pulses for rectangle and sinc envelope functions.....	30
2.6	Precession of net magnetization in rotating and laboratory frames	32
2.7	Flip angle	35
2.8	Net magnetization vector in the rotating frame	36
2.9	FID signal.....	39
2.10	Parameters characterizing slice where image is perpendicular to x,y,z-axes ...	42
2.11	Slice thickness determined by bandwidth size at fixed gradient strength	44
2.12	Slice thickness determined by gradient strength at fixed bandwidth.....	45
2.13	Fixed slice thickness, increased gradient strength with increased bandwidth ..	45
2.14	Slice selective gradient pulse at $\frac{1}{2}$ -time of 90° pulse duration	46
2.15	Image gradients for slice select, frequency-encoding, phase-encoding.....	47
2.16	Magnetic moments return to thermal equilibrium and then to M_z	51
2.17	T_1 curve where $M_z(0) = 0$	52
2.18	Spin- spin interactions cause the magnetic moments to dephase	53
2.19	T_2 -decay curve for the magnetization after a 90° pulse	54
2.20	Spin echo sequence	58
2.21	T_1 -, T_2 -, PD-weighted images of a mouse (<i>in vivo</i> and <i>ex vivo</i>)	60
2.22	k-space diagram	65
3.1	T_2 -weighted and Diffusion-weighted images of a mouse in <i>ex vivo</i>	70
3.2	Diffusion of a molecule	73
3.3	Diffusion of a molecule (Einstein's Relation)	74
3.4	Pulse gradient spin echo sequence	79
3.5	Diffusion ellipsoid. Ellipsoid representations of anisotropy.....	86
3.6	PGSE vs OGSE.....	95
3.7	Pulse sequence diagrams: sine, ideal cosine and apodised-cosine waves	97
3.8	Tetrahedral and octahedral holes	100
3.9	CCP and HCP close packed structures	101
4.1	General outline of methods used for each experiment.....	108
4.2	3 μm bead phantom.....	110
4.3	Tube phantom	111
4.4	Microfluidic device.....	112
4.5	Image registration	116
4.6	ROIs in the 3 μm bead phantom	117
4.7	ROIs in the tube phantom	118
4.8	ROIs in the microfluidic device.....	119

4.9	Diffusion spectrum for the bead phantom	122
4.10	Diffusion spectrum for the tube phantom	123
4.11	Preparation of tube sample (attempt 1).....	126
4.12	Preparation of tube sample (attempt 2).....	127
5.1	General outline of methods used for each experiment.....	134
5.2	6 and 10 μm bead phantom.....	136
5.3	Tube phantom (microcapillary tubing)	137
5.4	ROIs in the 3 μm bead phantom	141
5.5	ROIs in the 6 and 10 μm bead phantoms.....	142
5.6	ROIs in the tube phantoms.....	143
5.7	Diffusion spectrum for 3, 6 and 10 μm bead phantoms.....	146
5.8	Pore radius vs. bead radius.....	148
5.9	Diffusion spectrum for the tube sample.....	149
5.10	SNR in the 6 and 10 μm bead phantoms (signal intensity)	152
6.1	General outline of methods used in the experiment.....	163
6.2	Human corpus callosum tissue sample	164
6.3	MR slice selection in tissue sample and images	166
6.4	Regions of interest drawn on the corpus callosum sample	167
6.5	Slice selection for electron microscopy for the corpus callosum sample	169
6.6	Measurements of axon diameters taken on the EM images.....	170

List of Tables

2.1	Difference $N_{\uparrow} - N_{\downarrow}$ for magnetic fields at 1.5, 3.0, 7.0, 11.7 T	25
2.2	Difference $N_{\uparrow} - N_{\downarrow}$ in ppm for magnetic fields at 1.5, 3.0, 7.0, 11.7 T.....	26
2.3	Effect of TR and TE for a spin echo image	59
5.1	Inferred bead pore radius, and corresponding diameters	147
5.2	Inferred S/V ratios, tube diameters, and diffusion coefficients of water	150
6.1	Measurements from EM images of axon diameters	170
6.2	Fitted AxD for each ROI in humans brain sample	172
6.3	Second set of measurements from EM images of axon diameters	173
B.1.1	Bead Phantoms and Microfluidic Device	206
B.1.2	Microcapillary Pipettes	207
B.1.3	Tube Phantom	208
B.1.4	Corpus Callosum.....	209

Chapter 1

Introduction

In this thesis a new magnetic resonance imaging (MRI) method was developed and optimized to probe the smallest structures to date. This introductory chapter covers the goals and rationale of this work including why MRI was chosen as the imaging method, and the format of this thesis. The final chapter in this thesis describes the ideas for moving this method to the clinic for use in the diagnosis and understanding of many central nervous system diseases discussed in this chapter.

1.1 Axons

Neurons, or nerve cells are an important part of the central nervous system which are responsible for receiving sensory input. Each neuron consists of three main parts; the axon, cell body and dendrites (Figure 1.1). The cell body is where the nucleus lies, housing most of the neuron's DNA and where proteins are made to be transported throughout the axon and dendrites. A dendrite is where the neuron receives input from other cells, receiving the synaptic inputs from the axons, with the sum total of dendritic inputs determining whether the neuron will fire an action potential. Axons are long, threadlike projections which serve as the output structure of the neuron, sending electrical messages called action potentials throughout the entire axon. The axon is the transmitting part of the neuron. Within the axon, action potentials are generated. These action potentials travel through the axon causing the release of neurotransmitters or

chemical messengers which transmit the signals across the gaps between the neurons [1].

Myelin is the fatty substance that surrounds the axons and acts like an insulating layer, allowing for the transmission of signals over long distances from the brain and spine. Between the axons lies the Nodes of Ranvier, or myelin sheath gaps, which occur along a myelinated axon. Nodes of Ranvier are uninsulated and highly enriched in ion channels which allow the exchange of ions required to regenerate the action potential. This allows the action potential to ‘jump’ from one node to the next along the axons, resulting in a faster conduction of the action potential (Figure 1.2) [1, 2]. MRI cannot detect individual axons, but can detect axon bundles

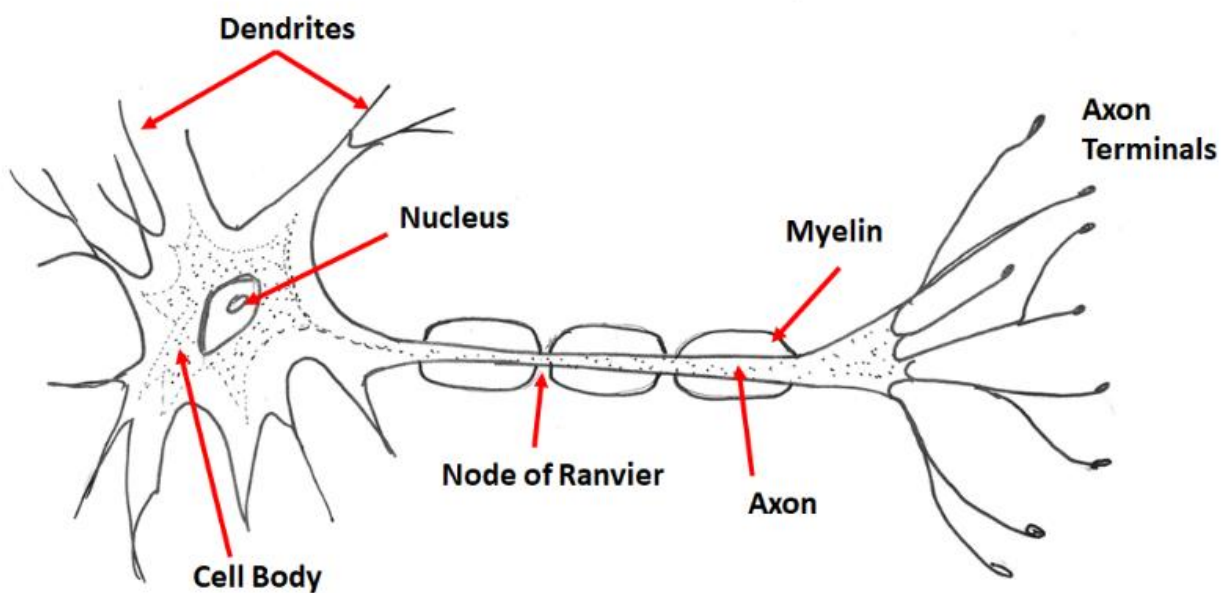


Figure 1.1: Neurons comprise of 3 main features; the cell body which contains the nucleus, the axon which transmits signals from the cell body towards the axon terminal, and the dendrites which receive the signals from the neurons. Myelin insulates axons which allows for the transport of signals across the body.

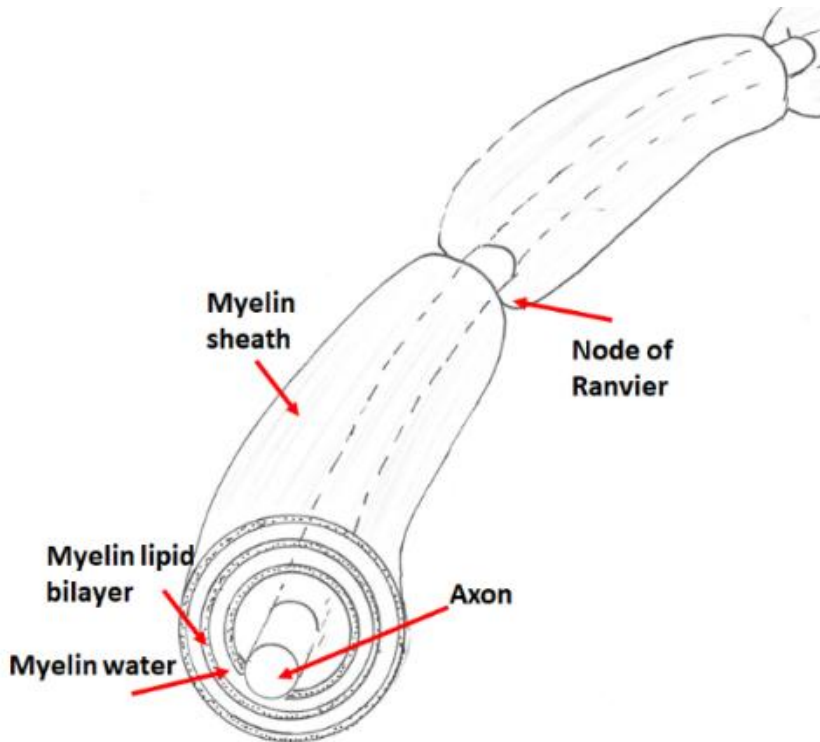


Figure 1.2: Myelin, which aids in the transport of signals throughout the body, surrounds axons that are long, threadlike projections.

1.2 Rationale for this study

Using MRI to measure geometric information in tissue, such as axon diameter distributions has advantages over traditional *ex vivo* histological techniques, even with intact *ex vivo* tissues. The highly invasive methods currently available for measuring axon diameters require sectioning of tissue and are limited due to the need for *post mortem* tissue, the inability to make repeated measurements, the use of small tissue sample sizes, and fixation and cutting artefacts [3, 4]. Traditional histological techniques require that tissues be sectioned which makes the three dimensional nature of the tissue difficult to assess. Histological techniques are also subject to inaccuracies such as cell shrinkage [5]. Because of the difficulties with *ex vivo* histological

measurements there are many properties of tissues that remain unstudied. For instance, measurements of axon diameter distributions, the variation of fibre composition over the population and during development are largely unstudied [5]. With MRI, the tissue remains intact and images can provide measurements over large regions of the tissue thus overcoming these challenges with histological techniques.

MRI can be used to infer the sizes of samples in structures using diffusion weighted imaging and/or diffusion spectroscopy [5-9]. The main application of the MRI size inference methods has been towards axon diameter distributions (ADDs) [3, 10, 11]. These MRI methods are the only non-invasive way to infer axon diameter which is directly proportional to nerve conduction velocity [6, 12-15].

MRI is a non-invasive imaging method that can visualize the anatomy of the subject being imaged. It measures the magnetization of the water inside the tissue of the subject to create images [16-18]. Different types of pulse sequences can be used to allow contrast in the images to depend on different properties of water [19]. For example, in relaxometry images, contrast depends on the relaxation times, T_1 and T_2 , of the tissues [19]; in diffusion weighted images, contrast depends on the mobility of the water molecule [19-21]; and in magnetization transfer imaging, contrast depends on the bound and free water pools [22]. As discussed in 2013 at the International Society for Magnetic Resonance in Medicine (ISMRM) Workshop on Diffusion as a Probe of Neural Tissue Structure (Podstrana, Croatia), many metrics which relate to the image contrast, like the apparent diffusion coefficient (ADC), appear to be related to anatomical structures, but the exact relationship is unknown. While no model is perfect, some are useful. During the workshop, many discussions were made on the need for measurements from MRI to be correlated with the function of the tissue. The methods described in this thesis have the

potential to infer axon diameters that will correlate with the speed of nerve transmission in brain tissue.

Recent studies have indicated that axon diameter sizes and distributions might possibly be altered in diseases [23] such as Alzheimer's disease (AD) [24], amyotrophic lateral sclerosis [25-27], autism [28, 29], diabetes [30], dyslexia [31], multiple sclerosis (MS) [3, 32], and schizophrenia [33, 34]. The methods described in this thesis have the potential to help us understand, diagnose, monitor, and treat these diseases. It will provide a means to evaluate the structure of the white matter in the live brain.

Currently, an accurate diagnosis of AD requires *post-mortem* microscopic examination of the brain. MRI allows us the opportunity to visualize the entire brain *in vivo*. This has the potential for early diagnosis for AD. With my new method, changes in white matter structures in the brain that are indicative of AD could be monitored which would allow us to diagnose AD earlier than before. Although senile plaques and neurofibrillary tangles are some well-established hallmarks of AD, changes in cerebral white matter correlate with the cognitive decline and may also increase the risk of the development of dementia and AD. Neuronal cell death and loss of myelin and axons can cause the loss of brain tissue (atrophy). White matter atrophy in the hippocampus and entorhinal cortex, the most affected regions in AD, has been revealed with MRI even in very mild AD cases [35]. Using this method, changes in the structure of white matter due to AD have the potential to be detected which could help in the understanding and diagnosis of the disease.

In addition, proper diagnosis for both schizophrenia and MS can take months to determine. Diagnosis criteria for those with schizophrenia often changes, and these patients have difficulty

in communicating because of the distress they experience. MS varies widely between people making the use of MRIs controversial in the diagnosis of MS.

Another example is fibre composition and size of the corpus callosum are hypothesized as important biomarkers for schizophrenia, because there have been demonstrated differences in both of these biomarkers between schizophrenia and control humans in *post-mortem* studies. Reduction in both the size and the fibre density of the corpus callosum was found in schizophrenic humans, particularly in females [36]. However, there is question as to whether this reduction in size is a reflection in the change of the overall brain size, or whether it is particular to this structure. Using this method, these measurements can be made on the intact brain allowing a better understanding and diagnosis of the disease.

MS is a demyelinating autoimmune disease which attacks the myelin in the brain and in the spinal cord, causing inflammation and often damaging both myelin sheaths and the underlying axons. When this occurs, the usual flow of nerve pulses is interrupted or distorted. For MS, symptoms are unpredictable as they vary from person to person, depending on where they are affected. This makes diagnosis very difficult and numerous tests need to be performed according to the symptoms they experience. With this method, these white matter changes have the potential to be monitored in the live brain allowing for better monitoring of the disease.

1.3 Goals

A new and important method was developed and optimized for distinguishing the size of very small ($\sim 1 \mu\text{m}$) tissue structures, such as small axon diameters, using diffusion MRI. This method relies on probing the shortest possible diffusion time scales so that the transition from restricted to hindered diffusion within the smallest structures can be detected. Current state-of-the-art methods using temporal diffusion spectroscopy cannot distinguish these small structures because these methods use pulse sequences which limit the ability to probe the shortest diffusion times. This method circumvents those limitations by using oscillating gradients in lieu of pulsed gradients. The new method will have important biological and neuroscience applications; one example is probing axon diameter distributions.

The first MRI diffusion spectroscopy methods used to infer axon diameter sizes [5, 6, 3, 10, 11] use single diffusion encoding sequences [5, 37] such as the pulsed gradient spin echo sequence [38]. These methods measure the apparent diffusion coefficient of water in samples as a function of time and fit those data to analytical models to infer the sizes of objects, such as axon membranes, that cause the restriction of water diffusion. One study inferred that axon diameters are approximately $3.5 \mu\text{m}$ and vary in size across the corpus callosum [11]. A similar variation was visualized across the monkey [10] and the rat corpus callosum [3].

These sequences are sensitive to axons which are larger than $5 \mu\text{m}$ in diameter [7, 39, 40]. The majority of axons constituting cortical connections are smaller than this [41], therefore oscillating gradient spin echo (OGSE) sequences have been simulated [8] for temporal diffusion spectroscopy to study smaller axons [7]. These simulations were able to infer $0.5 \mu\text{m}$ diameter cylinders using gradient strengths available on our BGA6 gradient set from Bruker Biospin

(Bruker Biospin, Ltd., Milton, ON). The study indicated the feasibility of performing diffusion spectroscopy measurements with OGSE on pre-clinical MR imagers to infer small axon diameters for rodent studies.

In addition to diffusion gradient waveform shape, diffusion gradient strength plays a large role in the ability of temporal diffusion spectroscopy methods to infer small restriction sizes such as axon diameters. Several studies have shown the lower limit of the size that can be inferred from the method, termed the resolution limit, depends on the gradient strength [7, 39, 40, 42, 43]. For instance, one study determined that for clinical MRI with 80 mT/m gradients, the resolution limit is 4-8 μm , while for Connectome gradient strengths of 300 mT/m the resolution limit is reduced to 2-5 μm [44]. The studies performed in this work used a pre-clinical MRI Bruker BGA6 gradient set with a maximum gradient strength of 1 T/m which is suitable for rodent studies and brings the resolution limit closer to that needed for rodent white matter.

The routinely used resolution of MR is 1 mm in the human brain and 100 μm in the mouse brain, as reported in 2004 by [45]. The better the resolution, the longer the imaging time and the higher the field strength and gradient strengths needed [45]. Also, smaller sample sizes allow for higher resolution because smaller fields of view can be imaged. For instance, an 18 μm x 34 μm x 18 μm resolution MR image of a quail embryo was collected to create a quail atlas of development [46]. The images collected for the atlas were acquired on an 11.7T MRI and required 5 to 21.5 hours to collect to obtain resolution from 18 μm to 90 μm . Thus, clearly, unless something changes, MRI will not allow us to visualize individual axons.

The experiments in this thesis are not attempting to change the inherent resolution of MRI. Instead, they are exploiting the sensitivity of MRI to diffusion of water to infer the sizes of axon diameters (See Section 3.4). No images or highly detailed mapping of axons using MRI will be

made, especially which look even remotely similar to electron microscopy images (See Section 6.2.6) which clearly have the resolution to visualize individual axons. Instead, many diffusion weighted images with much worse resolution compared to the size of an axon are used to obtain diffusion weighted signals which can be fit to models to extract axon diameter sizes. These signals, fits, and fit parameters give you information about structures, such as axons, making up the voxels (or 3-dimensional arrangement of volume elements) of the images.

1.4 Thesis Organization

This thesis will detail the testing of temporal diffusion spectroscopy methods using oscillating gradient spin echo sequences to infer the diameters of micron-sized restrictions in phantoms with known sizes and in a portion of the human corpus callosum. This section gives a brief overview of the organization of the chapters in the thesis.

Before going into the details of the project, Chapter 2 will discuss the basic physics behind MRI. Many fundamental concepts will be discussed and imaging sequences described, most of which were used in the experiments presented in this thesis. Chapter 3 outlines diffusion and how to use MRI to measure diffusion using the main pulse sequence, the pulse gradient spin echo sequence (PGSE). Another pulse sequence, the oscillating gradient spin echo sequence (OGSE) will be explained and the reasoning for switching from the PGSE to the OGSE. The temporal diffusion spectroscopy methods to infer sample sizes are also explained.

Chapters 4 through 6 explain the experiments performed for this thesis. Chapter 4 covers the first attempts to make inferences of micron-sized restrictions in phantoms. Some experiments

were somewhat successful although they resulted in sizes with high uncertainties. Other experiments produced no meaningful results which allowed for the determination of the size range appropriate for the gradient frequencies used in these experiments. Chapter 5 covers experiments on more optimized phantoms using more optimized imaging parameters and analysis methods. These experiments were featured in a publication accepted to *Magnetic Resonance Materials in Physics, Biology and Medicine* [47]. Chapter 6 describes an experiment, using the methods learned from the previous experiments, to infer axon diameters in human corpus callosum. Lastly, Chapter 7 describes improvements which should be made in future experiments and suggests future directions for this research project.

References

1. Queensland Brain Institute - The University of Queensland (2017, November). What is a neuron [Online]. Available: <https://qbi.uq.edu.au/brain/brain-anatomy/what-neuron>
2. Wikipedia contributors. (2018, April 2). Axon. In Wikipedia, The Free Encyclopedia [Online]. Available: <https://en.wikipedia.org/w/index.php?title=Axon&oldid=833863825>
3. D. Barazany, P. J. Basser, and Y. Assaf, "In vivo measurement of axon diameter distribution in the corpus callosum of rat brain," *Brain*, vol. 132, no. 5, pp. 1210-1220, 2009.
4. J. Virtanen, H. Uusitalo, A. Palkama, and H. Kaufman, "The effect of fixation on corneal endothelial cell dimensions and morphology in scanning electron microscopy," *Acta Ophthalmologica*, vol. 62, no. 4, pp. 577-585, 1984.
5. D. C. Alexander, P.L. Hubbard, M. G. Hall, E. A Moore, M. Ptito, G. J. M. Parker, and T. B. Dyrby, "Orientationally invariant indices of axon diameter and density from diffusion MRI," *NeuroImage*, vol. 52, no. 4, pp. 1374-1389, 2010.
6. Y. Assaf, T. Blumenfeld-Katzir, Y. Yovel, and P. J. Basser, "AxCaliber: a method for measuring axon diameter distribution from diffusion MRI," *Magnetic Resonance in Medicine*, vol. 59, no. 6, pp. 1347-1354, 2008.
7. M. Mercredi, T. J. Vincent, C. P. Bidinosti, and M. Martin, "Assessing the accuracy of using oscillating gradient spin echo sequences with AxCaliber to infer micron-sized axon diameters," *Magnetic Resonance Materials in Physics, Biology and Medicine*, vol. 30, no. 1, pp. 1-14, Feb 2017.
8. E. C. Parsons, M. D. Does, and J. C. Gore, "Temporal diffusion spectroscopy: Theory and implementation in restricted systems using oscillating gradients," *Magnetic Resonance in Medicine*, vol. 55, no. 1, pp. 75-84, 2006.
9. M. Martin, "Measuring restriction sizes using diffusion weighted magnetic resonance imaging: a review," *Magnetic Resonance Insights*, vol. 6, p. MRI. S11149, 2013.
10. T. B. Dyrby, M. G. Hall, M. Ptito, and D. Alexander, "Contrast and stability of the axon diameter index from microstructure imaging with diffusion MRI," *Magnetic Resonance in Medicine*, vol. 70, no. 3, pp. 711-721, 2013.
11. A. Horowitz, D. Barazany, I. Tavor, M. Bernstein, G. Yovel, and Y. Assaf, "In vivo correlation between axon diameter and conduction velocity in the human brain," *Brain Structure and Function*, vol. 220, no. 3, pp. 1777-1788, 2015.
12. J. Hursh, "The properties of growing nerve fibers," *American Journal of Physiology--Legacy Content*, vol. 127, no. 1, pp. 140-153, 1939.
13. J. Ritchie, "On the relation between fibre diameter and conduction velocity in myelinated nerve fibres," *Proceedings of the Royal Society of London B: Biological Sciences*, vol. 217, no. 1206, pp. 29-35, 1982.

14. S. G. Waxman, "Determinants of conduction velocity in myelinated nerve fibers," *Muscle & Nerve*, vol. 3, no. 2, pp. 141-150, 1980.
15. I. Tasaki, K. Ishii, and H. Ito, "On the relation between the conduction-rate, the fiber-diameter and the internodal distance of the medullated nerve fiber," *Japanese Journal of Medical Sciences III, Biophysics*, vol. 9, no. 1, pp. 189-199, 1943.
16. Z.-P. Liang and P. C. Lauterbur, *Principles of Magnetic Resonance Imaging: A Signal Processing Perspective*. New York: Wiley-IEEE Press, 2000.
17. P. T. Callaghan. *Principles of Nuclear Magnetic Resonance Microscopy*. New York: Oxford University Press, Inc., 1993.
18. R. H. Hashemi, W. G. Bradley, and C. J. Lisanti, *MRI: The Basics*, 2nd ed. Philadelphia: Lippincott Williams & Wilkins, 2012.
19. M. A. Bernstein, K. F. King, and X. J. Zhou, *Handbook of MRI Pulse Sequences*. Burlington: Elsevier Academic Press, 2004.
20. D. K. Jones, *Diffusion MRI*. New York: Oxford University Press, 2010.
21. W. S. Price, "Pulsed-field gradient nuclear magnetic resonance as a tool for studying translational diffusion: Part 1. Basic Theory," *Concepts in Magnetic Resonance Part A*, vol. 9, no. 5, pp. 299-336, 1997.
22. I. M. Vavasour, K. P. Whittall, D. K. Li, and A. L. MacKay, "Different magnetization transfer effects exhibited by the short and long T₂ components in human brain," *Magnetic Resonance in Medicine*, vol. 44, no. 6, pp. 860-866, 2000.
23. R. J. Zatorre, R. D. Fields, and H. Johansen-Berg, "Plasticity in gray and white: neuroimaging changes in brain structure during learning," *Nature Neuroscience*, vol. 15, no. 4, p. 528, 2012.
24. R. A. Armstrong, "Alzheimer's Disease and the Eye☆," *Journal of Optometry*, vol. 2, no. 3, pp. 103-111, 2009.
25. S. Cluskey and D. Ramsden, "Mechanisms of neurodegeneration in amyotrophic lateral sclerosis," *Molecular Pathology*, vol. 54, no. 6, p. 386, 2001.
26. F. Agosta, E. Pagani, M. Petrolini, D. Caputo, M. Perini, A. Prella, F. Salvi, and M. Filippi, "Assessment of white matter tract damage in patients with amyotrophic lateral sclerosis: a diffusion tensor MR imaging tractography study," *American Journal of Neuroradiology*, vol. 31, no. 8, pp. 1457-1461, 2010.
27. N. S. Metwalli, M. Benatar, G. Nair, S. Usher, X. Hu, and J. D. Carew, "Utility of axial and radial diffusivity from diffusion tensor MRI as markers of neurodegeneration in amyotrophic lateral sclerosis," *Brain Research*, vol. 1348, pp. 156-164, 2010.
28. J. Piven, J. Bailey, B. J. Ranson, and S. Arndt, "An MRI study of the corpus callosum in autism," *American Journal of Psychiatry*, vol. 154, no. 8, pp. 1051-1056, 1997.
29. J. R. Hughes, "Autism: the first firm finding= underconnectivity?" *Epilepsy & Behavior*, vol. 11, no. 1, pp. 20-24, 2007.

30. T. Malysz, J. Ilha, P. S. D. Nascimento, K. D. Angelis, B. D. A. Schaan, and M. Achaval, "Beneficial effects of treadmill training in experimental diabetic nerve regeneration," *Clinics*, vol. 65, no. 12, pp. 1329-1337, 2010.
31. C. Njiokiktjien, L. De Sonneville, and J. Vaal, "Callosal size in children with learning disabilities," *Behavioural Brain Research*, vol. 64, no. 1, pp. 213-218, 1994.
32. V. A. Deshmukh, V. Tardif, C. A. Lyssiotis, C. C. Green, B. Kerman, H. J. Kim, K. Padmanabhan, J. G. Swoboda, I. Ahmad, and T. Kondo, "A regenerative approach to the treatment of multiple sclerosis," *Nature*, vol. 502, no. 7471, p. 327, 2013.
33. P. Randall, "Schizophrenia, abnormal connection, and brain evolution," *Medical Hypotheses*, vol. 10, no. 3, pp. 247-280, 1983.
34. D. Rice and S. Barone Jr., "Critical periods of vulnerability for the developing nervous system: evidence from humans and animal models," *Environmental Health Perspectives*, vol. 108, no. Suppl 3, p. 511, 2000.
35. M. Z. Kastyak-Ibrahim, D. L. Di Curzio, R. Buist, S. L. Herrera, B. C. Albeni, M. R. Del Bigio, and M. Martin, "Neurofibrillary tangles and plaques are not accompanied by white matter pathology in aged triple transgenic-Alzheimer disease mice," *Magnetic Resonance Imaging*, vol. 31, no. 9, pp. 1515-1521, 2013.
36. J. R. Highley, M. M. Esiri, B. McDonald, M. Cortina-Borja, B. M. Herron, and T. J. Crow, "The size and fibre composition of the corpus callosum with respect to gender and schizophrenia: a post-mortem study," *Brain*, vol. 122, no. 1, pp. 99-110, 1999.
37. N. Shemesh, S. N. Jespersen, D. C. Alexander, Y. Cohen, I. Drobnjak, T. B. Dyrby, J. Finsterbusch, M. A. Koch, T. Kuder, and F. Laun, "Conventions and nomenclature for double diffusion encoding NMR and MRI," *Magnetic Resonance in Medicine*, vol. 75, no. 1, pp. 82-87, 2016.
38. E. O. Stejskal and J. E. Tanner, "Spin diffusion measurements: spin echoes in the presence of a time-dependent field gradient," *The Journal of Chemical Physics*, vol. 42, no. 1, pp. 288-292, 1965.
39. M. Nilsson, D. van Westen, F. Ståhlberg, P. C. Sundgren, and J. Lätt, "The role of tissue microstructure and water exchange in biophysical modelling of diffusion in white matter," *Magnetic Resonance Materials in Physics, Biology and Medicine*, vol. 26, no. 4, pp. 345-370, 2013.
40. M. Nilsson, S. Lasič, I. Drobnjak, D. Topgaard, and C.-F. Westin, "Resolution limit of cylinder diameter estimation by diffusion MRI: The impact of gradient waveform and orientation dispersion," *NMR in Biomedicine*, vol. 30, no. 7, p. e3711.
41. G. Innocenti, R. Caminiti, and F. Aboitiz, "Comments on the paper by Horowitz et al.(2014)," *Brain Structure and Function*, vol. 220, no. 3, p. 1789, 2015.
42. M. Mercredi, S.L. Herrera, R. Buist, K. Matsuda, and M. Martin. "Determining how varying the number of gradient strengths and frequencies affects fitted mean axon diameters in the corpus callosum using oscillating spin echo gradients." in *ISMRM*, Paris, France, 2018

43. M. Mercredi and M. Martin, "Toward faster inference of micron-scale axon diameters using Monte Carlo simulations," *Magnetic Resonance Materials in Physics, Biology and Medicine*, pp. 1-20, 2018. <https://doi.org/10.1007/s10334-018-0680-1>
44. J. A. McNab, B. L. Edlow, T. Witzel, S. Y. Huang, H. Bhat, K. Heberlein, T. Feiweier, K. Liu, B. Keil, and J. Cohen-Adad, "The Human Connectome Project and Beyond: Initial Applications of 300 mT/m Gradients," *NeuroImage*, vol. 80, pp. 234-245, 2013.
45. A. P. Koretsky, "New developments in magnetic resonance imaging of the brain," *NeuroRx*, vol. 1, no. 1, pp. 155-164, 2004.
46. S. W. Ruffins, M. Martin, L. Keough, S. Truong, S. E. Fraser, R. E. Jacobs, and R. Lansford, "Digital three-dimensional atlas of quail development using high-resolution MRI," *The Scientific World Journal*, vol. 7, pp. 592-604, 2007.
47. S. L. Herrera, M. Mercredi, R. Buist R, and M. Martin. "Inferring diameters of spheres and cylinders using interstitial water". *Magnetic Resonance Materials in Physics, Biology and Medicine*. 2018. <https://doi.org/10.1007/s10334-018-0685-9>

Chapter 2

Magnetic Resonance Imaging - Basics and Related Imaging Sequences

The text and images contained within this chapter explaining the theory involved in magnetic resonance imaging have mostly been taken from my Master's thesis [1]. This chapter will explain magnetic resonance imaging and provide the framework to understand better the theory involved and how it relates to this project.

Section 2.1 covers nuclear magnetic resonance which is the basis of magnetic resonance imaging which is explained in Section 2.2. Section 2.3 covers the free induction decay, and Section 2.4 explains how the MRI signal is detected. Sections 2.5 and 2.6 covers how a signal is localized using a gradient and how the magnetization relaxes. Section 2.7 explains many of the basic pulse sequences used in MRI. Lastly, Section 2.8 explains k-space and image reconstruction.

2.1 Nuclear Magnetic Resonance

Magnetic resonance imaging (MRI) is founded on the basis of nuclear magnetic resonance (NMR) which was demonstrated experimentally in 1946 independently by Purcell et al. [2] and Bloch [3]. In this section, NMR will be explained, and expanding from that NMR imaging.

2.1.1 Nuclear Magnetic Moments

MRI is based on the interaction of a nucleus with a magnetic moment with an external magnetic field, \vec{B}_0 . Most MRI uses the nucleus of a hydrogen atom (^1H), with the dominant nucleus being the proton. The interaction of the proton with the external magnetic field results in the precession of the proton spin about the field direction. MR imaging rests on the ability to manipulate, with a combination of magnetic fields, and then detect, the bulk precession of hydrogen spins in water, fat and other organic molecules.

Nuclei have an intrinsic angular momentum called spin, \vec{J} . Semi-classically, the basic motion of the proton spin can be described as a spinning gyroscope that is electrically charged with an effective loop of electric current around the same axis about which it is spinning. This effective current loop interacts with the external magnetic fields as well as producing its own magnetic field. The magnetic dipole moment (or magnetic moment) vector $\vec{\mu}$, describes the strength at which the loop interacts with the external magnetic field, as well as the strength at which the loop produces its own field. The direction of this vector is the spin axis itself, and the magnetic moment vector will align itself along any external static magnetic field \vec{B}_0 . The magnetic moment vector will precess around the field direction. An example of this is shown in Figure 2.1.

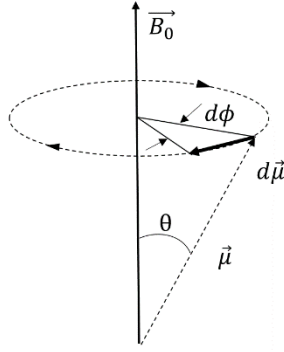


Figure 2.1: The proton's spin interacts with the magnetic field to produce a torque, causing it to precess about \vec{B}_0 , as the fixed axis. Looking down from above \vec{B}_0 , the magnetic moment vector $\vec{\mu}$ precesses clockwise as it is proportional to the spin vector. For the customary counterclockwise definition of polar angles, the differential $d\phi$ shown is negative.

The spin angular momentum and magnetic moment vectors can be related to each other by

$$\vec{\mu} = \gamma \vec{J} \quad (2.1)$$

where γ is a physical constant known as the gyromagnetic ratio which is dependent on the nucleus. It can also be written in the form of another constant $\bar{\gamma} = \frac{\gamma}{2\pi}$ which changes the units to Hertz (Hz) from radians/seconds. The ^1H nucleus has a gyromagnetic ratio of $\gamma = 2.675 \times 10^8 \text{ rad/sec}\cdot\text{T}$ or $\bar{\gamma} = 42.58 \text{ MHz/T}$. The MRI scanner used in this thesis has a magnetic field of $B_0 = 7\text{T}$ which results in a Larmor frequency of $f_0 = 300 \text{ MHz}$. The Larmor frequency is the rate of precession of the magnetic moment of the proton around the external field, and is later described in Equation (2.14).

The magnitude of the magnetic moment is

$$|\vec{\mu}| = \gamma \hbar \sqrt{I(I+1)} \quad (2.2)$$

where \hbar is the Planck's constant divided by 2π ($\hbar = 1.05546 \times 10^{-34} \text{ J}\cdot\text{s}$), and I is the nuclear spin quantum number which depends on specific nuclei. This spin quantum number can

take on integer, half-integer, or zero values ($I = 0, 1/2, 1, 3/2, 2, \dots$). The value of the spin quantum number for a particular nucleus is dependent on the nucleus. Nuclei with odd mass number have half-integral spin. Nuclei with even mass number and an even charge number have zero spin. Nuclei with even mass number but an odd charge number have integral spin.

For nuclei such as ^1H , ^{13}C , the spin quantum number is $I = 1/2$ and such a spin system is called a spin-1/2 system. In MR, nuclei with nonzero spin are used.

In the absence of an external magnetic field, the direction of the spin vector, $\vec{\mu}$ is completely random because of thermal motion. Therefore at thermal equilibrium, no net magnetic field exists around a macroscopic object. In order to generate macroscopic magnetization from an object, spin vectors need to be lined up. This is done by exposing the object to a strong magnetic field \vec{B}_0 . Using the convention where the magnetic field is applied along the z-axis, $\vec{B}_0 = B_0 \hat{k}$. Because of quantum mechanics, we know that the properties that we observe from a single nucleus belong to one of a set of discrete set of probabilities.

In this model, the z-component of $\vec{\mu}$ becomes certain due to the B_0 field and is given by

$$\mu_z = \gamma m_I \hbar \quad (2.3)$$

where m_I is called the magnetic quantum number. For any nucleus with nonzero spin, $m_I = -I, -I + 1, \dots, I - 1, I$, which corresponds to $(2I+1)$ possible orientations for $\vec{\mu}$ with respect to the direction of the external field. The angle θ between $\vec{\mu}$ and \vec{B}_0 is calculated by:

$$\cos \theta = \frac{\mu_z}{\mu} = \frac{m_I}{\sqrt{I(I+1)}} \quad (2.4)$$

The orientation of $\vec{\mu}$ is quantized along the direction of the external field, and the direction of the transverse component $\vec{\mu}_{xy}$ is randomly oriented in the transverse plane and as

$$\overrightarrow{\mu_{xy}} = \mu_x \hat{i} + \mu_y \hat{j} \quad (2.5)$$

and μ_x and μ_y can be expressed as

$$\begin{cases} \mu_x = |\overrightarrow{\mu_{xy}}| \cos \xi \\ \mu_y = |\overrightarrow{\mu_{xy}}| \sin \xi \end{cases} \quad (2.6)$$

where ξ is a random variable that is uniformly distributed over $[0, 2\pi)$ and $|\overrightarrow{\mu_{xy}}|$ is given by

$$|\overrightarrow{\mu_{xy}}| = \sqrt{\mu^2 - \mu_z^2} = \gamma \hbar \sqrt{I(I+1) - m_I^2} \quad (2.7)$$

For a spin-1/2 system, $I = \frac{1}{2}$ and $m_I = \pm \frac{1}{2}$, we can calculate the angle θ between $\overrightarrow{B_0}$ and μ and the transverse magnitude using Equations (2.4) and (2.7), which gives:

$$\theta = \pm 54^\circ \quad (2.8)$$

$$|\overrightarrow{\mu_{xy}}| = \frac{\gamma \hbar}{\sqrt{2}} \quad (2.9)$$

These nuclear magnetic moments have a random orientation in the absence of an externally applied magnetic field (Figure 2.2a). When an external magnetic field is applied, the magnetic moment vectors become oriented in one of two directions (parallel or anti-parallel) with respect to the applied magnetic field B_0 as based on Equation (2.8) (Figure 2.2b, c).

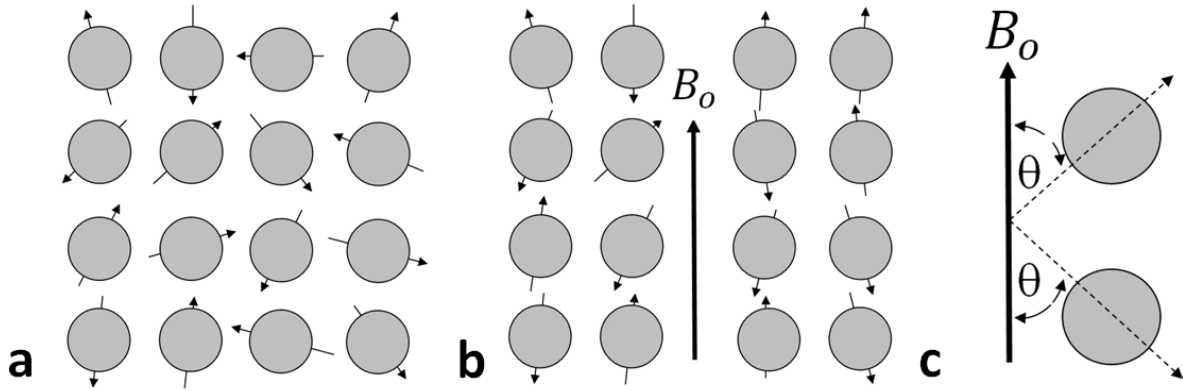


Figure 2.2: (a) Nuclear magnetic moment vectors have random orientations when no magnetic field is present. (b) Magnetic moment vectors become oriented in one of two directions with respect to the applied magnetic field B_0 . (c) Nuclei either align themselves parallel or anti-parallel with respect to the B_0 field [1, modified from 4, 5].

Although the properties of spin in particles are quantum in nature, they can also be described by classical mechanics, as explained below [6]. Using the classical mechanics vector model, when a magnetic dipole moment $\vec{\mu}$ is placed in an external magnetic field \vec{B}_0 it experiences a torque (Figure 2.3).

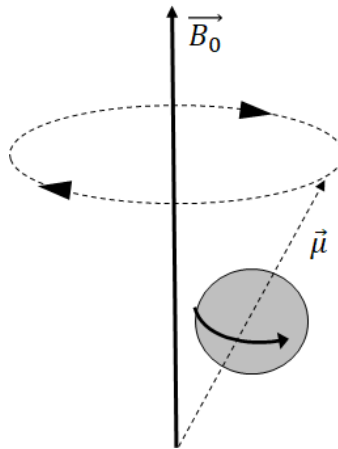


Figure 2.3: Precession of the nuclear magnetic moment about an external field is similar to a spinning top in a gravitational field [1]. The nucleus precesses around B_0 at the Larmor frequency given in Equation (2.14).

The classical equation of the motion of the magnetic dipole moment in equilibrium in a static magnetic field, \vec{B}_0 , is

$$\frac{d\vec{J}}{dt} = \vec{\mu} \times B_0 \hat{k} \quad (2.10)$$

Because $\vec{\mu} = \gamma \vec{J}$, this can be written as the equation of motion for isolated spins:

$$\frac{d\vec{\mu}}{dt} = \gamma \vec{\mu} \times B_0 \hat{k} \quad (2.11)$$

The solution to the Equation (2.11) using the convention in MRI to assign the z-axis to align with the magnetic field \vec{B}_0 is expressed as follows [4]:

$$\begin{cases} \mu_{xy}(t) = \mu_{xy}(0)e^{-i\gamma B_0 t} \\ \mu_z(t) = \mu_z(0) \end{cases} \quad (2.12)$$

where $\mu_{xy}(0)$ and $\mu_z(0)$ are initial values and the transverse component

$\mu_{xy} = \mu_x + i\mu_y = \vec{\mu}_x \hat{i} + \vec{\mu}_y \hat{j}$ is rewritten as a complex exponential. This transverse component can also be written as:

$$\mu_{xy}(t) = \begin{cases} \mu_x(t) = \mu_x(0) \cos(\gamma B_0 t) + \mu_y(0) \sin(\gamma B_0 t) \\ \mu_y(t) = -\mu_x(0) \sin(\gamma B_0 t) + \mu_y(0) \cos(\gamma B_0 t) \end{cases} . \quad (2.13)$$

Equation (2.12) describes the precession of $\vec{\mu}$ about the B_0 field (or z-axis), which is called nuclear precession. The precessing magnetization has an angular frequency which rotates in the clockwise direction, which is called the Larmor frequency.

$$\omega_0 = \gamma B_0 \quad (2.14)$$

In addition to Equation (2.12), nuclear precession can be described by an angular velocity vector defined as:

$$\vec{\omega} = -\gamma\vec{B}_0 = -\omega_0\hat{k} \quad (2.15)$$

Precession can also be described using the rotation matrix, where $\mathbf{R}(\alpha)$ can describe the rotation of α about the z-axis

$$\mathbf{R}_z(\alpha) = \begin{bmatrix} \cos \alpha & \sin \alpha & 0 \\ -\sin \alpha & \cos \alpha & 0 \\ 0 & 0 & 1 \end{bmatrix} \quad (2.16)$$

Equations (2.12) and (2.13) can be rewritten to express μ with time-dependence as

$$\boldsymbol{\mu}(t) = \mathbf{R}_z(\omega_0 t)\boldsymbol{\mu}(0) \quad (2.17)$$

where μ should be interpreted as a column vector $\mu = [\mu_x, \mu_y, \mu_z]^T$.

2.1.2 Bulk Magnetization

A macroscopic magnetization vector \vec{M} is used to describe the collective behaviour of a spin system, which is the vector sum of all the microscopic magnetic moments $\vec{\mu}_n$ in the object. In the absence of an external magnetic field, $\vec{M} = 0$. When an object is placed in a B_0 field, based on Section 2.1.1, $\vec{\mu}_n$ can take on one of two possible orientations with respect to the z-axis at any given time. Spins in different orientations have different energy of interaction with the external magnetic field.

The energy associated with the nuclear dipoles based on their alignment in the z-axis is given by

$$E = -\vec{\mu} \cdot \vec{B}_o = -\mu_z B_o = -\gamma \hbar m_I B_o \quad (2.18)$$

Because there are two possible values of m_I ($\pm 1/2$), there exists two energy states in the spin- $\frac{1}{2}$

^1H nucleus:

$$E_{\uparrow} = -\frac{1}{2} \gamma \hbar B_o \quad \text{and} \quad E_{\downarrow} = +\frac{1}{2} \gamma \hbar B_o \quad (2.19)$$

which describe the spin-up (lower energy) and spin-down (higher energy) states, respectively.

The two different energy states correspond with the proton magnetic moments aligning parallel (lower energy) or anti-parallel (higher energy) with B_o . The energy difference between these two states is

$$\Delta E = E_{\downarrow} - E_{\uparrow} = \gamma \hbar B_o \quad (2.20)$$

where this energy level splitting is known as the Zeeman effect as shown in Figure 2.4.

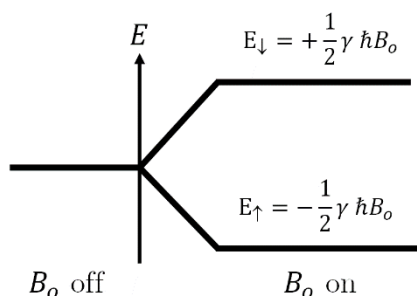


Figure 2.4: Zeeman splitting for a spin- $\frac{1}{2}$ system with an applied magnetic field, B_o . The two energy states correspond with the proton magnetic moments aligning parallel (lower energy E , E_{\uparrow}) or anti-parallel (higher energy E , E_{\downarrow}) with B_o [1].

A nucleus in the lower energy state would need to absorb a photon with energy

$\Delta E = \gamma \hbar B_o = \hbar \omega_o$ to move to the higher energy state and $\omega_o = \gamma B_o$ is exactly the Larmor frequency.

To calculate the relative number of protons in the parallel (low energy) state N_{\uparrow} versus the anti-parallel (high energy) state N_{\downarrow} in thermal equilibrium, the Boltzmann equation is used:

$$\frac{N_{\uparrow}}{N_{\downarrow}} = \exp\left(\frac{\Delta E}{k_B T}\right) = \exp\left(\frac{\gamma \hbar B_o}{k_B T}\right) \quad (2.21)$$

where T is the temperature of the spin system (for live imaging body temperature is about 310 K), k_B is the Boltzmann constant ($k_B = 1.38 \times 10^{-23} \text{ J/K}$).

The ratio of $\frac{N_{\uparrow}}{N_{\downarrow}}$ can be found as follows:

$$\frac{N_{\uparrow}}{N_{\downarrow}} = \exp\left(\frac{2\pi(42.58 \times 10^6 \frac{\text{Hz}}{\text{T}})(1.05546 \times 10^{-34} \text{ J}\cdot\text{s})B_o}{(1.38 \times 10^{-23} \frac{\text{J}}{\text{K}})(310 \text{ K})}\right) = \exp(6.6 \times 10^{-6} \cdot B_o).$$

For experiments performed for this thesis at a magnetic field of $B_o = 7 \text{ T}$ (Tesla) which corresponds to $\Delta E = \gamma \hbar B_o = 1.976 \times 10^{-25} \text{ J}$, the ratio of dipoles in the two energy states is

$\frac{N_{\uparrow}}{N_{\downarrow}} = \exp(46 \times 10^{-6}) = 1.0005$. Similarly for experiments performed at 1.5, 3.0 and 11 T,

have $\frac{N_{\uparrow}}{N_{\downarrow}}$ equalling 1.00001, 1.00002, 1.0007, respectively. To show the difference of between

these magnetic field strengths, we can take an approximation using the Taylor expansion for

$\exp(x)$: $1 + x + \frac{x^2}{2} + \dots$. For small x , this gives $\exp(x) = 1 + x$. Therefore $\frac{N_{\uparrow}}{N_{\downarrow}} \sim 1 + x$ can be

rewritten as the following: $N_{\uparrow} \sim N_{\downarrow} + x \cdot N_{\downarrow} \Rightarrow N_{\uparrow} - N_{\downarrow} \sim x \cdot N_{\downarrow}$

Table 2.1 gives the difference of $N_{\uparrow} - N_{\downarrow}$ in parts per million (ppm) for magnetic fields at clinical field strengths of 1.5 T and 3.0 T, as well as pre-clinical field strengths of 7 T and 11.7 T.

Table 2.1: Difference $N_{\uparrow} - N_{\downarrow}$ for magnetic fields at 1.5, 3, 7 and 11.7 T (in ppm)

B_o (T)	1.5	3.0	7.0	11.7
$N_{\uparrow} - N_{\downarrow}$	9.9×10^{-6}	20×10^{-6}	46×10^{-6}	77×10^{-6}

2.1.3 Net Magnetization Vector

The difference in the number of nuclei aligned parallel and anti-parallel to B_o leads to the net magnetization vector \vec{M} that is used to generate a signal. By adding all the individual dipole moments $\vec{\mu}_n$ in a sample, we obtain the net magnetization

$$\vec{M} = \sum_{n=1}^N \vec{\mu}_n = \left(\sum_{n=1}^N \mu_{x,n} \right) \hat{x} + \left(\sum_{n=1}^N \mu_{y,n} \right) \hat{y} + \left(\sum_{n=1}^N \mu_{z,n} \right) \hat{z} \quad (2.22)$$

where N is the total number of spins in a unit volume. Because there is no preferential orientation in the xy-plane, the x- and y- components of the magnetization vector each average to zero, thus

$$\vec{M} = \left(\sum_{n=1}^N \mu_{z,n} \right) \hat{z} = \left(\sum_{n=1}^N \gamma \hbar (m_I)_n \right) \hat{z} = \gamma \hbar \left(\sum_{n=1}^N (m_I)_n \right) \hat{z} . \quad (2.23)$$

For ^1H nuclei,

$$\sum_{n=1}^N (m_I)_n = \frac{1}{2} (N_{\uparrow} - N_{\downarrow}) \quad (2.24)$$

therefore the magnetization vector becomes:

$$\vec{M} = \left[\gamma \hbar \frac{1}{2} (N_{\uparrow} - N_{\downarrow}) \right] \hat{z} . \quad (2.25)$$

In practice, because the energy difference is so small ($\Delta E \ll k_B T$), by first order approximation, Equation (2.21) can be written as

$$N_{\uparrow} - N_{\downarrow} \cong \frac{N \gamma \hbar B_o}{2 k_B T} . \quad (2.26)$$

For the experiments in this thesis which used the magnetic field at $B_o = 7T$, the difference of dipoles is $N_{\uparrow} - N_{\downarrow} \cong 23$ ppm. The difference, $N_{\uparrow} - N_{\downarrow}$, for some clinical and pre-clinical MRI magnetic fields are given in Table 2.2 with $N = 10^6$ total dipoles.

Table 2.2: Difference $N_{\uparrow} - N_{\downarrow}$ in ppm for magnetic fields 1.5, 3.0, 7.0, 11.7 Tesla

B_o (T)	1.5	3.0	7.0	11.7
$N_{\uparrow} - N_{\downarrow}$	5.0	9.9	23	39

Combining Equations (2.25) and (2.26) gives the magnitude of the magnetization vector at equilibrium

$$\vec{M}_o = \left[\gamma \hbar \frac{1}{2} \left(\frac{N \gamma \hbar B_o}{2 k_B T} \right) \right] \hat{z} = \frac{N \gamma^2 \hbar^2 B_o}{4 k_B T} \hat{z} \quad (2.27)$$

which points exactly along the positive direction of the z-axis. Here, this magnitude of \vec{M} is directly proportional to the total number of spins N , and also to the external magnetic strength B_o with $M_o \ll B_o$ because it is static at equilibrium.

2.1.4 Inhomogeneities in the Magnetic Field

Spin systems can contain a range of resonance frequencies. In this case, we call each group of nuclear spins in the same resonance frequency an isochromat. The two main reasons for a magnetized spin system to have multiple isochromats is the existence of inhomogeneities in the B_0 field, and the chemical shift effect.

When B_0 is inhomogeneous, then the Larmor frequency is spatially dependent, i.e. spins with the same γ value will have different Larmor frequencies at different spatial locations. The chemical shift effect occurs because nuclei in different chemical environments resonate at slightly different frequencies. A weak magnetic field shields the nucleus which is caused by the orbiting electrons that surround it. As a result the effective magnetic field that a nucleus sees is

$$\hat{B}_0 = B_0(1 - \delta) \quad (2.28)$$

where δ is a shielding constant.

2.2 Magnetic Resonance Signal

In order to produce an MR signal, the spin system needs to be excited using an external force such as a radio frequency (RF) pulse. The components required to produce an MR signal will be discussed in this section, namely RF pulses and extending from that the rotating frame of reference, Bloch equations and the flip angle.

2.2.1 Radio-Frequency Pulse

To measure the NMR signal generated, the magnetization vector \vec{M} must be made to vary with time. This is done by applying a RF pulse which is a short, time-varying magnetic field \vec{B}_1 that is perpendicular to the main magnetic field \vec{B}_0 with $|\vec{B}_1| \ll |\vec{B}_0|$. The B_1 field, for example, can take on the following form: $\vec{B}_1(t) = B_1 \cdot \cos(\omega_0 t)$

The NMR signal arises from the transitions between the two energy states of protons, with energy difference of $\Delta E = \gamma \hbar B_0$ as given in Equation (2.20). Thus the B_1 field must supply this energy $\Delta E = \gamma \hbar B_0$ so that the nuclei can move from the lower state to the higher state.

Therefore the B_1 field must vary in time with frequency ω_0 and for typical MR field strengths, ω_0 is within the RF range.

The RF pulse is described by the function [4]

$$\vec{B}_1(t) = B_1^e(t) [\cos(\omega_0 t + \phi)\hat{x} - \sin(\omega_0 t + \phi)\hat{y}] \quad (2.29)$$

This can also be written in complex form:

$$\vec{B}_1(t) = B_1^e(t)e^{-i(\omega_o t + \phi)} \quad (2.30)$$

where ω_o is the frequency of the applied RF pulse, ϕ is the initial phase angle of the B_1 field, and $B_1^e(t)$ is the envelope of the pulsed RF function, which describes its shape and duration.

Common shapes for RF pulses are rectangle and sinc, the reasoning for these two typical pulse shapes will be given in Section 2.5.1.

A rectangular pulse can be defined as

$$B_1^e(t) = B_1 \prod \left(\frac{t - \tau_P/2}{\tau_P} \right) \quad (2.31)$$

where τ_P is the pulse width, and Π is a boxcar function that is zero outside the interval $t=[0, \tau_P]$ and it is at an amplitude of 1 inside the interval. A sinc pulse can be defined as

$$B_1^e(t) = \begin{cases} B_1 \text{sinc} \left[\pi \Delta f \left(t - \frac{\tau_P}{2} \right) \right] & ; 0 \leq t \leq \tau_P \\ 0 & ; t > \tau_P \end{cases} \quad (2.32)$$

where the peak of the main lobe of the pulse is at an amplitude of B_1 when $t = \frac{\tau_P}{2}$, which is at the time when $\text{sinc}(0)=1$. The zeroes of this curve are found at $t = \pm n\pi + \frac{\tau_P}{2}$ for $n = 1, 2, \dots$, with the main lobe found between $\pm\pi + \frac{\tau_P}{2}$. The shape of the rectangle and sinc RF pulses are given in Figure 2.5.

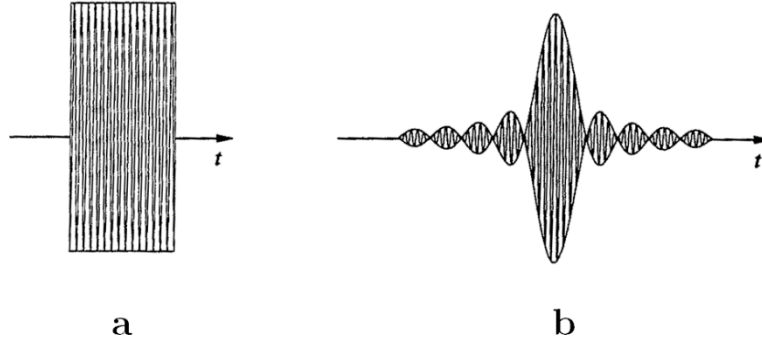


Figure 2.5: RF pulses with (a) rectangle envelope function, and (b) sinc envelope function [4]. The RF pulse is oscillating with frequency ω_0 .

2.2.2 Rotating Frame of Reference

To explain the effect of the rotating magnetization vector \vec{M} caused by the rotating B_1 field, \vec{M} and B_1 can be viewed in a reference frame rotating at the same rate as \vec{M} or B_1 , that is at a rate of Larmor frequency, ω_0 . Mathematically, the rotating frame is a transformation expressed as follows:

$$\left. \begin{aligned} \hat{x}' &= \cos(\omega_0 t) \hat{x} - \sin(\omega_0 t) \hat{y} \\ \hat{y}' &= \sin(\omega_0 t) \hat{x} + \cos(\omega_0 t) \hat{y} \\ \hat{z}' &= \hat{z} \end{aligned} \right\} \quad (2.33)$$

Rewriting the B_1 field in terms of x and y components

$$(i) \quad \vec{B}_1(t) = B_{1x}(t)\hat{x} + B_{1y}(t)\hat{y} \quad (2.34)$$

$$(ii) \quad \vec{B}_{1,rot}(t) = B_{1x'}(t)\hat{x}' + B_{1y'}(t)\hat{y}',$$

where in the (i) laboratory frame, the spin system precesses about the magnetic field at Larmor frequency, and in (ii) the entire rotating frame rotates at Larmor frequency.

The magnetization vector, can also be written in terms of x and y components

$$(i) \quad \vec{M} = M_x \hat{x} + M_y \hat{y} + M_z \hat{z} \quad (2.35)$$

$$(ii) \quad \vec{M}_{rot} = M_{x'} \hat{x}' + M_{y'} \hat{y}' + M_{z'} \hat{z}'$$

where (i) is in the laboratory frame, and (ii) is in the rotating frame. To convert the \vec{M} and \vec{B}_1 vector between the laboratory and the rotating frame, the following coordinate transformations are performed respectively in Equations (2.36) and (2.37).

Setting $\vec{M}_{rot} = \vec{M}$ gives the transformation as follows:

$$\begin{bmatrix} M_{x'} \\ M_{y'} \\ M_{z'} \end{bmatrix} = \begin{bmatrix} \cos(\omega_o t) & -\sin(\omega_o t) & 0 \\ \sin(\omega_o t) & \cos(\omega_o t) & 0 \\ 0 & 0 & 1 \end{bmatrix} \begin{bmatrix} M_x \\ M_y \\ M_z \end{bmatrix} \quad (2.36)$$

Similarly, setting $\vec{B}_{1,rot} = \vec{B}$ gives the transformation of

$$\begin{bmatrix} B_{1x'} \\ B_{1y'} \end{bmatrix} = \begin{bmatrix} \cos(\omega_o t) & -\sin(\omega_o t) \\ \sin(\omega_o t) & \cos(\omega_o t) \end{bmatrix} \begin{bmatrix} B_{1x} \\ B_{1y} \end{bmatrix} \quad (2.37)$$

The precession of the magnetization vector in the presence of a rotating RF field can be observed as shown in Figure 2.6.

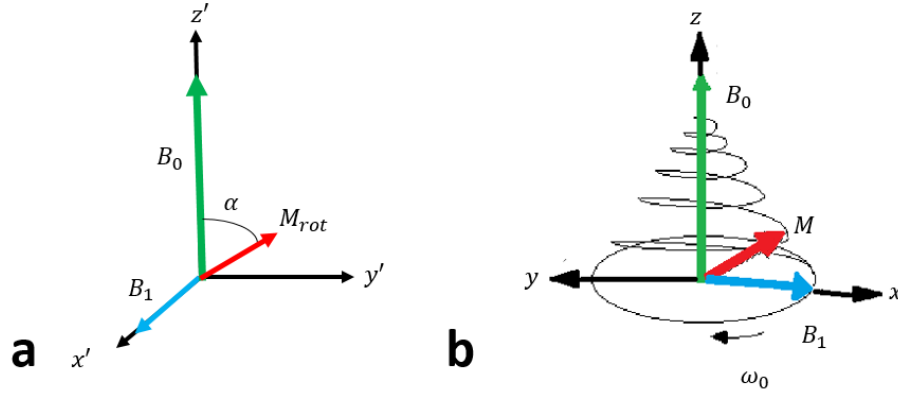


Figure 2.6: The precession of net magnetization in (a) the rotating frame and (b) the laboratory frame. The angle at which the RF field tips M_{rot} is denoted as α in the rotating frame. In the laboratory frame the magnetization spirals down towards the transverse plane as it is under the influence of the longitudinal field B_0 and the transverse field [1, modified from 7].

2.2.3 Bloch Equation

The time-dependent change of the net magnetization vector \vec{M} is described by the Bloch equation [3]:

$$\frac{d\vec{M}}{dt} = \gamma \vec{M} \times \vec{B} - \frac{M_x \hat{x} + M_y \hat{y}}{T_2} - \frac{(M_z - M_0) \hat{z}}{T_1} \quad (2.38)$$

where M_0 is the thermal equilibrium value for \vec{M} in the presence of B_0 only, T_1 is the relaxation time constant for the longitudinal magnetization to return to equilibrium after an RF pulse, and T_2 is the relaxation time constant in the presence of a perfectly uniform external field \vec{B}_0 for the transverse magnetization to decay after an RF pulse. For explanation of the relaxation time constants see Section 2.6.

The Bloch equation during an RF pulse can take on a simpler form (ignoring the last two terms) because the duration of B_1 is much shorter than the relaxation times. During the RF pulse, the Bloch equation is simplified to

$$\frac{d\vec{M}}{dt} = \gamma \vec{M} \times \vec{B} \quad (2.39)$$

By taking the first derivative of \vec{M} with respect to time from Equation (2.35) in the rotating frame gives

$$\begin{aligned} \frac{d\vec{M}}{dt} &= \hat{x}' \frac{dM_{x'}}{dt} + \hat{y}' \frac{dM_{y'}}{dt} + \hat{z}' \frac{dM_{z'}}{dt} + M_{x'} \frac{d\hat{x}'}{dt} + M_{y'} \frac{d\hat{y}'}{dt} + M_{z'} \frac{d\hat{z}'}{dt} \\ \rightarrow \frac{d\vec{M}}{dt} &= \left[\frac{d\vec{M}}{dt} \right]_{rot} + M_{x'} \frac{d\hat{x}'}{dt} + M_{y'} \frac{d\hat{y}'}{dt} + M_{z'} \frac{d\hat{z}'}{dt} \end{aligned} \quad (2.40)$$

The time derivatives of the unit vectors can be written as:

$$\frac{d\hat{x}'}{dt} = \vec{\omega} \times \hat{x}'; \quad \frac{d\hat{y}'}{dt} = \vec{\omega} \times \hat{y}'; \quad \frac{d\hat{z}'}{dt} = \vec{\omega} \times \hat{z}' \quad (2.41)$$

where in this case, $\vec{\omega} = -\omega \hat{z}$.

Combining Equations (2.40) and (2.41), we get the following:

$$\left[\frac{d\vec{M}}{dt} \right]_{lab} = \left[\frac{d\vec{M}}{dt} \right]_{rot} + \vec{\omega} \times \vec{M}_{rot} . \quad (2.42)$$

Because $\vec{M}_{rot} = \vec{M}$, it can also be written as

$$\left[\frac{d\vec{M}}{dt} \right]_{lab} = \left[\frac{d\vec{M}}{dt} \right]_{rot} + \vec{\omega} \times \vec{M} \quad (2.43)$$

Solving for the change of \vec{M} in the rotating frame, or $\left[\frac{d\vec{M}}{dt}\right]_{rot}$, this becomes

$$\left[\frac{d\vec{M}}{dt}\right]_{rot} = \left[\frac{d\vec{M}}{dt}\right]_{lab} - \vec{\omega} \times \vec{M}. \quad (2.44)$$

Substituting Equation (2.39) into (2.44) gives

$$\left[\frac{d\vec{M}}{dt}\right]_{rot} = \gamma \vec{M} \times \left(\vec{B} + \frac{\vec{\omega}}{\gamma}\right). \quad (2.45)$$

The effective magnetic field that the magnetization vector experiences in the rotating frame is

$$\vec{B}_{eff} = \vec{B}_{rot} + \frac{\vec{\omega}}{\gamma} \quad (2.46)$$

Therefore if we let $\vec{B}_{rot} = B_o \hat{z}$ and $\vec{\omega} = -\gamma B_o \hat{z}$, then $\vec{B}_{eff} = B_{rot} - \frac{\gamma B_o \hat{z}}{\gamma} = B_o \hat{z} - B_o \hat{z} = \mathbf{0}$.

This shows that the apparent longitudinal field vanishes and \vec{M}_{rot} appears to be stationary in the rotating frame. Therefore the full Bloch equation (Equation (2.38)) can be expressed in the rotating frame as

$$\frac{d\vec{M}_{rot}}{dt} = -\frac{M_x \hat{x} + M_y \hat{y}}{T_2} - \frac{M_z \hat{z} - M_o \hat{z}}{T_1} \quad (2.47)$$

because $\gamma \vec{M}_{rot} \times \vec{B}_{eff} = 0$.

2.2.4 Flip Angle

The angle that the magnetization vector \vec{M} rotates away from the z-axis because of the application of an RF pulse is called the flip or tip angle. It is defined as the angle between the \vec{M} and the z-axis (see Figure 2.7). The equation for the flip angle is given as

$$\alpha = \int_0^{\tau} \gamma B_1^e(t) dt \quad (2.48)$$

where α is the flip angle, and $B_1^e(t)$ is the RF pulse envelope function, and τ is the duration of the RF pulse.

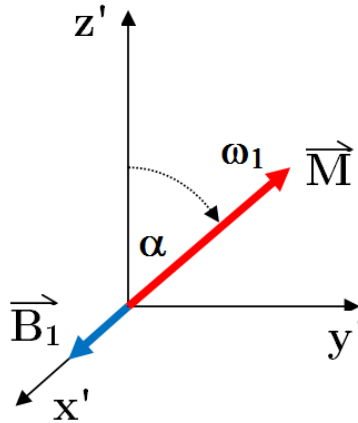


Figure 2.7: Flip angle. With an applied external magnetic field B_1 , the net magnetization vector \vec{M} flips through an angle α [1].

With an applied external magnetic field, $\vec{B}_1 = B_1 \hat{x}'$, the magnetization vector \vec{M} rotates through an angle of α and rotates in the y' and z' plane.

For a rectangular pulse of duration τ , this angle reduces to the following:

$$\alpha = \gamma B_1^e \tau \quad (2.49)$$

The flip angle depends on the pulse duration of τ and strength of the B_1 field. The frequency of B_1 is the same as the Larmor frequency which means that the pulse is on-resonance. Off-resonance pulses also exist in MR but are beyond the scope of this thesis.

An RF B_1 pulse that rotates the magnetization vector \vec{M} through the angle α is referred to as an alpha-pulse. For example, rotating \vec{M} by 90° is referred to as a 90° pulse or $\frac{\pi}{2}$ -pulse, and rotating \vec{M} by 180° is referred to as a 180° pulse or π -pulse. In general, the amount of transverse magnetization M_{xy} after an α -pulse is given by:

$$M_{xy} = |\vec{M}| \cdot \sin(\alpha) \quad (2.50)$$

Using Equation (2.50), the 90° pulse results in the maximal signal at:

$M_{xy} = M_o \sin(90^\circ) = M_o$, and the 180° pulse results in a minimal signal at:

$M_{xy} = M_o \sin(180^\circ) = 0$, and is shown on Figure 2.8.

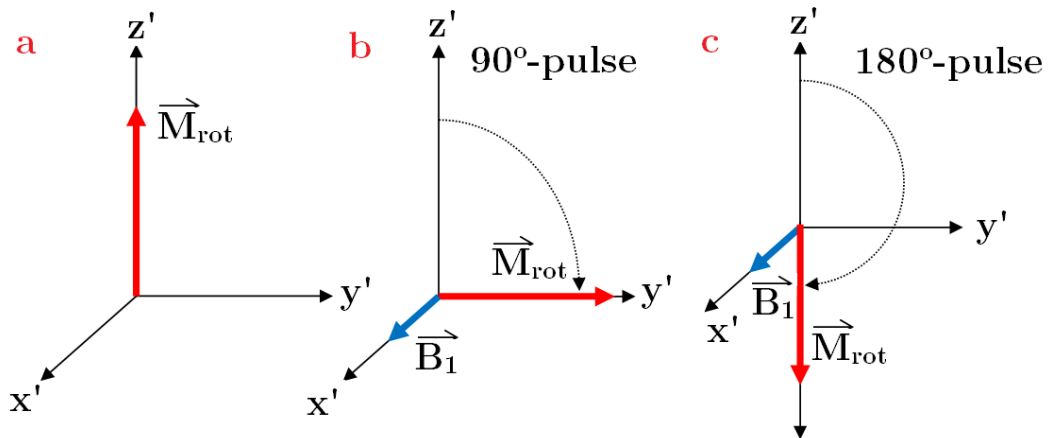


Figure 2.8: Net Magnetization vector \vec{M}_{rot} in the rotating frame at: (a) equilibrium, (b) following a 90° pulse, and (c) following a 180° pulse [1].

2.3 Free Induction Decay

After the excitation RF pulse, the transverse magnetization M_{xy} rotates at Larmor frequency and it induces a damped sinusoidal voltage known as the free induction decay (FID) (Figure 2.9).

The magnitude of this FID signal depends on the flip angle (Equation (2.50)), the total number of spins in the sample, as well as the strength of the magnetic field (Equation (2.27)). The signal decays as a result of the loss of phase coherence between the individual magnetic moments due to the inhomogeneity of the field, which is characterized by the T_2^* decay (described in Section (2.6)). The FID signal is proportional to:

$$S(t) \propto \sin(\alpha) \int_{-\infty}^{\infty} \rho(\vec{r}) e^{-\frac{t}{T_2(\vec{r})}} e^{-i\omega(\vec{r})t} d\vec{r} ; t > 0 \quad (2.51)$$

where $\rho(\vec{r})$ is the spatial density. After a 90° pulse, a homogeneous sample with a single resonant frequency ω_0 , will reduce to

$$S(t) \propto M_0 e^{-\frac{t}{T_2}} e^{-i\omega_0 t} \quad (2.52)$$

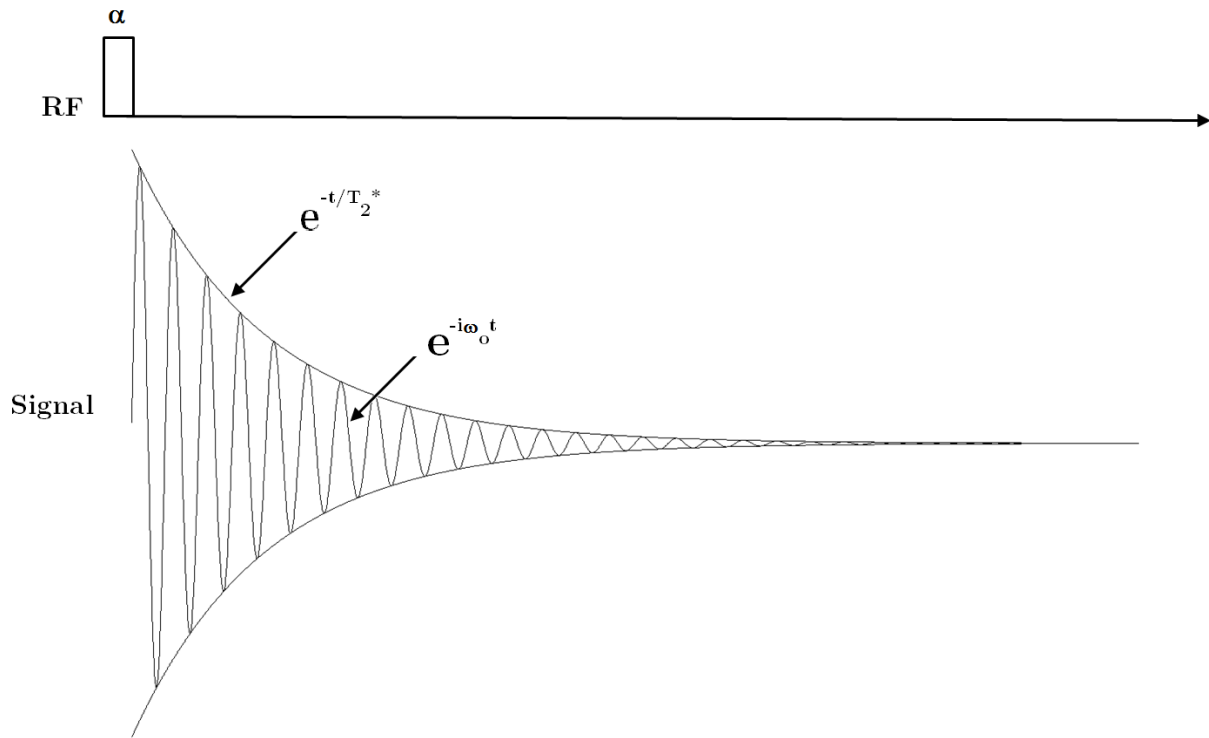


Figure 2.9: The FID signal after an α -pulse. Due to the local field inhomogeneities, the signal is approximated by an exponential decay with the time constant, T_2^* . In this figure ω_0 , is small for visual clarity [1].

2.4 Signal Detection

MR detection is based on Faraday's law of electromagnetic induction where the voltage generated in a coil is proportional to the rate at which the magnetic flux through a coil changes. According to Faraday's law of induction and the principles of reciprocity, a time varying magnetization $\vec{M}(\vec{r}, t)$ will induce a voltage $V(t)$ in a receiver coil which is often regarded as the raw NMR signal [4] expressed as follows:

$$V(t) \propto -\frac{\partial}{\partial t} \int_{object} \vec{B}(\vec{r}) \cdot \vec{M}(\vec{r}, t) d\vec{r} \quad (2.53)$$

where $\vec{B}(\vec{r})$ is the magnetic field at position \vec{r} .

To accommodate later signal processing stages as well as detect a higher signal-to-noise ratio, quadrature detection is often used, in which two orthogonal receiver coils detect signal yielding a complex signal

$$S(t) = S_1(t) + i S_2(t) \quad (2.54)$$

with one output being treated as the real part (x-axis) and the other the imaginary part (y-axis).

If we assume that there is a homogeneous magnetic field in the receiver coil, the signal can be expressed as follows [4]:

$$S(t) \propto \int_{object} M_{xy}(\vec{r}, 0) e^{i\omega(\vec{r})t} d\vec{r} \quad (2.55)$$

where $\omega(\vec{r})$ is the frequency of the rotating frame. Assuming that the spatial density of hydrogen nuclei, $\rho(\vec{r})$ is proportional to the longitudinal magnetization at thermal equilibrium:

$$\rho(\vec{r}) \propto M_o(\vec{r}) . \quad (2.56)$$

and the transverse magnetization after 90° pulse becomes

$$M_{xy}(\vec{r}, 0) \propto \rho(\vec{r}) \quad (2.57)$$

then the signal is related to the spatial distribution of ^1H nuclei and their frequencies. This can be expressed using Equation (2.55) as

$$S(t) \propto \int \rho(\vec{r}) e^{-i\omega(\vec{r})t} d\vec{r} \quad (2.58)$$

and shows that $S(t)$ and $\rho(\vec{r})$ are Fourier transform pairs.

The SNR for an image can be measured from the following equation:

$$SNR = 0.655 * \frac{S}{\sigma} \quad (2.59)$$

This equation is a statistical image-based measure representing the ratio of the average signal intensity in a region of interest (ROI) S , and the standard deviation σ , of the signal intensity in the background (noise region) of the image [8, 9]. The noise region is typically chosen in the air surrounding the object of interest where the sample's magnetic resonance signal should be zero.

2.5 Gradients

The signals produced from an FID as described in Section 2.4 do not provide any spatial information. To introduce this spatial information, gradient coils are used to produce another set of magnetic fields that can alter the B_o field and thus create an image. The gradients cause the magnetic field strengths to vary linearly with position along a particular axis in order to make the Larmor frequency depend on position within the magnet. The application of gradient fields for spatial localization in MRI was first outlined by Lauterbur in 1973 [10].

The gradient field \vec{B}_G is a linear, position dependent, inhomogeneous field whose z-component varies linearly along a specific direction, causing the protons to alter their precessional frequency corresponding to their position along the applied gradient field in a known and predictable way.

The gradient system consists of the three gradient coils, referred to as the x-, y- and z-gradient coils which would ideally produce their respective gradient fields. These gradients are

$$\begin{aligned} G_x &= \frac{\partial B_{G,z}}{\partial x} \\ G_y &= \frac{\partial B_{G,z}}{\partial y} \\ G_z &= \frac{\partial B_{G,z}}{\partial z} \end{aligned} \quad (2.60)$$

It is important to note that for each case, the magnetic field produced by the gradient coil has components in the x-direction ($B_{G,x}$) and y-direction ($B_{G,y}$), but these components are ignored for the experiments performed in this thesis because the B_0 field is very strong in the z-direction, and therefore $B_{G,z}$ is often used interchangeably with B_G .

The total magnetic field in the presence of a gradient field is given by

$$\vec{B}_z = (B_0 + B_{G,z})\hat{z} \quad (2.61)$$

and in the case where all three gradient coils are turned on simultaneously, the total gradient field is given by

$$B_{G,z} = G_x x + G_y y + G_z z \quad (2.62)$$

Alternatively, these gradient coils can be turned on individually as in the Equations (2.60).

These three gradients are grouped into a gradient vector:

$$\vec{G} = (G_x, G_y, G_z) = G_x \hat{x} + G_y \hat{y} + G_z \hat{z} \quad (2.63)$$

The direction of \vec{G} is called the *gradient direction* of $\vec{B}_{G,z}$ (or \vec{B}_G). Because the gradients is a linearly position-dependent magnetic field, it can be written as

$$\vec{B}_z = \vec{G} \cdot \vec{r} \quad (2.64)$$

2.5.1 Slice Selective Gradients

In MRI the most common approach to generate a single slice or 2D image is to excite only the protons lying in the desired image plane (Figure 2.10). This is done with a magnetic field gradient and a shaped RF pulse. Figure 2.10 shows there are three cases where slice selection excites slices along the x-, y-, and z-axes and the corresponding slice equations are given respectively, by

$$\begin{aligned} |x - x_o| &\leq \frac{\Delta x}{2} \\ |y - y_o| &\leq \frac{\Delta y}{2} \\ |z - z_o| &\leq \frac{\Delta z}{2} \end{aligned} \quad (2.65)$$

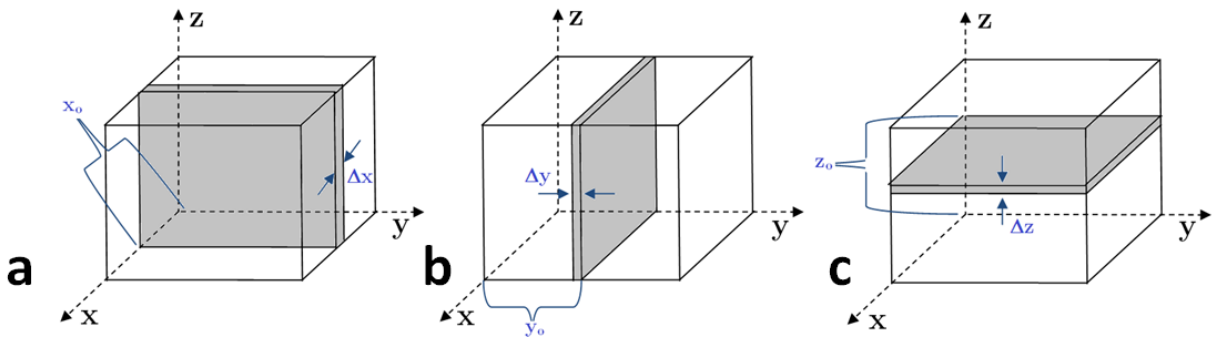


Figure 2.10: Parameters characterizing a slice in the special case where the image is perpendicular to the (a) x-axis, (b) y-axis, and (c) z-axis. The slice equations are given respectively in Equation (2.65) [1, modified from 4].

Slice selective gradients make the resonant frequency dependent on position by specifically varying along the slice select direction ($\vec{\mu}_s$) linearly. It should be noted that one of the unique beneficial features of MRI is the slice direction can be made to be any arbitrary direction. For simplicity and by convention, the slice selection direction will be taken as the z-direction for this chapter. To excite a slice along the z-axis during an RF pulse, a linear gradient field needs to be applied along the z-axis

$$\vec{G}_{ss} = (0,0, G_z) = G_z \hat{z} \quad (2.66)$$

This RF pulse is called a slice selective RF pulse. This changes the Larmor frequency of the spins so that it varies linearly with position along the z-axis:

$$\omega(z) = \omega_o + \gamma G_z z \quad (2.67)$$

or
$$f(z) = f_o + \bar{\gamma} G_z z \quad (2.68)$$

Ideally, a rectangular slice profile is desired in the image plane. In the frequency domain after a Fourier transform, the sinc RF pulse (Equation (2.32)) yields a rectangular profile

$$p(f) = \prod \left(\frac{f - f_c}{\Delta f} \right) e^{\frac{i2\pi(f-f_c)\tau_p}{2}} \quad (2.69)$$

where $\prod \left(\frac{f-f_c}{\Delta f} \right)$ is the boxcar function with a frequency bandwidth Δf centred on the frequency f_c . If we define the centre of our slice as z_o and the desired thickness as Δz , then the bandwidth Δf , and central frequency f_c are given as

$$\Delta f = \bar{\gamma} G_z \Delta z \quad (2.70)$$

$$f_c = f_o + \bar{\gamma} G_z z_o \quad (2.71)$$

where Δf determines the slice thickness, and f_c determines the slice selection.

Equation (2.69) can be rewritten with Equations (2.70) and (2.71) to be defined along the z-direction, with a slice of thickness Δz that is centred at $z = z_0$:

$$p_s(z) = \prod \left(\frac{z - z_0}{\Delta z} \right) e^{i\gamma G_z (z - z_0) \tau_p / 2} \quad (2.72)$$

Using these equations, changing the bandwidth (Figure 2.11) or the gradient strength (Figure 2.12) can adjust the slice thickness. For example, slice thickness can be made smaller by decreasing the bandwidth or increasing the gradient strength. The slice thickness can be made larger by increasing the bandwidth or decreasing the gradient strength. With a chosen slice width, changing the gradient strength changes the bandwidth (Figure 2.13).

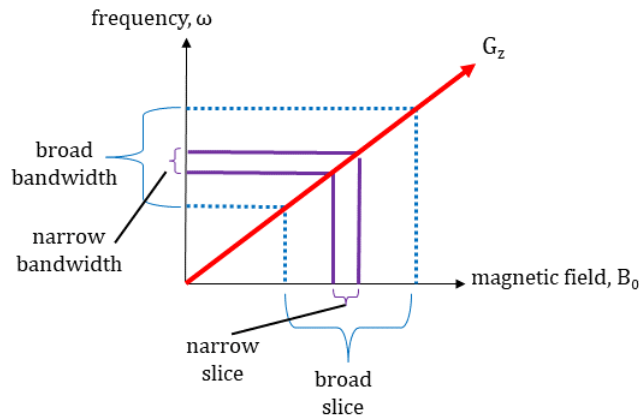


Figure 2.11: For a given gradient field strength: an RF pulse with a narrow bandwidth excites protons over a narrower slice of tissue, and a broad bandwidth excites a thicker slice [1].

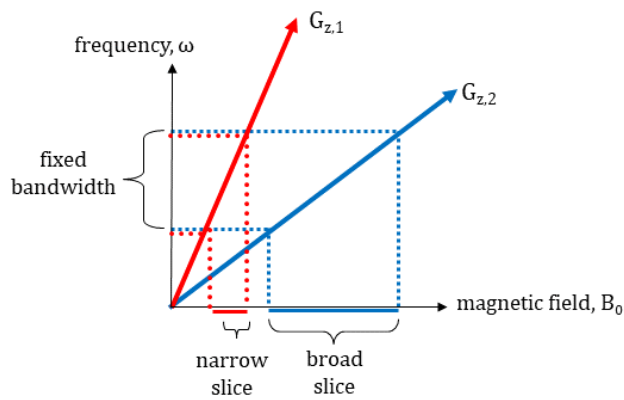


Figure 2.12: For a fixed bandwidth, the magnitude of the gradient strength (slope) determines the slice thickness. Decreasing the gradient strength ($G_{z,2}$) results in a wider slice thickness [1].

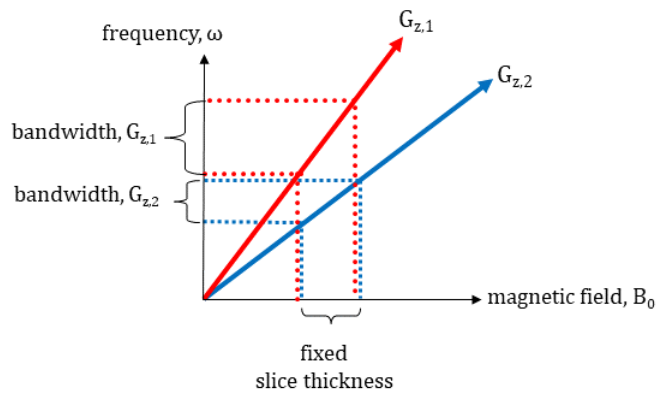


Figure 2.13: For a fixed slice thickness, the magnitude of the gradient strength (slope) increases with an increased bandwidth. The larger gradient strength, $G_{z,1}$ produces an increased bandwidth, when compared to the bandwidth of $G_{z,2}$ at a lower gradient strength [1].

After a slice select 90° pulse and gradient, the phase of the spins will depend on position and the relationship between frequency and position is:

$$\omega = \gamma G_z z \quad (2.73)$$

The slice selective gradient pulse duration is the same as the 90° pulse duration, t_{90} . During half this time (Figure 2.14), the spins acquire a phase dependent on position, according to

$$\Delta\phi = \omega\Delta t = \gamma G_z z \cdot \frac{t_{90}}{2} \quad (2.74)$$

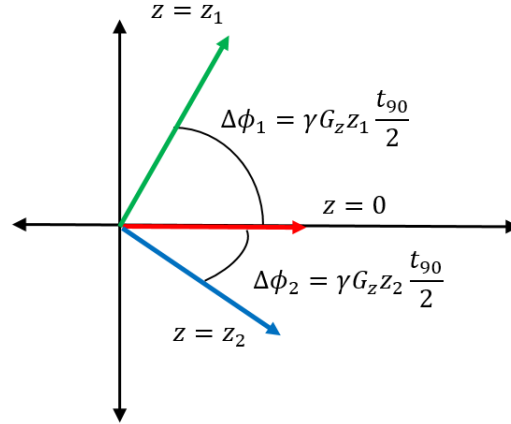


Figure 2.14: The slice selective gradient pulse, during half the time of the 90° pulse duration, spins acquire a phase that is dependent on positions. In this figure, $z_1 > 0 > z_2$, $\Delta\phi_1 > 0 > \Delta\phi_2$ [1].

To regain phase coherence, a slice refocusing gradient is added after the completion of the RF pulse (Figure 2.15). The gradient has an opposite sign, and its duration is half that of the slice select gradient. Thus the phase added during the refocusing pulse is given as

$$\Delta\phi = \omega\Delta t = -\gamma G_z z \cdot \frac{t_{90}}{2} \quad (2.75)$$

and therefore the net phase is given by the sum of the Equations (2.74) and (2.75) is zero.

In summary, the slice select gradient applied during RF pulse results in a proton excitation in a single phase, localizing the signal in the dimension orthogonal to the gradient. It is the first of the three gradients applied to the volume in question to create an image.

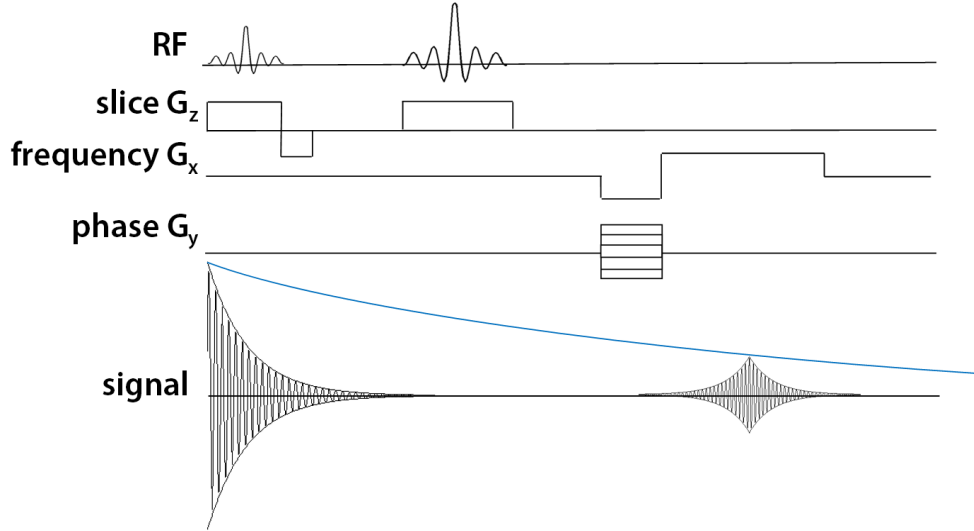


Figure 2.15: Image gradients for slice selection (section 2.5.1), frequency-encoding (section 2.5.3) and phase-encoding (section 2.5.2). The slice selective gradient pulse for the 180° pulse refocuses itself [1].

2.5.2 Phase Encoding Gradients

The phase encoding gradient is applied between the 90° and 180° pulses, or after the 180° pulse before the echo. It shifts the frequency of the spins for a time, T_{PE} , so that the phase acquired in this time depends on position. For simplicity, if we assume the phase encoding is in the y - direction, spins at different y -positions accumulate different phase angles after a time interval, T_{PE} . Therefore, the signal collected afterward will have an initial phase angle given by

$$\phi(y) = (\omega_o + \gamma G_y y) T_{PE} \quad (2.76)$$

$$\phi(y') = -\gamma G_y y' T_{PE} \quad (2.77)$$

where $G_y y$ is the phase encoding gradient, and Equations (2.76) and (2.77) represent the phase in the laboratory frame and rotating frame respectively. Because $\phi(y)$ is linearly related to the

signal location y , the signal is phase encoded. The received signal is the sum of all local phase encoded signals:

$$S(t) = \int_{object} dS(\vec{r}, t) = \left[\int_{object} \rho(y) e^{-i\gamma G_{PE} \cdot y \cdot T_{PE}} d\vec{r} \right] \cdot e^{-i\omega_0 t} \quad (2.78)$$

where the carrier signal ($e^{-i\omega_0 t}$) is removed after demodulation. Thus phase encoding is done by pre-frequency encoding the signal for a short time interval. Based on the equation above, this signal has the form of a non-encoded signal with a position-dependent initial phase angle, which can be adjusted with a variable phase encoding gradient strength or phase encoding interval.

2.5.3 Frequency Encoding Gradients

After the magnetic moments have been excited by a slice selective RF pulse, spatial information can be encoded into the signal during the free precession period. A gradient called the frequency encoding gradient (or readout gradient), is applied in one of the in-plane directions perpendicular to the slice gradient direction. By convention, and for ease of explanation, the frequency encoding direction will be taken as x -direction. This makes the oscillation frequency of the MR signal linearly dependent on its x -position, and it can be throughout the formation and decay of the spin echo signals as shown in Figure 2.15.

Consider an idealized one-dimensional object with spin distribution $p(x)$, if the magnetic field that the object experiences after an excitation is

$$B(x) = B_0 + G_x x \quad (2.79)$$

then the Larmor frequency at position x is

$$\omega(x) = \omega_o + \gamma G_x x \quad (2.80)$$

As a result, the FID signal generated locally from the spins is

$$dS(x, t) = \rho(x) dx \cdot e^{-i\gamma(B_o + G_x x)t} \quad (2.81)$$

This signal is frequency encoded because its oscillation frequency $\omega(x) = \gamma(B_o + G_x x)$ is linearly related to spatial location, where G_x is the frequency encoding gradient. The signal received from the object in the presence of the gradient is

$$S(t) = \int_{object} dS(x, t) \propto \left[\int_{-\infty}^{\infty} \rho(x) e^{-i\gamma G_x x t} dx \right] e^{-i\omega_o t} \quad (2.82)$$

After demodulation, or the removal of the carrier signal $e^{-i\omega_o t}$, the signal is reduced to

$$S(t) = \int_{-\infty}^{\infty} \rho(x) e^{-i\gamma G_x x t} dx \quad (2.83)$$

The frequency encoding gradient field causes the magnetic moments to lose phase coherence because each spin has a different frequency based on position. The gradient is applied for a given time T_{FE} , thus the phase acquired by a given spin at position x during this time is

$$\phi(x) = (\omega_o + \gamma G_x x) T_{FE} \quad (2.84)$$

$$\phi(x') = -\gamma G_x x' T_{FE} \quad (2.85)$$

where Equations (2.84) and (2.85) are in the laboratory frame and rotating frame respectively.

To make the net phase zero at the centre of the frequency encoding gradient, i.e. $t = \frac{T_{FE}}{2}$ when the echo is produced, a readout dephaser pulse is typically added before the readout pulse, and this pulse has half the duration and negative amplitude of the frequency encoding pulse (see Figure 2.15). This also means that the line of k-space is collected from $-k_{max}$ to $+k_{max}$.

2.6 Relaxation

As discussed in Section 2.2, in order to produce an MR signal the spin system needs to be perturbed using an external force, such as an RF pulse. Once this RF pulse is removed, the spin system will eventually return or recover to its initial equilibrium state via two processes; one known as *spin-lattice* or *longitudinal relaxation* and the other known as *spin-spin* or *transverse relaxation*. Spin-lattice or longitudinal relaxation is the term given for the exponential growth of M_z , wherein the spin system exchanges energy with the lattice which consists of the molecular arrangement and structure of the object. Once in equilibrium, the magnetization has its maximum value of M_0 and is aligned with the strong magnetic field taken in the z-direction (see Figure 2.16).

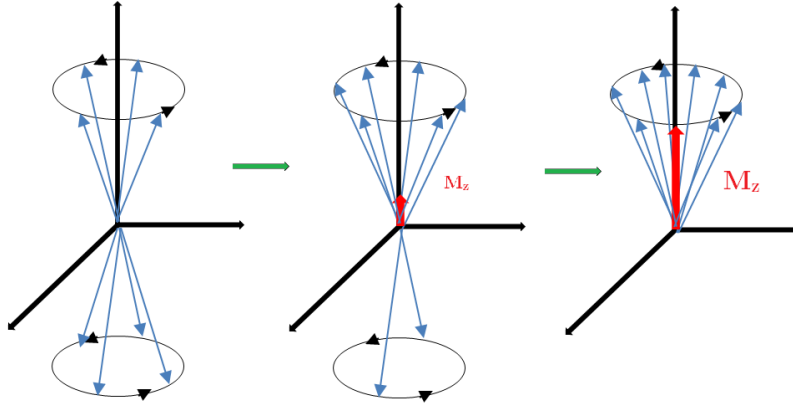


Figure 2.16: The magnetic moments will spontaneously return to a lower energy state (thermal equilibrium), and thus return the longitudinal magnetization M_z to its full value. The time constant for this is called T_1 [1, modified from 11].

The effect of spin-lattice or longitudinal relaxation can be described using the Bloch equation as

$$\frac{dM_z}{dt} = \frac{M_o - M_z}{T_1} \quad (2.86)$$

where M_z is the longitudinal magnetization recovered after a time t in an object, and T_1 is the spin-lattice or longitudinal relaxation time. The solution to this differential Equation (2.86) is given as

$$M_z(t) = M_z(0) \cdot e^{\left(\frac{-t}{T_1}\right)} + M_o \left[1 - e^{\left(\frac{-t}{T_1}\right)}\right] \quad (2.87)$$

where M_o is the longitudinal magnetization at equilibrium, and $M_z(0)$ is the initial value after the completion of the RF pulse. If the initial RF pulse is a 90° pulse, then $M_z(0) = 0$, which changes this equation to

$$M_z = M_o \left(1 - e^{-t/T_1}\right). \quad (2.88)$$

The M_z after a 90° pulse is shown in Figure 2.17.

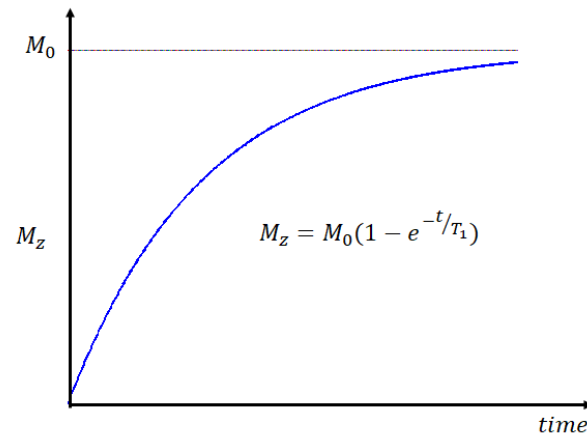


Figure 2.17: A T_1 curve, where $M_z(0) = 0$, which happens after a 90° pulse, for instance. The longitudinal magnetization becomes re-established in an exponential manner characterized by the time constant T_1 [1].

The component of magnetization in the transverse plane goes to zero via a process called *spin-spin relaxation* or *transverse relaxation*. This spin-spin or transverse relaxation is the term given to represent the spin-spin interactions that cause the loss of phase coherence due the intrinsic magnetic properties of the object. In this process, spins exchange energy amongst themselves and become less ordered, which corresponds to a loss of coherence to the system (Figure 2.18).

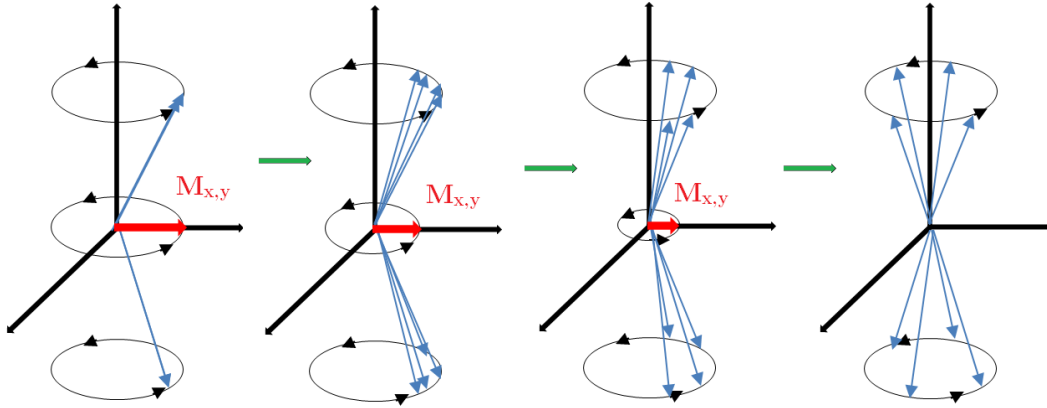


Figure 2.18: Spin-spin interactions cause the magnetic moments to dephase. The time constant for this is referred to as T_2 [1, modified from 11].

Similar to the equation for longitudinal magnetization (Equation (2.88)), the effect of spin-spin relaxation is described with the use of the Bloch equation as

$$\frac{dM_{xy}}{dt} = -\frac{M_{xy}}{T_2} \quad (2.89)$$

where M_{xy} is the transverse component of magnetization (xy-plane) as a function of time after the RF pulse, and T_2 is the spin-spin relaxation time, or transverse relaxation time.

A solution to Equation (2.89) is given as

$$M_{xy}(t) = M_{xy}(0) \exp\left(-\frac{t}{T_2}\right) \quad (2.90)$$

and is shown in Figure 2.19. For the case after a 90° pulse which sets $M_{xy}(0) = M_o$ this changes the equation to

$$M_{xy}(t) = M_o e^{-t/T_2} . \quad (2.91)$$

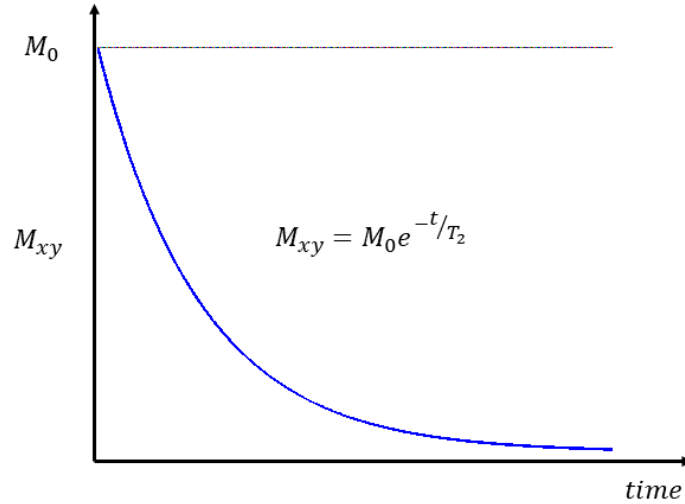


Figure 2.19: A T_2 decay curve for the magnetization after a 90° -pulse. The transverse magnetization decreases in an exponential manner characterized by the time constant T_2 [1].

The T_2 decay mechanisms are determined by the molecular structure of the sample. If the main magnetic field is not homogeneous, the loss of phase coherence may occur more rapidly than the spin-spin interactions themselves. When B_0 inhomogeneity is considered, the spin-spin decay constant, T_2 , is changed to T_2^* to take into account the extra dephasing which occurs due to the field inhomogeneities [12]. This T_2^* is often defined as

$$\frac{1}{T_2^*} = \frac{1}{T_2} + \frac{1}{T_2'} \quad (2.92)$$

where T_2' represents factors such as local field inhomogeneities that cause magnetization to dephase faster. This equation is an approximation of the real interactions but will suffice for the descriptions in this thesis.

2.7 Pulse Sequences

The spin density and relaxation constants T_1 and T_2 are all fundamental properties of tissues which can be exploited by MRI [4, 12, 13]. The T_1 - and T_2 - relaxation times are determined by the molecular structure of the tissues [13, 14]. The type of structure of the molecules in the tissue influences how protons either absorb or give off the energy into the surrounding molecular structure, and determines how fast the magnetic moments in the tissue will dephase. Energy transfer occurs most efficiently when the natural motional frequencies (translation, rotation and vibration) ω , of the protons are at Larmor frequency, ω_o (Equation (2.14)). The natural motional frequency of hydrogen depends on the physical state of the tissue, and is influenced by the atoms to which they are attached or are proximal. Atoms which are spaced further apart from one another produce higher natural motional frequencies and there are fewer spin-spin interaction between these atoms which cause slower dephasing and therefore give the tissue a long T_1 and long T_2 . Alternatively, atoms which are spaced closer together have lower natural motional frequencies, and dephasing occurs more rapidly due to more spin-spin interaction, producing a short T_1 and short T_2 .

Fluids, such as water (H_2O), have hydrogen protons that are spaced further apart from one another and produce natural motional frequencies much higher than the Larmor frequency for hydrogen, i.e. $\omega(H_2O) \gg \omega_o$, which results in a long T_1 . Also this distance between the protons causes slower dephasing, which produces a long T_2 . Solids, on the other hand have the opposite effect because the molecular structure is very compact this creates greater spin-spin interaction causing dephasing to occur more rapidly, producing a short T_2 . Solids also have lower natural motional frequencies which are lower than the Larmor frequency for hydrogen,

$\omega(\text{solids}) < \omega_o$, which produces a short T_1 . Intermediate molecules, such as fat, have natural motional frequencies that are close to the Larmor frequencies used for MRI, $\omega(\text{fat}) \approx \omega_o$, which produces short T_1 and T_2 .

Creating pulse sequences that emphasize these differences in tissues aids in the contrast sensitivity of MR images. One pulse sequence, the spin echo pulse sequence, will be discussed in this chapter because it is the basis of the diffusion pulse sequences used in the experiments presented in this thesis. The sequence is used to generate an echo which is a form of magnetic resonance signal that is produced from the refocusing of the transverse magnetization. The spin echo is a signal that is generated by multiple RF pulses.

The spin echo uses an RF excitation pulse that rotates the longitudinal magnetization (M_z) into the xy-plane, producing the maximal transverse magnetization (M_{xy}) which has the spins in phase coherence. Dephasing of the spins occurs and a FID signal emerges from this dephasing. In order to put the spins back into coherence, another RF pulse is applied along the transverse direction, inverting the phases of the spin system causing the spins to rephase, which produces the signal or 'echo'.

Gradient echoes were previously explained in Section 2.5, now spin echoes will be explained in the next section, Section 2.7.1.

2.7.1 Spin Echo

The spin echo pulse sequence is a commonly used sequence in MRI. An initial 90° RF pulse is applied at time $t=0$, which flips the spins into the xy -plane, producing the maximal transverse magnetization M_{xy} and places the spins in phase coherence (Figure 2.20a). The FID signal appears and exponentially decays with T_2^* relaxation due to the magnetic field inhomogeneity, in turn causing the spins to be out of phase. Typically this FID is ignored and each spin will acquire a different phase based on its surrounding magnetic field inhomogeneities (Figure 2.20b).

After a time delay, τ , a 180° RF pulse (known as the *refocusing pulse*) is applied along a transverse direction such as \hat{x}' which inverts the phases of the spin system (Figure 2.20c). During the next time period, τ , the spins rephase. This 180° pulse eliminates the dephasing that was caused by the T_2^* effect from the first RF pulse. The spins are rephased and produce a measureable signal at a time equal to the time of echo, termed the echo time or time of evolution (TE), so named because of the "echo" signal (Figure 2.20d). The echo at time TE is at lower amplitude than the FID because of the T_2 relaxation.

Digital sampling and acquisition of the signal occurs just before and after the peak amplitude of the echo (centred at the time TE). At a time TR , or repetition time, after the 90° pulse, another 90° pulse is applied, and the sequence repeated to acquire more signal (Figure 2.20).

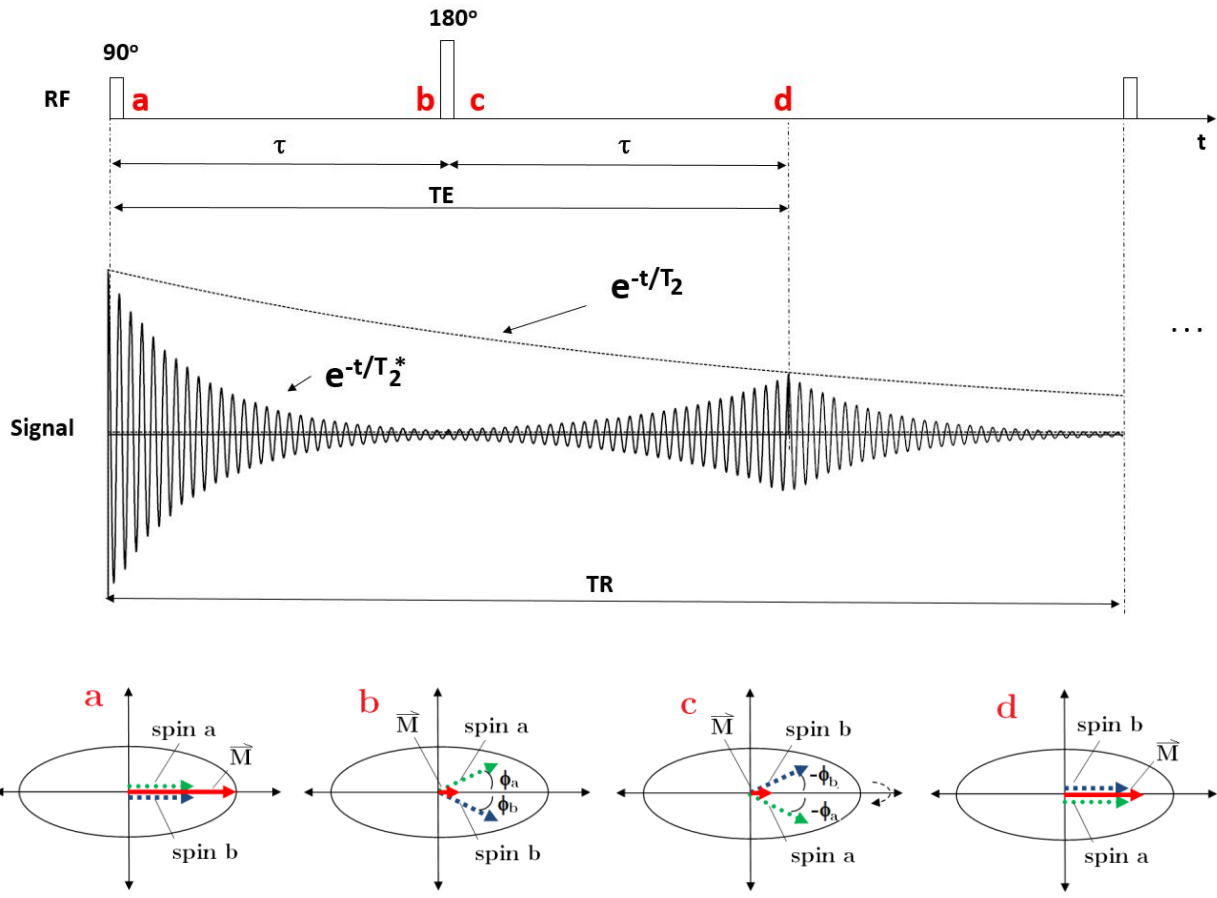


Figure 2.20: Spin echo sequence. After a 90° pulse the 'spin a' will precess faster than \vec{M} and 'spin b' will precess slower than \vec{M} which results in a T_2^* decay (shown in part b). At $t = \tau$, a 180° pulse flips the spins in the opposite planes (shown in part c), which causes both the 'spin a' and 'spin b' precess towards \vec{M} , resulting in a growth in T_2^* . The spins rephase at $t = 2\tau = TE$ with a signal amplitude weighted by the T_2 constant (shown in part d). The magnitude \vec{M} at this stage is much smaller than it was prior to the 90° pulse [1].

Typically a few dummy scans (or pulse sequences where signals were not acquired) are used to get the system in a form of steady state before signal is acquired. For spin echo sequences, the parameters of interest are TR and TE . It can be shown that the signal in the spin echo sequence is given by [15]

$$S(t) \propto M_{xy}(t) = M_{xy}(0) \left\{ 1 - 2 \cdot e^{\left[\frac{-(TR - \frac{TE}{2})}{T_1} \right]} + e^{-\left(\frac{TR}{T_1}\right)} \right\} \times e^{-\frac{TE}{T_2}} . \quad (2.93)$$

Equation (2.93) shows that TE influences the T_2 -weighting of the image, and TR influences the T_1 -weighting of the image (assuming $TE \ll TR$). The effects of TE and TR on image contrast are summarized in Table 2.3, with examples of T_1 -weighted, T_2 -weighted, and PD-weighted MR images shown in Figure 2.21.

Table 2.3: The effect of TR and TE for a spin echo image.

	TE short	TE long
TR short	T_1 -weighted	not used
TR long	PD-weighted	T_2 -weighted

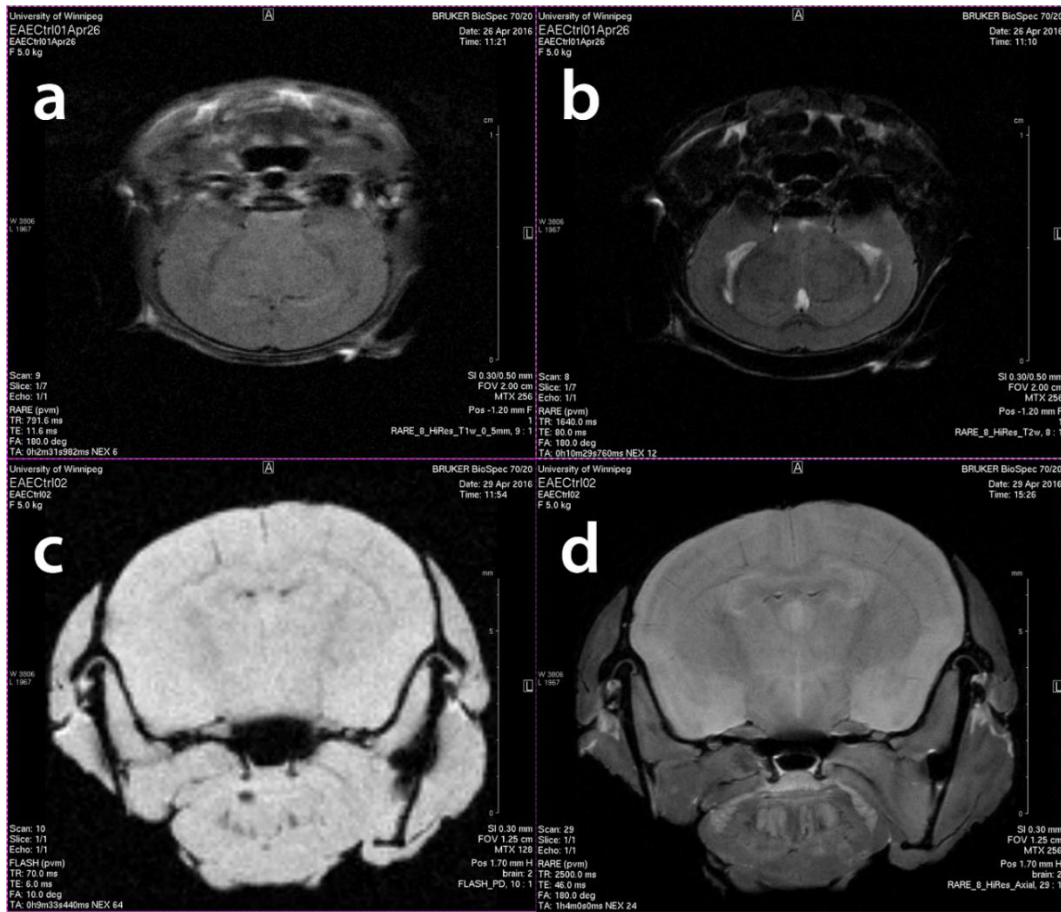


Figure 2.21: Example MR images of the brains of two mice. One set of images was collected from the same slice in a mouse *in vivo* (a, b), and the second set of images was collected from a different slice in a mouse *ex vivo* (c, d). *In vivo* MR images of mouse 1 are (a) a T_1 -weighted MR image, and (b) a T_2 -weighted MR image oriented as if the mouse was lying on its back facing you. *Ex vivo* MR images of mouse 2 are (c) a PD-weighted MR image, and (d) a T_2 -weighted MR image oriented as if the mouse was lying on its belly facing you. These images show the difference in contrast between T_1 -weighted, T_2 -weighted, and PD-weighted images. For instance, comparing (a) and (b) shows that the T_1 -weighted image at 7 T has less contrast than the T_2 -weighted image. The ventricles, for instance, are clearly visible in the T_2 -weighted image and the white matter-grey matter contrast is more apparent in the T_2 -weighted image. Comparing (c) and (d) shows that there is more contrast in the T_2 -weighted image than in the PD-weighted image. For instance, the brain is hyper-intense to the surrounding muscles in the T_2 -weighted image and of similar intensity in the PD-weighted image. Comparing the *in vivo* and *ex vivo* images also provides some important information. The resolution and signal-to-noise ratio (SNR) of the *ex vivo* images was better than that of the *in vivo* images because more time could be spent collecting the images.

Given that the images presented for the experiments in this thesis are T_2 -weighted in addition to being diffusion-weighted (see Chapter 3), only the T_2 -weighted spin echo sequence is discussed here.

2.7.2 T_2 -Weighting

To minimize the T_1 differences in the tissues, and accentuate the T_2 differences in a spin echo image [14] a relatively long TR is used (Figure 2.20). This allows for a significant longitudinal recovery so that the transverse magnetization differences are those mainly resulting from variations in the T_2 values of tissues with a long TR. By using a long TR, Equation (2.93) reduces to

$$S(t) = M_0 e^{-\left(\frac{TE}{T_2}\right)}. \quad (2.94)$$

A T_2 -weighted signal from the spin echo sequence is the second echo (produced by the 180° pulse) of a long TR spin echo pulse sequence. In T_2 -weighted images of the brain at 7T, CSF appears brightest at the longest T_2 , than fat which has the shortest T_2 . Grey and white matter have intermediate T_2 values, with grey matter having a lower T_2 than white matter. Crémillieux, et al. [16] measured at 7T, the T_2 values of CSF and fat with values of 125.1 ± 9.2 ms and 27.4 ± 1.3 ms, respectively. Guilfoyle et al. [17], measured at 7T, the T_2 values of grey and white matter, with $41 \pm 3 / 38 \pm 2$ ms for grey matter (hippocampus/cortex), and 37 ± 2 ms for white matter (corpus callosum). The value of TE is chosen to optimize differences between tissue types. For

example, if the desire is to have the largest contrast between fat and brain tissue, then a TE value between the T_2 values of fat and brain should be chosen.

2.8 k-space Data Acquisition and Image Reconstruction

Ljunggenen [18] and Tweig [19] independently introduced k-space formalism in 1983 when both showed that the demodulated MR signal $S(t)$ generated by freely precessing nuclear spins in the presence of a linear magnetic field gradient \vec{G} equals the Fourier transform of the effective spin density.

In the rotating frame, the Larmor frequency can be written as a function of position vector \vec{r} and the gradient vector \vec{G} (Equation (2.63), where

$$\omega(\vec{r}) = \gamma (\vec{G} \cdot \vec{r}) . \quad (2.95)$$

Using Equation (2.58), this produces the signal in the form of a Fourier transform

$$S(t) \propto \int \rho(\vec{r}) e^{-i\gamma(\vec{G} \cdot \vec{r})t} d\vec{r} . \quad (2.96)$$

A reciprocal space vector can be defined as

$$\vec{k} = \frac{\gamma \vec{G} t}{2\pi} \quad (2.97)$$

Using this definition of \vec{k} , the signal can be rewritten as

$$S(\vec{k}) \propto \int \rho(\vec{r}) e^{-i2\pi\vec{k}\cdot\vec{r}} d\vec{r} \quad (2.98)$$

where $\rho(\vec{r})$ and $S(\vec{k})$ are Fourier transform pairs and therefore can be written as

$$\rho(\vec{r}) \propto \int S(\vec{k}) e^{-i2\pi\vec{k}\cdot\vec{r}} d\vec{k} . \quad (2.99)$$

The signal $S(\vec{k})$ is detected in the k-space domain of Fourier transform into the spatial domain function, $\rho(\vec{r})$. In 2-dimensions [4], $\rho(\vec{r})$ become $\rho(x, y)$ and $S(\vec{k})$ and is expressed as

$$S(k_x, k_y) \propto \iint_{-\infty}^{\infty} \rho(x, y) e^{-2\pi(k_x x + k_y y)} dx dy \quad (2.100)$$

where k_x, k_y are defined in Equation (2.101). The reciprocal space or k-space can be transversed by varying \vec{G} or t with the direction of the transverse set by the sign of \vec{G} .

Prior to image reconstruction for 2D planar imaging, the raw data acquired from the pulse sequences are stored in a 2-dimensional matrix called the k-space matrix, with k defined in Equation (2.97). The z-direction is the slice direction with this definition the components of the vector k can be written as the equations:

$$k_x = \frac{\gamma}{2\pi} G_x t \quad \text{and} \quad k_y = \frac{\gamma}{2\pi} G_y t \quad (2.101)$$

The data acquired at different phase and frequency values are placed into the matrix in a location based on k-values. A line of data in k-space is directly related to the gradient across the object being imaged. Continuing with the previous convention, the x-direction is taken as the

frequency encoding direction, and y -direction as the phase encoding direction. When the frequency encoding gradient is switched on during acquisition, a series of points are acquired corresponding to the various frequencies present at a particular phase value k_y and slice position, z , creating a horizontal line of voxels in k -space along the k_x -axis. As the values of k_y change, the k -space data populates the matrix k_x -line by k_x -line. Every point in k -space contains part of the information for the complete image.

Figure 2.22 shows how the lines of data in k -space are related to the gradients. In this simple spin echo pulse sequence, the phase-encoding and frequency dephaser gradients are switched on at the same time. The frequency dephaser gradient (Figure 2.22(i)) is in the negative direction and therefore moves the k_x value to the left of centre. The first phase gradient is applied at the maximum negative value so that it moves to the lowest k_y value (Figure 2.22a). This is followed by the frequency-encoding gradient (Figure 2.22(ii)) with twice the area as the frequency dephaser gradient (Figure 2.22(i)) and in the positive direction. This causes a gradient echo to occur which samples a line of k -space. A crusher gradient is then used to eliminate any unwanted signal (such as from the FID) before the next acquisition occurs. For each line of k -space, the phase-encoding gradient increases by Δk_y and this sequence is repeated until all lines of k -space are acquired (Figure 2.22(b-d)).

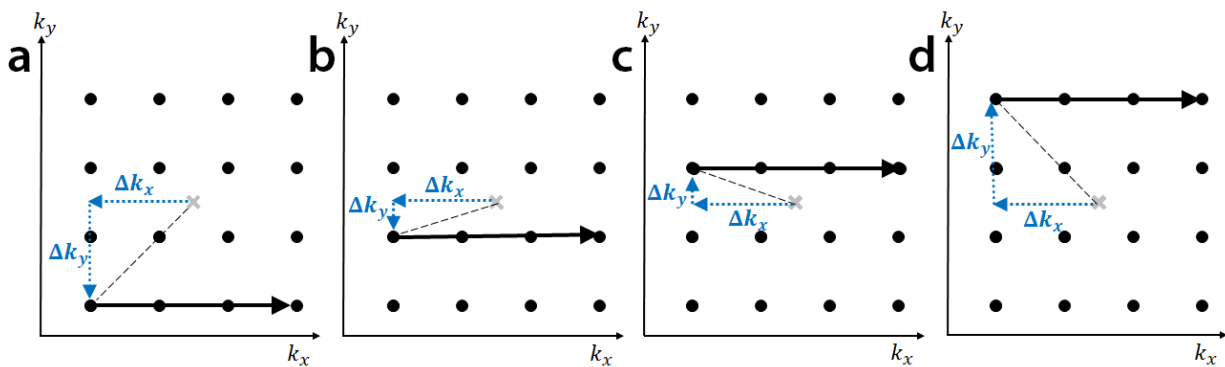
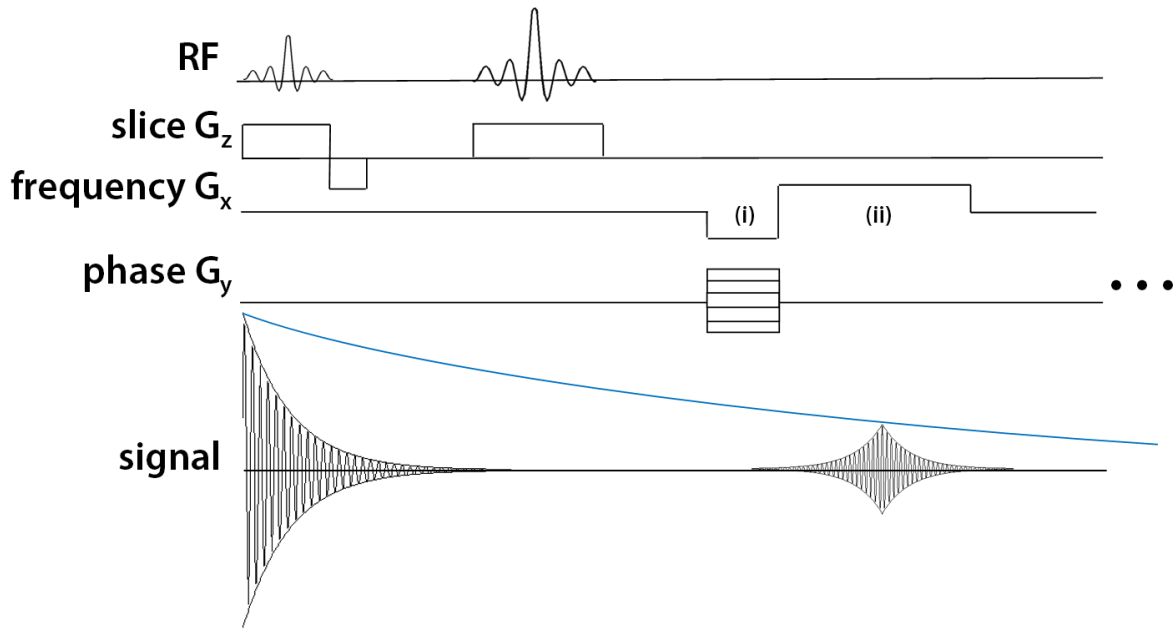


Figure 2.22: A schematic that shows how the lines of data in k-space are related to the gradients [1]. Phase-encoding and frequency dephaser gradients are switched on simultaneously. (a) The frequency dephaser gradient (i) is in the negative direction and moves the k_x value left of centre. The first gradient is applied at the maximum negative value, moving k_y to the lowest value. This is followed by the frequency-encoding gradient (ii) which is in the positive direction and twice the area of (i). This causes a gradient echo to occur which samples a line of k-space. A crusher gradient is then used to eliminate any unwanted signals prior to the next acquisition. For each line of k-space, the phase-encoding gradient increases by Δk_y , and this sequence is repeated until all lines of k-space are acquired (b-d).

In k-space, the outer rows of the matrix correspond to the higher spatial frequencies, which provide information regarding the borders and contours of the image, whereas the lower spatial

frequencies are found closer to the centre of the matrix, and represent the general contrast of the image. For a choice of field of view (FOV), the read and phase gradient strength and pulse times are defined by the following relationships [1, 14, 20, 21]:

$$\begin{aligned} FOV_x &= \frac{1}{\Delta k_x} = \frac{2\pi}{\gamma G_x \Delta t}, \\ FOV_y &= \frac{1}{\Delta k_y} = \frac{2\pi}{\gamma G_y \Delta t}. \end{aligned} \quad (2.102)$$

The maximum value of k, or equivalently, the number of phase and frequency encoding steps sampled determines the resolution:

$$\text{Resolution}_x = \Delta x = \frac{1}{|k_{x_{max}}|} = \frac{1}{N_x \Delta k_x} \quad (2.103)$$

$$\text{Resolution}_y = \Delta y = \frac{1}{|k_{y_{max}}|} = \frac{1}{N_y \Delta k_y} \quad (2.104)$$

The proton density $\rho(\vec{r})$, weighted by T_1, T_2 , can be mapped by measuring the NMR signal, $S(\vec{k})$, over all k-space and taking the Fourier transform. In other words, as time progresses the signal traces out a trajectory in k-space so that the $S(\vec{k})$ can be measured. The spin density $\rho(\vec{r})$ weighted for the effects of T_1 preparation, T_2 decay, dephasing due to field inhomogeneity, etc, and any other phenomena that affect the amount of transverse magnetization available to induce signal in the RF pulse can be calculated from the Fourier transform of $S(\vec{k})$ to make an image.

References

1. S. L. Herrera. "Magnetic Resonance Imaging and Magnetic Resonance Spectroscopy Characterize a Rodent Model of Covert Stroke," Masters Thesis, Dept. of Physics & Astronomy. University of Manitoba, Winnipeg, MB, 2012.
2. E. M. Purcell, H. C. Torrey, and R. V. Pound, "Resonance absorption by nuclear magnetic moments in a solid," *Physical Review*, vol. 69, no. 1-2, p. 37, 1946.
3. F. Bloch, "Nuclear induction," *Physical Review*, vol. 70, no. 7-8, p. 460, 1946.
4. Z.-P. Liang and P. C. Lauterbur, *Principles of Magnetic Resonance Imaging: A Signal Processing Perspective*. New York: Wiley-IEEE Press, 2000.
5. M. Puddephat. (2010). *Principles of Magnetic Resonance Imaging* [Online]. Available: <http://www.mikepuddephat.com/Page/1603/Principles-of-magnetic-resonance-imaging>
6. L. G. Hanson, "Is quantum mechanics necessary for understanding magnetic resonance?," *Concepts in Magnetic Resonance Part A*, vol. 32, no. 5, pp. 329-340, 2008.
7. S. Clare. (2006). *Functional MRI: Methods and Applications - Chapter 2* [Online]. Available: http://users.fmrib.ox.ac.uk/~stuart/thesis/chapter_2/chapter2.html
8. J. D. Thiessen, "Development and application of quantitative MRI methods for assessing white matter integrity in the mouse brain," Ph.D. dissertation, Dept. of Physics & Astronomy. University of Manitoba, Winnipeg, MB, 2012.
9. S. B. Reeder, "Measurement of signal-to-noise ratio and parallel imaging," *Parallel imaging in clinical MR applications*, pp. 49-61, 2007.
10. P. Lauterbur, "Image formation by induced local interactions: examples employing nuclear magnetic resonance," *Nature*, vol. 242, pp. 190-191, 1973.
11. K. Wikibooks / Maher. (2017). *Basic Physics of Nuclear Medicine/MRI & Nuclear Medicine --- Wikibooks{,} The Free Textbook Project* [Online]. Available: https://en.wikibooks.org/w/index.php?title=Basic_Physics_of_Nuclear_Medicine/MRI_%26_Nuclear_Medicine&oldid=3225239
12. P. T. Callaghan. *Principles of Nuclear Magnetic Resonance Microscopy*. New York: Oxford University Press, Inc., 1993.
13. R. H. Hashemi, W. G. Bradley, and C. J. Lisanti, *MRI: The Basics*, 2nd ed. Philadelphia: Lippincott Williams & Wilkins, 2012.
14. J. T. Bushberg, *The Essential Physics of Medical Imaging*. Philadelphia: Lippincott Williams & Wilkins, 2002.
15. M. A. Bernstein, K. F. King, and X. J. Zhou, *Handbook of MRI Pulse Sequences*. Burlington: Elsevier Academic Press, 2004.

16. Y. Crémillieux, S. Ding, and J. F. Dunn, "High-resolution in vivo measurements of transverse relaxation times in rats at 7 Tesla," *Magnetic Resonance in Medicine*, vol. 39, no. 2, pp. 285-290, 1998.
17. D. N. Guilfoyle, V. V. Dyakin, J. O'Shea, G. S. Pell, and J. A. Helpert, "Quantitative measurements of proton spin-lattice (T_1) and spin-spin (T_2) relaxation times in the mouse brain at 7.0 T," *Magnetic Resonance in Medicine*, vol. 49, no. 3, pp. 576-580, 2003.
18. S. Ljunggren, "A simple graphical representation of Fourier-based imaging methods," *Journal of Magnetic Resonance (1969)*, vol. 54, no. 2, pp. 338-343, 1983.
19. D. B. Twieg, "The k-trajectory formulation of the NMR imaging process with applications in analysis and synthesis of imaging methods," *Medical Physics*, vol. 10, no. 5, pp. 610-621, 1983.
20. R. Bitar, G. Leung, R. Perng, S. Tadros, A. R. Moody, J. Sarrazin, C. McGregor, M. Christakis, S. Symons, A. Nelson, T. P. Roberts, "MR pulse sequences: what every radiologist wants to know but is afraid to ask," *Radiographics*, vol. 26, no. 2, pp. 513-537, 2006.
21. D. B. Plewes and W. Kucharczyk, "Physics of MRI: A Primer," *Journal of Magnetic Resonance Imaging*, vol. 35, no. 5, pp. 1038-1054, 2012.

Chapter 3

Diffusion

Diffusion is the movement of molecules in a system and is dependent on the system and its surrounding environment, such as temperature, size of molecules, and the permeability of molecules through any barriers in the system. The motion of molecules in any fluid, such as water, is random. Because of this randomness, estimating the diffusion of a single molecule is difficult, and therefore we can study a group of molecules instead. In MRI we study the diffusion of molecules within a voxel, which is a 3-dimensional volume of interest. Within this voxel, the diffusion represents the net displacement of that entity of molecules for a given time period.

3.1 Diffusion of water in the body

Water makes up more than 70% of the human body, and takes the form of intra- and extra-cellular fluids [1]. In biological tissues, diffusion of water molecules follows a pattern based on the tissue's structure and properties. In the presence of some pathological conditions such as acute stroke or tumours, diffusion becomes disturbed and the amount of diffusion changes in the affected area. Therefore many abnormalities can be detected by studying these changes in diffusion.

3.2 Diffusion-Weighted imaging

Using MRI, diffusion of water molecules can be exploited to visualize internal physiology using the technique called diffusion-weighted imaging (DWI). Image contrast obtained in DWI reflects the difference in the rate of diffusion between tissues. The basis of DWI's utility is because of this observed diffusive process. Subtle changes in the degree of restriction to diffusion are reflected in the changes in the diffusion-weighted signal. The water molecules that influence the signal in a diffusion weighted image acquisition can be thought of as probes to tissue microstructure. Figure 3.1 shows a T_2 -weighted (a) and diffusion-weighted (b) image from an *ex vivo* mouse as examples.



Figure 3.1: Example MR images of the mouse brain collected *ex vivo*. (a) T_2 -weighted MR image and (b) diffusion-weighted MR image from the same mouse. These images show differences in the contrast between the T_2 -weighted and the diffusion-weighted MR images. For instance, there is more contrast in the diffusion-weighted image than in the T_2 -weighted image with the brain being more hyper-intense compared to the muscles in the diffusion-weighted image than the T_2 -weighted image.

Stejskal and Tanner were the first to quantify diffusion changes, by making the MR signal depend on diffusion [2]. Subsequently, others such as Le Bihan, *et al.* [3], Taylor, *et al.* [4], and Merboldt, *et al.* [5], implemented DWI. Le Bihan, *et al.* implemented DWI on the human brain for the first time in 1986 [6].

3.2.1 Self Diffusion

Molecules in liquid at thermal equilibrium undergo random motions by a phenomenon called Brownian motion. Brownian motion is responsible for molecular diffusion. The molecules travel through space sampling different regions that are available to them, i.e. they undergo self-diffusion. For example, in a glass of water, the molecules are all moving or diffusing with a rate that depends on temperature. The net displacement of the molecules is zero, which is obvious because the water does not move out of the glass. The mean squared displacement $\langle s^2 \rangle$ however is non-zero and it depends on time as described using Einstein's relation:

$$\langle s^2 \rangle = \langle (r_2 - r_1)^2 \rangle = 2n_d D \Delta \quad (3.1)$$

where $s = r_2 - r_1$ is the displacement of a molecule, n_d is the spatial dimension in which the motion is being studied, $\Delta = t_2 - t_1$ is the time over which the diffusion is measured, and the proportionality constant D , is called the self-diffusion coefficient or diffusivity constant. The diffusion coefficient has dimensions of distance squared per unit time (e.g. mm^2/s or $\mu m^2/ms$), is given by the following:

$$D = \frac{k_b T}{6\pi\eta R} \quad (3.2)$$

where k_b is Boltzmann's constant ($k_b = 1.38 \times 10^{-23} J/K$), T is absolute temperature (K), η is viscosity ($Pa \cdot s$) and R is the particle radius (mm or μm). This diffusion coefficient is a measurement of the amount of diffusion migration which depends on the type of medium being measured, and the ease of the diffusion.

3.2.2 Isotropic, anisotropic, unrestricted and restricted diffusion

Molecules diffusing in a uniform medium containing no barriers, or molecules that are studied over a short-time interval during which they do not interact with any barriers are said to experience unrestricted diffusion (Figure 3.2 a). In any uniform media, where there is no preferred direction for diffusion, this type of diffusion is called isotropic.

In other non-uniform media such as porous samples and cellular tissues, there may exist barriers that restrict or hinder molecular displacement. In such media, the behaviour depends on the time scale of the study, as well as the permeability of the barriers. Unrestricted diffusion can still describe the motion if barriers are highly permeable because molecules may still move in a way that appears that the barriers are not there as shown in Figure 3.2b. In media with barriers that are not highly permeable, if the molecules diffusing are studied over a time long enough for them to interact with the barriers, these molecules are said to experience restricted diffusion (Figure 3.2c). In a restricted, non-uniform medium such as porous samples and cellular tissue, if the barriers are not symmetric in all directions, diffusion is anisotropic, which means that the

amount of diffusion is not equal in all directions. The directionality here depends on the cellularity and integrity of the cell within the tissues [7].

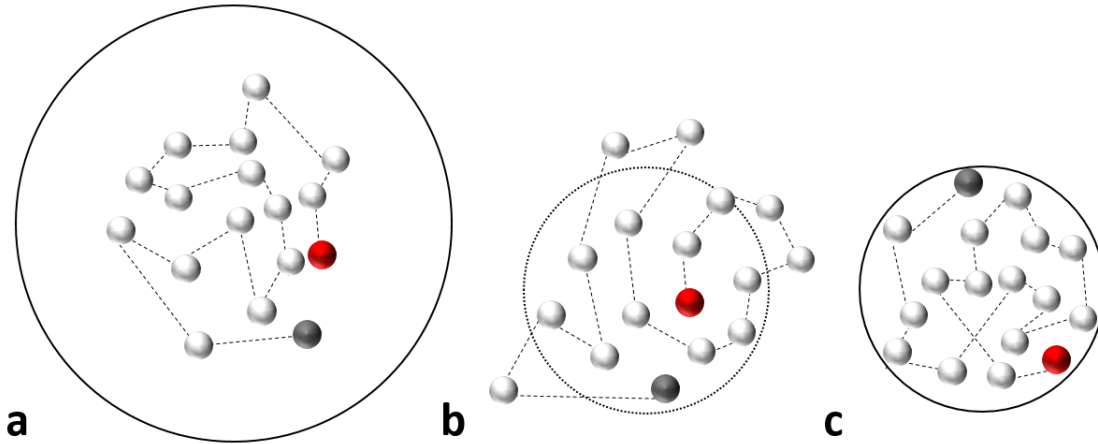


Figure 3.2: Diffusion of a molecule. As a molecule diffuses from one point $r_{initial}$ (red) to another r_{final} (black) it travels approximately the same distance during the same amount of time. This molecule can experience (a) unrestricted diffusion if it does not move a distance that is comparable to the length of a pore, here diffusion is studied at a short period of time where it does not interact with the barriers. (b) Unrestricted diffusion can also occur when the barriers are highly permeable, and the diffusing molecule encounters the barrier of the medium which does not affect its diffusion. (c) Restricted diffusion occurs when a diffusing molecule encounters the barriers of its medium which it cannot easily pass through, and will be found anywhere within the pore.

The free self-diffusion coefficient D_{free} can be measured if there are no restrictions to movement, such as when in a uniform medium. However in non-uniform media, the apparent diffusion coefficient, or ADC is instead measured. Assuming Einstein's relation, the mean squared displacement $\langle s^2 \rangle$, during the diffusion time Δ can be used to find the ADC. Understanding the influence of the restrictions or hindrances on the ADC gives information about the geometry of the boundaries of the surrounding medium, which for MRI, could be tissues, concrete, polymers, gases, etc [7].

As an example, the ADC in a system consisting of molecules in a porous material with diffusion coefficient D , that are restricted to a single pore of diameter a will depend on diffusion time Δ because of Einstein's equation (Equation 3.1). For $\Delta \ll a^2/(2D)$, the diffusion will appear almost unrestricted (Figure 3.3a). For $\Delta \gg a^2/(2D)$, all molecules, regardless of their starting position, will be found anywhere in the pore (Figure 3.3 b) [8].

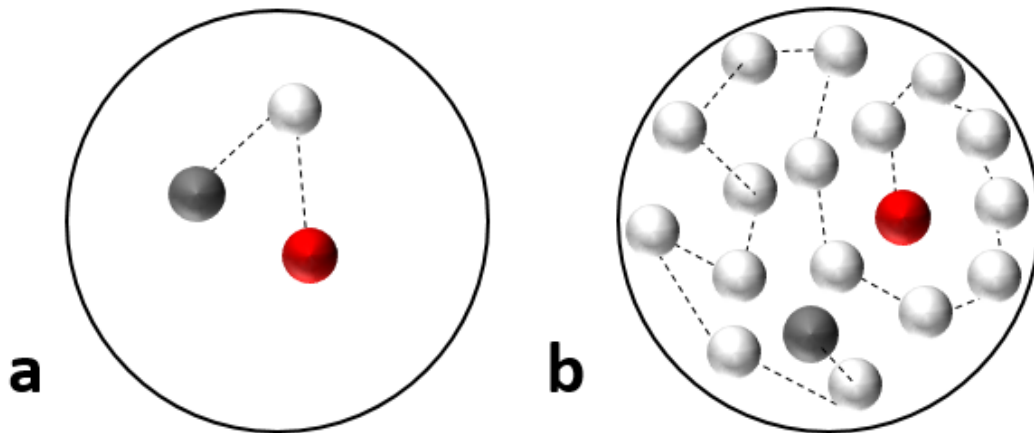


Figure 3.3 (a) When $r^2 \ll a^2$ or $\Delta \ll a^2/(2D)$: Diffusion will appear almost unrestricted, molecules do not move a distance that is comparable to the length of the pore. Diffusion is studied at short times where it doesn't interact with barriers. (b) When $r^2 \gg a^2$ or $\Delta \gg a^2/(2D)$: diffusion is restricted, and the molecules will encounter the barriers in its medium, and will be found anywhere within the pore.

Measurements as a function of diffusion time Δ can provide information about the structure in which the molecules are diffusing. Specifically, there will be a change in the ADC when measuring through the diffusion time $\Delta = a^2/(2D)$ which can be used to determine pore size. More details are described in Sections 3.4 and 3.5.

3.2.3 Bloch-Torrey Equation

In Chapter 2, we saw with the Bloch equation (Equation 2.38) describing its net magnetization that proton motion induces phase shifts in the MR signal. This equation however was solved assuming no diffusive motion. The motion due to molecular diffusion is however different because of its randomness, and within any given image voxel it will contain a very large number of diffusion trajectories which would give different net magnetization if following Equation (2.38).

Torrey in 1965, introduced a diffusion constant D into the Bloch equation, to account for the self-diffusion of molecules at thermal equilibrium [9] and Equation (2.38) can be written as

$$\frac{d\vec{M}(\vec{r}, t)}{dt} = \gamma\vec{M} \times \vec{B} - \frac{M_x\hat{x} + M_y\hat{y}}{T_2} - \frac{(M_z - M_o)\hat{z}}{T_1} + D\nabla^2\vec{M} . \quad (3.3)$$

If we neglect the relaxation and consider only the transverse magnetization, where

$M_{xy}(\vec{r}, t) \equiv M_x(\vec{r}, t) + iM_y(\vec{r}, t)$. Equation (3.3) reduces to [9]:

$$\frac{\partial}{\partial t}\vec{M}(r, t) = \gamma\vec{M}(\vec{r}, t) \times \vec{B} + D\nabla^2\vec{M}(\vec{r}, t) \quad (3.4)$$

If we add a magnetic field gradient, we can define the time-dependent magnetic field along the z- direction as $\vec{B} \equiv \vec{r} \cdot \vec{G}(t)\hat{z}$. After a 90° pulse, the equation for the transverse magnetization becomes [2]:

$$\frac{\partial}{\partial t}M_{xy}(\vec{r}, t) = -i\gamma(\vec{r} \cdot \vec{G})M_{xy}(\vec{r}, t) + D\nabla^2M_{xy}(\vec{r}, t) \quad (3.5)$$

where \vec{G} is independent of position.

For no self-diffusion, $D = 0$, this gives the solution:

$$M_{xy}(\vec{r}, t) = A e^{-i\gamma\vec{r}\cdot\int_0^t \vec{G}(t')dt'} \quad (3.6)$$

with A constant. For $D \neq 0$, assuming that the diffusion is time-dependent but spatially invariant, consider $A \rightarrow A(t)$, where $A(t)$ represents the effect of diffusion on the transverse magnetization. Substituting Equation (3.6) into (3.5), yields a differential equation for $A(t)$

$$\frac{\partial}{\partial t} A(t) = e^{-i\gamma\vec{r}\cdot\int_0^t \vec{G}(t')dt'} D \nabla^2 M_{xy}(\vec{r}, t) \quad (3.7)$$

The equation that represents the signal loss due to diffusion [10] is given by applying the natural logarithm to both sides of Equation (3.7) which gives

$$\frac{\partial}{\partial t} \ln A(t) = D e^{-i\gamma\vec{r}\cdot\int_0^t \vec{G}(t')dt'} \nabla^2 \left[e^{-i\gamma\vec{r}\cdot\int_0^t \vec{G}(t')dt'} \right] \quad (3.8)$$

If we assume $A(0)$ is a constant, i.e. $A(0) = 1$, then solving for $\ln A(t)$:

$$\ln A(t) = -D\gamma^2 \int_0^t dt'' \left[\left(\int_0^{t''} \vec{G}(t')dt' \right) \cdot \left(\int_0^{t''} \vec{G}(t')dt' \right) \right] + \ln A(0) \quad (3.9)$$

or

$$\ln \left(\frac{A(t)}{A(0)} \right) = -D\gamma^2 \left[\int_0^t \left(\int_0^{t'} \vec{G}(t'')dt'' \right) \cdot \left(\int_0^{t'} \vec{G}(t'')dt'' \right) dt' \right] \quad (3.10)$$

Defining the k-space vector, $\vec{k}(t')$ to be

$$\vec{k}(t') = \int_0^{t'} \vec{G}(t'')dt''. \quad (3.11)$$

Then Equation (3.8) becomes

$$\ln\left(\frac{A(t)}{A(0)}\right) = -\left(\int_0^t \vec{k}(t') \cdot \vec{k}(t') dt'\right) D. \quad (3.12)$$

Defining the diffusion-weighting factor, b , further simplifies Equation (3.12) to

$$b(t) = \int_0^t \vec{k}(t') \cdot \vec{k}(t') dt'. \quad (3.13)$$

Equating the time diffusion-weighted signal $S(t)$ to this $A(t)$ and the signal intensity in the absence of any diffusion-weighting, S_0 to A_0 , this gives the diffusion-weighted signal:

$$S(t) = S_0 e^{-b(t)D} \quad (3.14)$$

From this equation, the application of time-dependent gradient magnetic fields, encoded in b , will influence the signal depending on the diffusion constant D of the molecules containing the nuclei being imaged.

The diffusion coefficient, D , is the measurement of the amount of diffusion migration. We still use this equation even when we do not observe this ‘free’ diffusion in samples such as pores or cells. But when we calculate the diffusion coefficient in Equation (3.14) we instead calculate the apparent diffusion coefficient, ADC, due to the restrictions and hindrances to the motion. For simplicity, the equations will have the ADC termed as D .

3.2.4 Pulsed Gradient Spin Echo

In order to generate diffusion-weighting in a MR image, one of the most common pulse sequences used is the pulsed gradient spin echo sequence (PGSE). This PGSE was first described by Stejskal and Tanner in 1965 [2] and a schematic is shown in Figure 3.4. This sequence is similar to the spin echo sequence described in Section 2.71, but it also has two additional gradient pulses of magnitude g , which are applied back-to-back for a duration δ , where the second gradient is applied after the 180° -degree pulse at a time of Δ after the first gradient. These gradients allow for the dephasing and rephrasing of protons' spins so the resulting signal will depend on diffusion. The first gradient pulse introduces the phase shift to the protons' spins which will depend on their positions. The second gradient pulse, which also introduces a phase shift based on the position of the spins, will reverse the changes induced by the first gradient if the spins do not move. If the spins move, the second gradient introduces a phase shift such that the total phase shift depends on displacement. As a result, when there is diffusion present, there will be signal attenuation.

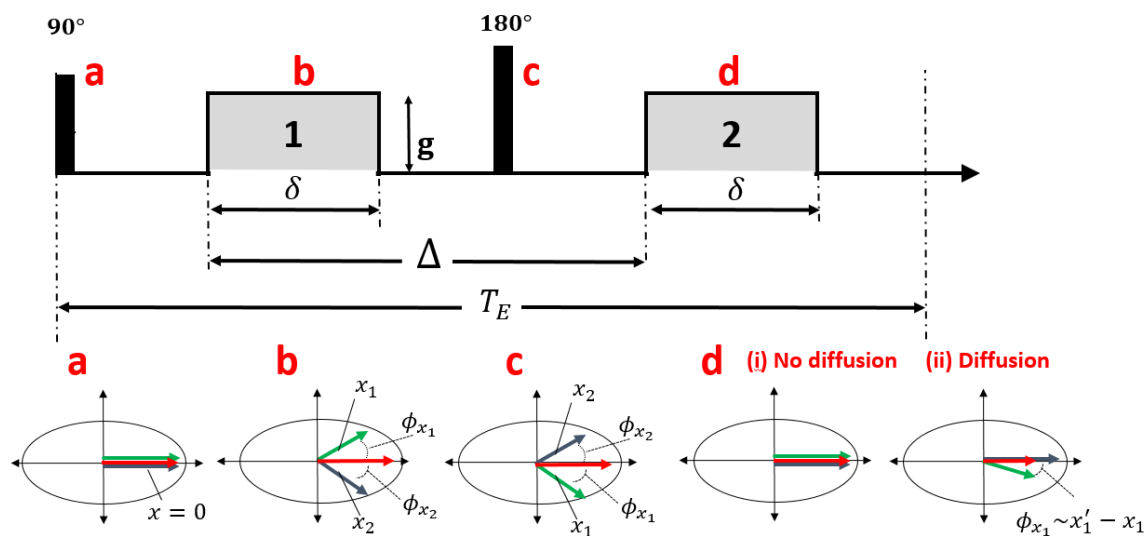


Figure 3.4: Pulsed gradient spin-echo pulse sequence. The spins are represented by the arrows, which are dephased and rephased by the applied gradients (b,d). The second gradient rephrases the spins, which yields an echo, and can result in a net phase of zero in a static system (i), or in a diffusion-weighted spin echo signal (ii). The signal attenuation depends on the amount of diffusive motion that occurs between the two gradients.

Figure 3.4 shows the PGSE pulse sequence. After a 90° -RF pulse which tips the magnetization into the transverse plane, and T_2^* decay begins as in the spin echo sequence which was explained in section 2.71 (Figure 3.4a). The first gradient pulse that is applied produces a magnetic field which causes the spins to experience a phase shift based on the position at the time of the pulse so that the frequency of each nuclei depends on position (Figure 3.4b). If the gradient with amplitude g is in the x -direction, using Equation (2.84), we know that a spin at position x_1 , during the first gradient pulse (1) of duration δ , will acquire a phase of

$$\phi_{x_1} = \gamma g x_1 \delta \quad (3.15)$$

in the rotating frame, as shown in Figure 3.4b.

Thus not all spins in a sample will acquire the same phase during the first gradient pulse. For instance, a spin at position $x_1 > x_2$ will precess faster than a spin at position x_2 resulting in the spin at position x_1 acquiring a larger phase than the spin at position x_2 .

Next, the 180° -RF pulse is applied, reversing the phase of the spins (Figure 3.4c) so that the spin from Equation (3.15) that was at position x_1 during the first pulse will now have a phase of $-\phi_{x_1}$ or :

$$\phi_{x_1} = -\gamma g x_1 \delta \quad (3.16)$$

After a time Δ , the second gradient pulse (2) is applied, which, if the spins have not moved, results in the spins acquiring the same phase they did during the first pulse rephasing the spins. For instance, the spin at position x_1 from Equations (3.15) and (3.16) will acquire the phase from Equation (3.15) again resulting in a total phase at this point of

$$\phi_{x_1} = -\gamma g x_1 \delta + \gamma g x_1 \delta = 0 \quad (3.17)$$

As with the spin echo sequence (section 2.7.1), rephasing from magnetic field inhomogeneities will occur at echo time $t = TE$ (Figure 3.4d). But, the signal obtained will depend on whether diffusion is present. As explained, if no diffusion occurs (Figure 3.4 (d,i)), the phase acquired by the second gradient pulse will be equal and opposite to the phase acquired during the first pulse and then reversed by the 180° pulse, resulting in a net phase of zero (Equation (3.17)).

However, if diffusion occurs, then the mean square phase of all spins will be nonzero, causing a loss of MR signal (Figure 3.4 (d,ii)). For instance if a spin is at position x_1 during the first gradient pulse and x_1' during the second gradient pulse, according to Equations (3.15 - 3.17), the net phase $\Delta\phi$, of the spin at the echo time will be

$$\Delta\phi = \gamma g(x_1' - x_1)\delta \quad (3.18)$$

where $x_1' - x_1$ represents the displacement due to diffusion between the first and second gradient pulses. In summary, for static molecules, $x_1 = x_1'$ and $\Delta\phi = 0$. When diffusion occurs, $x_1 \neq x_1'$ and $\Delta\phi \neq 0$, and the signal is attenuated because the phase shift is different for different spins.

From Figure 3.4, the rectangular pulses and RF pulses can be described by $\vec{G}(t)$,

$$\vec{G}(t) = \begin{cases} -g\hat{x} & \text{for } 0 < t < \delta \\ 0 & \text{for } \delta < t < \Delta \\ +g\hat{x} & \text{for } \Delta < t < \delta + \Delta \\ 0 & \text{otherwise} \end{cases} \quad (3.19)$$

The corresponding k-space vector, $\vec{k}(t)$, from Equation (3.11) becomes

$$\vec{k}(t) = \begin{cases} -gt\hat{x} & \text{for } 0 < t < \delta \\ -g\delta\hat{x} & \text{for } \delta < t < \Delta \\ -g(\delta + \Delta - t)\hat{x} & \text{for } \Delta < t < \Delta + \delta \\ 0 & \text{otherwise} \end{cases} \quad (3.20)$$

and using Equation (3.13) yields a diffusion-weighting factor, $b(TE)$

$$\begin{aligned} b &= \int_0^{TE} \vec{k}(t) \cdot \vec{k}(t) dt \\ &= \gamma^2 \int_0^{\Delta+\delta} k^2 dt \\ &= \gamma^2 g^2 \left(\int_0^{\delta} t^2 dt + \int_{\delta}^{\Delta} \delta^2 dt + \int_{\Delta}^{\Delta+\delta} (\delta + \Delta + t)^2 dt \right) \end{aligned} \quad (3.21)$$

Simplifying gives $b(TE)$:

$$b = \gamma^2 g^2 \delta^2 \left(\Delta - \frac{\delta}{3} \right). \quad (3.22)$$

It should be noted that these gradients require some time to ramp up to their given amplitude, therefore the rectangular shaped gradients are actually trapezoidal.

To describe the trapezoidal gradient pulses which include the ramp rise time, ϵ , the b-value becomes [11]:

$$b = \gamma^2 g^2 \left[\delta^2 \left(\Delta + \frac{\delta}{3} \right) - \frac{\delta \epsilon^2}{6} + \frac{\epsilon^3}{30} \right] \quad (3.23)$$

Obviously, with ϵ small, Equation (3.23) reduces to Equation (3.22) which is often used for simplicity.

This signal for the PGSE sequence is determined by the ADC and the weighting factor, or b-value, is given by Equation (3.22) or (3.23). In general, the b-value is a weighting factor and is determined by the acquisition parameters in the given pulse sequence. For instance, the signal from the PGSE sequence is dependent on the time between pulses Δ , the strength of the gradients g , and the duration of the gradients applied δ . The gyromagnetic ratio γ , is a constant, and for the hydrogen proton is given as $\gamma = 42.58$ MHz/T. Adjusting the b-value allows for the different weightings in the image, and the diffusion coefficient D (or ADC) can be determined.

The larger the b-values, the larger the effect of diffusion so that it is more pronounced in the images. The tissues with high diffusion are seen as hypo-intense regions in the image while tissues with restricted diffusion are seen as hyper-intense. Signal intensity decreases as gradient

strength increases, and the extent of the signal decay depends on the diffusion constants of the water in the brain. The signal from the cerebrospinal fluid (CSF) region decays faster due to a higher ADC for CSF relative to the rest of the brain matter, which in turn appears much darker in the image than the rest of the brain matter.

The longer the diffusion time, the more time for water molecules to diffuse, and the refocussing of the protons is less perfect. Alternatively, the higher the diffusion constant, the larger the signal loss. Signal loss is also larger when the gradient pulse amplitudes are stronger or longer.

To obtain various amounts of diffusion weighting, we can change the strength of the gradients or we can change the diffusion time. This enables us to generate image contrast by exploiting the diffusion property of the protons found in the water in tissues. Care must be taken however, as to not change the TE and TR , so that the T_1 , T_2 , and T_2^* contrast does not also change.

3.3 Apparent diffusion coefficient, diffusion anisotropy, and the diffusion tensor.

Many measures are used to describe the diffusion information calculated from MRI. This section describes these measures and their meanings.

3.3.1 Apparent diffusion coefficient

To determine the diffusion coefficient, multiple images can be obtained using the PGSE pulse sequence while varying the gradient pulse strengths. For example, suppose two experiments were performed at two different b-values, b_1 and b_2 , where we obtain two diffusion-weighted signals, S_1 and S_2 . Manipulating Equation (3.14), we can calculate the diffusion coefficient:

$$\ln S_2 = -(b_2 - b_1)D + \ln S_1 \quad (3.24)$$

and

$$D = \frac{|\ln S_1 - \ln S_2|}{b_2 - b_1} \quad (3.25)$$

3.3.2 Mean diffusivity

Equation 3.25 can be extended to calculate the apparent mean diffusivity in a voxel, when applying gradients in 3 orthogonal directions (x, y and z). Calculating D along the three directions (D_x, D_y, D_z), allows the mean apparent diffusivity, which describes the magnitude of the apparent diffusivity with no information about its directionality, to be calculated as

$$\langle D \rangle = \frac{D_x + D_y + D_z}{3}. \quad (3.26)$$

3.3.3 Diffusion tensor

In order to quantify or describe both the magnitude and directionality of diffusion, we need to obtain diffusion-weighted images in 6 or more gradient directions, which can be constructed into a 3-dimensional representation of diffusion in a voxel, called the apparent diffusion tensor. The magnitudes of the tensor components depend on the orientation relative to the scanner frame of reference, defined by the gradients applied in the pulse sequence

$$\vec{D} = \begin{pmatrix} D_{xx} & D_{xy} & D_{xz} \\ D_{yx} & D_{yy} & D_{yz} \\ D_{zx} & D_{zy} & D_{zz} \end{pmatrix}. \quad (3.27)$$

Each voxel in the acquired image has a representative diffusion tensor. The information about the directionality, and the anisotropy of the apparent diffusivity in the voxel element can be extracted using tensor diagonalization. Diagonalization of \vec{D} yields the eigenvalues $(\lambda_1, \lambda_2, \lambda_3)$ and the corresponding eigenvectors $(\epsilon_1, \epsilon_2, \epsilon_3)$ which describe the magnitude and direction of diffusion, respectively. The eigenvalues are defined such that λ_1 has the largest value. The diagonalized \vec{D} is then given as

$$\vec{D} = \begin{pmatrix} \lambda_1 & 0 & 0 \\ 0 & \lambda_2 & 0 \\ 0 & 0 & \lambda_3 \end{pmatrix}. \quad (3.28)$$

The diffusion tensor can be represented as an ellipsoid (Figure 3.5) [12]. The magnitude of the major axis is proportional to λ_1 with the minor axes proportional to λ_2 and λ_3 . Directionality of the ellipsoid is determined by the corresponding eigenvectors. For $\lambda_1 \approx \lambda_2 \approx \lambda_3$, the ellipsoid is

spherical and diffusion is isotropic. For $\lambda_1 \approx \lambda_2 \gg \lambda_3$, the ellipsoid is oblate and diffusion is planar isotropic. For $\lambda_1 \gg \lambda_2 \approx \lambda_3$, the ellipsoid is prolate and diffusion is linear anisotropic.

Ellipsoid Representation of D

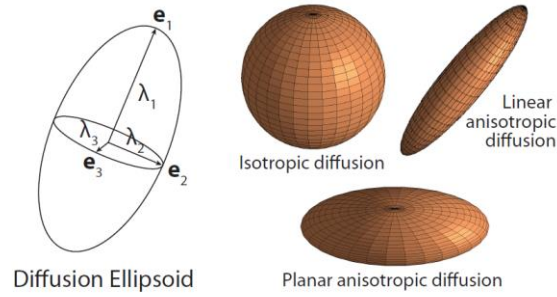


Figure 3.5: Diffusion Ellipsoid (left). Ellipsoid representations of linear anisotropy, planar anisotropy, and spherical anisotropy (right)[12].

Scalar metrics can be derived such as the mean diffusivity, axial ($\lambda_{||}$) and radial (λ_{\perp}) diffusivity, and fractional anisotropy (FA).

Mean diffusivity ($\langle D \rangle$), defines the magnitude of the diffusion in a voxel (Equation (3.29)).

Axial diffusivity, $\lambda_{||}$ indicates the amount of diffusion running parallel to the major axis of the ellipsoid (Equation (3.30)), λ_1 . Radial diffusivity, λ_{\perp} indicates the amount of diffusion running perpendicular to the major axis of the ellipsoid (λ_2 and λ_3) (Equation (3.31)).

$$\langle D \rangle = \frac{\text{Trace}(\vec{D})}{3} = \frac{\lambda_1 + \lambda_2 + \lambda_3}{3} \quad (3.29)$$

$$\lambda_{\parallel} = \lambda_1 \quad (3.30)$$

$$\lambda_{\perp} = \frac{\lambda_2 + \lambda_3}{3} \quad (3.31)$$

3.3.4 Fractional Anisotropy

Fractional anisotropy is based on the standard deviation of the eigenvalues and characterizes the anisotropy of the ellipsoid. Ranging from 0 to 1, higher numbers indicate more anisotropy, with maximum anisotropy at $FA = 1$.

$$FA(\vec{D}) = \sqrt{\frac{3}{2}} \times \frac{\sqrt{(\lambda_1 - \langle D \rangle)^2 + (\lambda_2 - \langle D \rangle)^2 + (\lambda_3 - \langle D \rangle)^2}}{\sqrt{\lambda_1^2 + \lambda_2^2 + \lambda_3^2}} \quad (3.32)$$

FA is sensitive to low values of anisotropy and has become the most widely reported measure of anisotropy [13]. FA does not however distinguish the shape of the diffusion ellipsoid but provides useful information nonetheless. In healthy white matter with ordered and myelinated axon bundles, FA is high due to the directional structure of the axons. FA is low in grey matter where directionality is limited.

Changes in $\langle D \rangle$, axial diffusivity (λ_{\parallel}), and radial diffusivity (λ_{\perp}), can consequently cause changes in FA which makes its sensitivity a very useful tool in studying the changes in pathology [14].

3.4 Temporal Diffusion Spectroscopy

Section 3.2.2 discussed how the measured ADC of water diffusing inside a pore of a given radius depends on the time over which the diffusion is measured, termed the diffusion time. Others have derived expressions for the ADC as a function of time in various geometries [15- 18]. The goal of this thesis was to develop a method to infer micron-sized structures in samples. The ultimate goal of this project was to infer axon diameter sizes in brain tissue. Thus this section discusses two models of diffusion in cylinders, which can represent a simplified version of axons that are used in the experiments in Chapter 6. Two models for water diffusing outside the cells or axons in Chapters 4 and 5 are discussed here.

Several methods for estimating axon diameter distributions and the density of axons in fibre tracts using MRI measure ADC as a function of diffusion time Δ , using PGSE [19, 20, 21]. The AxCaliber method uses a framework that combines composite hindered and restricted models of water diffusion (CHARMED) and PGSE measurements [19]. The method uses one fixed gradient direction and multiple diffusion times and gradient strengths to make the CHARMED model more sensitive to axon diameter [19]. The MR signal is fitted to a simplified theoretical model with components from restricted diffusion ($\Delta \gg r^2/(2D)$), hindered diffusion [19], and free diffusion ($\Delta \ll r^2/(2D)$) [22]. Water in each axon of size or radius, r_i , in the model will experience that transition from restricted to free diffusion at different diffusion time. For example, water in an axon with a small diameter will experience restriction for much smaller diffusion time than water in a larger axon [7]. Thus by shortening the diffusion time Δ , smaller and smaller axons move from the restricted component to the free component allowing the inference of axon diameter of smaller and smaller axons.

The ActiveAx method further extended and optimized these methods to determine the accuracy and precision with which this important new biomarker, axon diameter, can be estimated in live human subjects [20]. The work from this group combined a simplified version of CHARMED with high-angular-resolution diffusion imaging (HARDI) and a model with a single axon diameter [20]. It has been modified to be robust in the presence of orientation dispersion but is insensitive to axons $< 2.5 \mu\text{m}$ in diameter, making it irrelevant for rodent studies [23] and the axons that constitute the majority of cortical connections.

The AxCaliber [19] and ActiveAx [20] models assume axons are parallel non-permeable cylinders. Water outside the cylinders, termed extra-axonal (or extracellular) water, is modelled as being constant with time. Water inside the cylinders, termed intra-axonal (or intracellular) water, is assumed to undergo restricted diffusion. The diffusion gradient is applied perpendicular to the cylinders to measure the radial diffusion. Images are collected varying the diffusion time and gradient strengths to obtain the signal used in the fits. This model was used in Chapter 6.

3.4.1 AxCaliber Model

The AxCaliber model assumes there are cylinders of different radii, r_i . The formula for the MR signal in the AxCaliber model adds together the signal from cylinders of all radii which are assumed to follow a gamma distribution. Fitting the MR signal data to the formula allows the inference of the parameters of the gamma distribution, the axon packing fraction, and the extra-axonal water diffusion coefficient.

In these experiments, in order to incorporate OGSE instead of PGSE into AxCaliber, a modification to the model was used [24]. If the intra-axonal region contributes a signal E_r , and the extra-axonal region contributes a signal E_h , then the total normalized signal is the volume-weighted sum of the contributions from each region.

$$E = f_{axon}E_r + (1 - f_{axon})E_h \quad (3.33)$$

where f_{axon} is the relaxed-weighted volume fraction of axons, or the intra-axonal volume fraction. Diffusion in the extra-axonal space is assumed to be hindered and is modelled with a Gaussian distribution

$$E_h = e^{-bD_h} \quad (3.34)$$

where D_h is the hindered diffusion coefficient of the extra-axonal space, and the b-value depends on the pulse sequence. The pulse sequences that were used in this experiment is the sine-OGSE and the apodised cosine-OGSE sequence, and will be discussed in Section 3.5.3.

The restricted signal from a large collection of axons is a volume-weighted sum of all cylinders' signals. It is assumed that the axon diameters come from a distribution of $w(r, \theta)$, parameterized by θ . Based on previous studies assumed that the axon diameters follow a gamma distribution [19, 24, 25], with the signal arising from the collection is

$$E_r = \frac{\sum_i w(r_i, \theta) r_i^2 e^{\beta(2\tau)} r_i^2}{\sum_j w(r_j, \theta) r_j^2} \quad (3.35)$$

where $\exp[\beta(2\tau)]$ is the signal from a cylinder of radius r_i , at the echo time of 2τ [19]. The gamma distribution has two free parameters α and β , and is given by

$$w(r, \alpha, \beta) = \frac{r^{\alpha-1} e^{-r/\beta}}{\beta^\alpha \Gamma(\alpha)} \quad (3.36)$$

3.4.2 ActiveAx Method

The ActiveAx model simplifies the number of parameters because it infers an effective mean axon diameter, AxD, rather than the full distribution of diameters. Basically, this model assumes all cylinders have the same diameter and infers this diameter, termed the effective mean diameter. This allows fewer measurements to be made, or more time repeating measurements which can be averaged to obtain more accurate results. Fitting the MR signal data to the formula allows the inference of the intra-axonal and extra-axonal diffusion coefficients, the axonal packing fraction and the mean effective axon diameter. This AxD correlates with the quantity:

$$\text{mean AxD} = \frac{\sum_{n=1}^N d_n^3}{\sum_{n=1}^N d_n^2} \quad (3.37)$$

where N is the total number of axons in each volume of interest, and d_n is the effective mean diameter of the n th axon.

Before testing the full AxCaliber model, phantoms were studied with known sizes to ensure that models which used PGSE could be switched to using the oscillating gradient spin echo (OGSE) sequence and correctly infer sizes in the samples. Chapter 4 discusses measurements made from water diffusing between polystyrene beads and capillary tubing. Chapter 5 goes into more detail

of the models used to make the inferences, and used more optimized imaging parameters found from the previous experiments. Briefly, the bead experiments used a model which assumed the pores are a system of interconnected spheres [26, 27]. The diffusion times or gradient frequencies used are appropriate for the size of the pores in the samples used in that study [27]. Tubes with micron-sized outer diameters could not be found so the gradient frequencies used for the tube experiments and corresponded to water diffusing in the short-time regime. The Mitra model [28] describes diffusion at short times and was used to study the water diffusing between the tubes and to find the surface-to-volume ratio (S/V) of the tubes. In this model, the diffusion coefficient is proportional to the square root of time and depends on the surface-to-volume ratio of restrictions in a sample [28-30]. The relationship between the time dependence of the diffusion coefficient, assumed to be measured with narrow gradient pulses, and S/V allows for the possibility of extracting information about restrictions in porous media [28-30].

3.5 Oscillating Gradient Spin Echo (OGSE)

This section explains the pulse sequences used in the experiments in this thesis and the reason for the need to switch pulse sequences from the PGSE sequence. The first section explains the limitations of the PGSE sequence. The remaining sections explain the oscillating gradient spin echo (OGSE) sequences and the reason they were able to overcome the limitations with the PGSE sequence.

3.5.1 Short Diffusion Times in the Pulsed Gradient Spin Echo Sequence

MR measurements of the size of the structures which cause the changes in ADC have been studied extensively to measure large axon diameter distributions $> 5 \mu\text{m}$ [23] and the density of axons in fibre tracts. The majority of axons constituting cortical connections have smaller axon diameter distributions $< 5 \mu\text{m}$ [31], thus a means to use shorter times to probe diffusion is necessary. The ultimate goal of this project is to measure smaller axon diameter distributions which are more relevant to neuroscience.

Measuring smaller axon diameter sizes requires shorter diffusion times so that the transition from restricted to hindered water diffusion within the axons can be detected. The PGSE sequence requires that diffusion times be large enough with respect to most axon diameters in human and rodent tissue which limits the information that could be obtained from the measurements.

Examining Equation (3.22), it can be seen that in order to keep b constant when shortening the diffusion time in the PGSE sequence, this requires strong gradients in order to measure smaller axon diameters. Gradient coils are limited in the power they can supply. Moreover, for small duration, large amplitude gradient pulses, there will be a large change in magnetic field experienced by the subject in a short amount of time. This induces an electric field in the subject, which could cause twitching of the skin, pain, or interference with the function of the heart or brain [32]. These large gradient pulses which rapidly turn on and off also cause eddy currents which can cause artefacts in images. Therefore time delays are typically added after large gradient pulses to allow the eddy currents to settle. These time delays also limit how short diffusion times can be. The 180° pulse occurs during the diffusion time and this RF pulse

requires a finite time. Therefore the diffusion time is also limited by the RF pulse. Thus to have detectable signal decay for small diffusion times, many images would be required to be collected and averaged together and this would take a lot of time for the subject to be in the MRI machine. For live subjects, long imaging times can be uncomfortable and for those needing anesthesia, long imaging times can be hazardous. For hospitals with long wait times, long imaging times would further increase these wait times.

Therefore, PGSE methods can only measure distributions $> 2.5 \mu\text{m}$ [33], which is irrelevant for rodent studies. Measuring smaller axon diameters will provide new important information for neuroscience because axon diameter is directly related to nerve conduction velocity and can thus provide more information to understand diseases. Hence a new pulse sequence is needed for measuring smaller structures.

3.5.2 Oscillating Gradient Spin Echo (OGSE) Sequences.

The original OGSE sequence was proposed to make measurements at short diffusion times [34]. In this sequence, the trapezoidal gradient pulses, typically idealized as rectangular pulses (Figure 3.6a) in pulse sequence diagrams of the PGSE sequence are replaced with sinusoidally varying gradient pulses (Figure 3.6b). Each period of the sine wave acts as a diffusion weighting so that the magnetic moments are dephased by the first lobe of the sine wave and rephased by the second lobe. Increasing the frequency f of the gradient oscillations gives access to shorter diffusion times ($\Delta \sim 1/f$). These sine waves are repeated multiple times so that sufficient diffusion weighting can be obtained, even at short diffusion times.

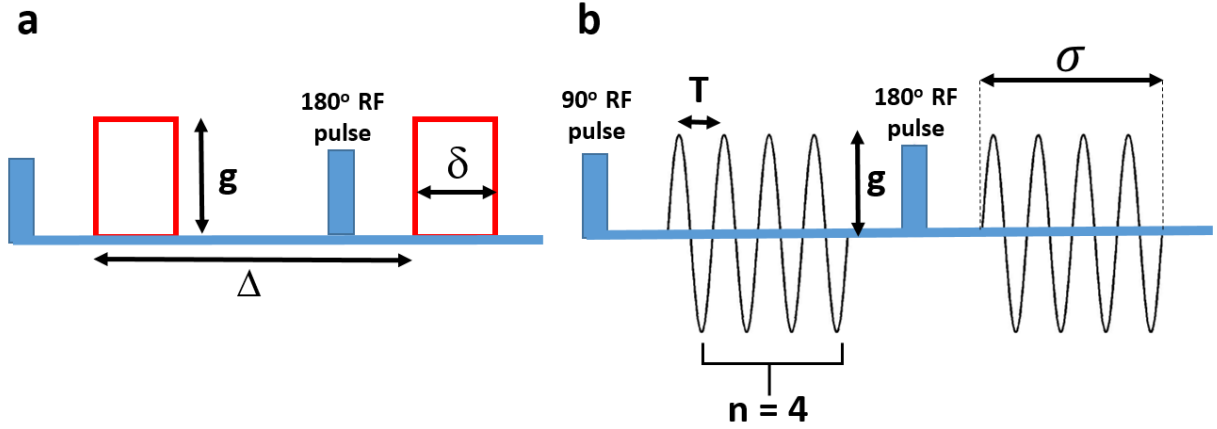


Figure 3.6: PGSE vs OGSE. (a) PGSE involves two rectangular gradients (idealized) of constant strength g , applied back-to-back for a duration δ , with the second gradient applied at a time Δ , after the first gradient pulse. Actual PGSE pulse sequences use trapezoidal gradients because of time needed to ramp up the gradient amplitude. (b) OGSE replaces the rectangular gradients of PGSE with sinusoidally varying gradient pulses. The duration of each gradient σ , is chosen to be an intergral number of n , of cycles of oscillations. Each period T , of the sine wave acts as a diffusion weighting so that the spins are dephased in the first lobe, and rephased in the second lobe, similar to the rectangular gradients of the PGSE. This figure shows the OGSE sequence for $n = 4$.

The gradient values for the sine-modulated OGSE sequence are

$$\vec{G}(t) = \begin{cases} -g \sin(\omega_n t) & \text{for } 0 \leq t < \sigma \\ 0 & \text{for } \sigma < t < \Delta \\ g \sin(\omega_n (t - \Delta)) & \text{for } \Delta \leq t \leq \Delta + \sigma \end{cases} \quad (3.38)$$

where T is the period, σ is the duration of each gradient, g is the gradient strength, $\omega_n = \frac{2\pi n}{T}$,

$\sigma = nT$, and $n =$ number of periods of the sine wave.

Using Equation (3.11) the k value is

$$\vec{k}(t) = \begin{cases} \frac{g}{\omega_n} [\cos(\omega_n t) - 1] & \text{for } 0 \leq t < \sigma \\ 0 & \text{for } \sigma < t < \Delta \\ \frac{g}{\omega_n} [1 - \cos(\omega_n (t - \Delta))] & \text{for } \Delta \leq t \leq \Delta + \sigma \end{cases} \quad (3.39)$$

Following the same process used to derive the b-value for the PGSE sequence (Equation (3.22)), the b-value for the OGSE sequence is derived as

$$\begin{aligned}
b &= \int_0^{TE} \vec{k}(t) \cdot \vec{k}(t) dt = \gamma^2 \int_0^{\Delta+\sigma} k^2 dt \\
&= \gamma^2 \left\{ \int_0^{\sigma} \left(\frac{g}{\omega_n} [\cos \omega_n t - 1] \right)^2 dt \right. \\
&\quad \left. + \int_{\Delta}^{\Delta+\sigma} \left(\frac{g}{\omega_n} [1 - \cos(\omega_n(t - \Delta))] \right)^2 dt \right\}
\end{aligned} \tag{3.40}$$

The first integral of Equation (3.40) represents one of the 2 diffusion-weighting waveforms, which equals to $b_1 = \frac{3}{8} \left(\frac{\gamma g}{\pi n} \right)^2 \sigma^3$. Similarly, the second integral is equal to the first. Thus using Equation (3.13) the b-value for the OGSE sequence for the sine modulated waveform (Figure 3.7a) is:

$$b_{sin} = \frac{3}{4} \left(\frac{\gamma g}{\pi} \right)^2 n T^3 . \tag{3.41}$$

This equation shows that there is now another option beyond increasing the gradient strength for increasing the diffusion weighting, namely, increasing the number of sinusoidal lobes, n .

3.5.3 Temporal Diffusion Spectroscopy with OGSE

OGSE has been used to measure the ADC as a function of diffusion time Δ , but measurements of the diameter of the structures which cause the changes in ADC had only been done with PGSE sequences [19,20, 35-38]. Using OGSE, surface-to-volume ratios from packed beads in water [39] and in cells of vegetables [38] have been measured. Given that diffusion during each wave

of the sinusoidal pulse is not independent of the other sinusoidal pulse, the ADC cannot easily be measured as a function of time using the OGSE sequence. Thus this sequence has been adapted for easier extraction of information about the variation of ADC with the frequency, ($f \sim 1/\Delta$), of the oscillating gradient wave and for easier implementation [40]. The most direct link between frequency and time is with the cosine-OGSE sequence (Figure 3.7b). This cosine-OGSE sequence has a b-value of

$$b_{cos} = \frac{1}{4} \left(\frac{\gamma g}{\pi} \right)^2 n T^3 . \quad (3.42)$$

It is not physically possible to implement this cosine sequence because gradient amplitudes cannot rise instantaneously. Therefore the apodised cosine sequence (Figure 3.7c) was proposed to overcome this problem while still approximately preserving the simple form of the frequency spectrum. A sine wave pulse with twice the frequency of the cosine pulse is added to the beginning and end of the cosine pulse for one quarter of the period. The b-value for this sequence is

$$b_{acos} = \frac{1}{4} \left(\frac{\gamma g}{\pi} \right)^2 n T^3 \left(1 - \frac{1}{8n} \right) . \quad (3.43)$$

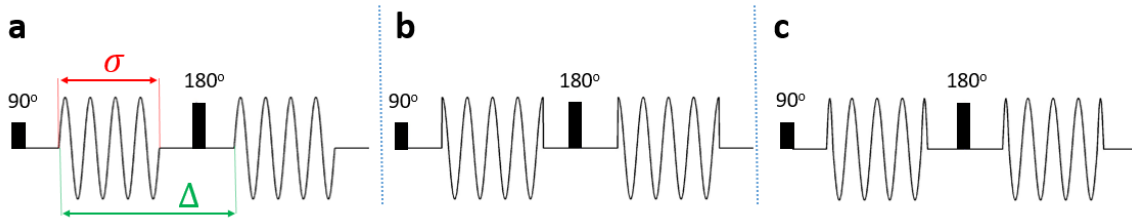


Figure 3.7: Pulse sequence diagrams for (a) sine wave, (b) ideal cosine wave, and (c) apodised cosine wave.

These new sequences have been used to study the ADC as a function of frequency and it was found that the contrast between tissues might be greater at a discrete, moderately high frequency (or a shorter diffusion time) than at low frequencies, as suggested by theoretical consideration of simple geometries and preliminary studies in tumours [15] and rat brain [41].

Given that the ultimate goal of this project is to measure axon diameters, it seemed obvious to switch the pulse sequence used with AxCaliber and ActiveAx to an OGSE sequence in order to probe smaller diameters. Others have postured that switching pulse sequences could be beneficial [20]. Alexander *et. al.* studied generalized waveforms (GEN) attempting to find an ideal pulse sequence. They were able to make axons with smaller radii more distinguishable with GEN than with PGSE [29, 43]. They suggest that oscillating waveforms would provide valuable information for *in vivo* studies [43].

In the phantom experiments described in Chapters 4 and 5, the apodised cosine sequence was used, whereas in the brain experiment in Chapter 6 the sine sequence was used.

3.5.4 Connected Spherical Pore Extra-Cellular Model

The diffusion spectrum, $D(\omega)$, for the extra-cellular water in the connected spherical pore model is given by [43, 44]

$$D(\omega) = D_h + \sum_k B_k \frac{a_k(D_0 - D_h)\omega^2}{a_k^2(D_0 - D_h)^2 + \omega^2} \quad (3.44)$$

where D_0 is the free diffusion coefficient, the first term (D_h) is the long-time diffusion coefficient and the second term is a sum of terms, including a_k and B_k , dependent on the pore geometry, which is assumed to be spherical [43]. Both a_k and B_k depend on the pore radius, r_{pore} [45]. For spherical pores,

$$a_k = \left(\mu_k/r_{pore}\right)^2 \quad (3.45)$$

and

$$B_k = \frac{2\left(r_{pore}/\mu_k\right)^2}{\mu_k^2 - 2} \quad (3.46)$$

where μ_k is the k^{th} root of $\mu J'_{3/2}(\mu) - J_{3/2}(\mu) = 0$ and $J_{3/2}$ is a Bessel function of the first kind [17]. Overall, there are three model parameters: D_o , D_h , and r_{pore} .

This model was used for the bead phantoms in Chapters 4 and 5. Normalized signal data collected from the extra-cellular water in these samples was expected to depend on the b-value and diffusion coefficient according to

$$S/S_0 = \exp(-b_{acos}(\omega, g)D(\omega)) \quad (3.47)$$

where b_{acos} is the b-value for an apodised cosine sequence (see Equation (3.39)) [43]. D_o was held fixed to the ADC value obtained for water, and both D_h and the pore radius were extracted from the fit. The natural logarithm of Equation (3.47) was used such that the data could be fitted to the linear equation

$$\ln(S/S_0) = -b_{acos} \cdot D \quad (3.48)$$

The beads were assumed to be tightly packed in a cubic lattice. In a tightly packed cubic lattice of spheres, there are two types of interstitial holes (or pores), the octahedral hole with radius

0.414 times the radius of the spheres, and the tetrahedral hole with radius 0.225 times the radius of the spheres [26] (Figure 3.8). Using these two types of interstitial holes, pore size can be related to bead size or bead diameter d_{bead} by

$$d_{bead} = \frac{2 \cdot r_{pore}}{0.414} \quad (3.49)$$

$$d_{bead} = \frac{2 \cdot r_{pore}}{0.225} \quad (3.50)$$

where Equations (3.49) and (3.50) refer to octahedral and tetrahedral holes, respectively.

The ratio of the number of each type of hole to sphere changes depending on whether the spheres are packed as cubic close packed (CCP) or hexagonal close packed (HCP) but the ratio of the sizes of the pores to the sizes of the spheres does not change [27] (Figure 3.9).

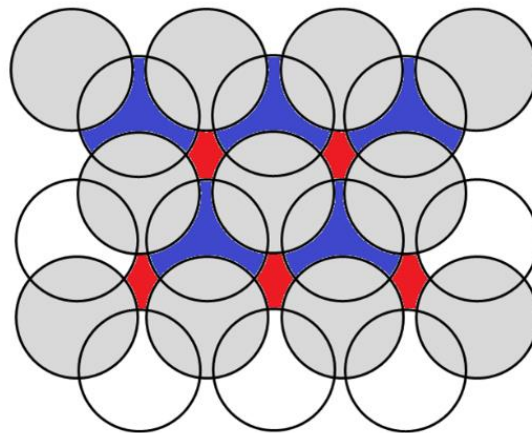


Figure 3.8: Tetrahedral and Octahedral holes. Given two layers of spheres; 1st layer (grey), and 2nd layer (white). When the second layer of spheres are placed on top of the first layer, the holes that are created between the first layer of grey spheres are called tetrahedral holes (shown in blue). The holes in the second layer that falls directly over the holes in the first layer are called octahedral holes (shown in red) (modified from [46]).

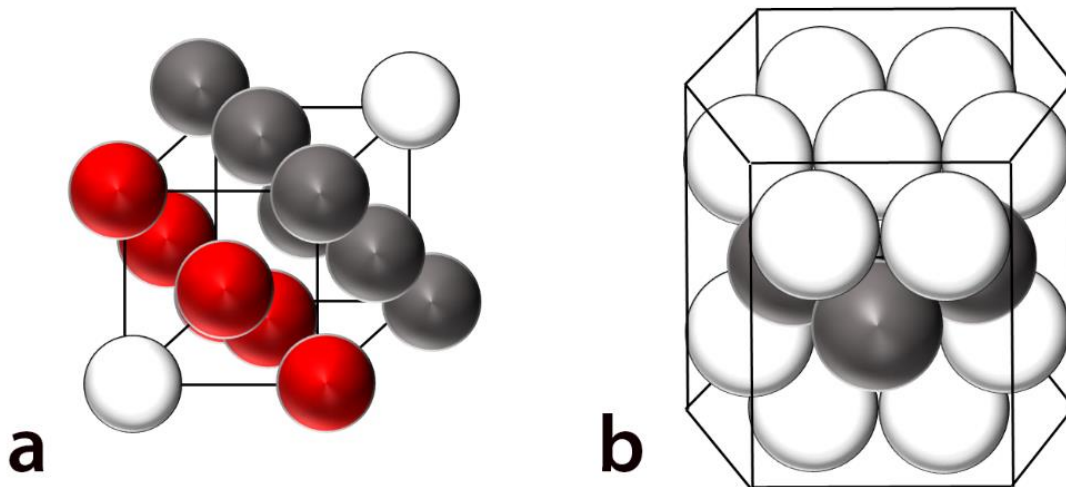


Figure 3.9: To relate the pore-size to bead size, the ratio of the number of each type of hole (tetrahedral or octahedral) to the number of spheres depends on how the spheres are packed, which can be either (a) cubic close packed (CCP) or (b) hexagonal close packed (HCP) (modified from [47]).

3.5.5 Short-time or High Frequency Model

The diffusion spectrum at short diffusion times or high frequencies ($\Delta \sim 1/\omega$) is approximated by

$$D(\omega) = D_0(1 - c(n)c_d S/V \sqrt{D_0/\omega}) \quad (3.51)$$

where D_0 is the intrinsic diffusion coefficient, S/V is the surface to volume ratio of the sample and c_d and $c(n)$ are numerical factors. For these numerical factors, c_d depends on the geometrical dimensions and $c(n)$ depends on the pulse sequence [28, 48]. Overall, there are two free model parameters: D_0 and S/V .

Signal data were fitted directly with Equation (3.51). Both D_0 and the surface-to-volume ratio were extracted from the fit. Assuming that the tubes were tightly packed, in a tightly packed

hexagonal lattice or square packed lattice of cylinders, the surface-to-volume ratio is related to the cylinder diameter d through the relation,

$$d = \frac{4f}{((1 - f) S/V)} \quad (3.52)$$

where f is the packing fraction of the tubes. This relation was used to relate the surface-to-volume ratio to the tube diameter. To determine the packing fraction of our sample, the number of capillary tubing pieces that could fit inside a sample tube was counted. The packing fraction that was used was the ratio of the area of the capillary tubing to the area of the sample tube.

References

1. P. E. Watson, I. D. Watson, and R. D. Batt, "Total body water volumes for adult males and females estimated from simple anthropometric measurements," *The American Journal of Clinical Nutrition*, vol. 33, no. 1, pp. 27-39, 1980.
2. E. O. Stejskal and J. E. Tanner, "Spin diffusion measurements: spin echoes in the presence of a time-dependent field gradient," *The Journal of Chemical Physics*, vol. 42, no. 1, pp. 288-292, 1965.
3. D. Le Bihan and E. Breton, "Imagerie de diffusion in-vivo par résonance magnétique nucléaire," *Comptes-Rendus de l'Académie des Sciences*, vol. 93, no. 5, pp. 27-34, 1985.
4. D. Taylor and M. Bushell, "The spatial mapping of translational diffusion coefficients by the NMR imaging technique," *Physics in Medicine & Biology*, vol. 30, no. 4, p. 345, 1985.
5. K.-D. Merboldt, W. Hanicke, and J. Frahm, "Self-diffusion NMR imaging using stimulated echoes," *Journal of Magnetic Resonance (1969)*, vol. 64, no. 3, pp. 479-486, 1985.
6. D. Le Bihan, E. Breton, D. Lallemand, P. Grenier, E. Cabanis, and M. Laval-Jeantet, "MR imaging of intravoxel incoherent motions: application to diffusion and perfusion in neurologic disorders," *Radiology*, vol. 161, no. 2, pp. 401-407, 1986.
7. D. K. Jones, *Diffusion MRI*. New York: Oxford University Press, 2010.
8. W. S. Price, "Pulsed-field gradient nuclear magnetic resonance as a tool for studying translational diffusion: Part 1. Basic theory," *Concepts in Magnetic Resonance Part A*, vol. 9, no. 5, pp. 299-336, 1997.
9. H. C. Torrey, "Bloch equations with diffusion terms," *Physical Review*, vol. 104, no. 3, p. 563, 1956.
10. R. W. Brown, E. M. Haacke, Y.-C. N. Cheng, M. R. Thompson, and R. Venkatesan, *Magnetic Resonance Imaging: Physical Principles and Sequence Design*. New York: John Wiley & Sons, 2014.
11. P. J. Basser, J. Mattiello, and D. LeBihan, "Estimation of the effective self-diffusion tensor from the NMR spin echo," *Journal of Magnetic Resonance, Series B*, vol. 103, no. 3, pp. 247-254, 1994.
12. J. D. Thiessen, "Development and application of quantitative MRI methods for assessing white matter integrity in the mouse brain," Ph.D. dissertation, Dept. of Physics & Astronomy. University of Manitoba, Winnipeg, MB, 2012.
13. S. Mori, *Introduction to Diffusion Tensor Imaging*. Oxford: Elsevier, 2007.
14. A. L. Alexander, J. E. Lee, M. Lazar, and A. S. Field, "Diffusion tensor imaging of the brain," *Neurotherapeutics*, vol. 4, no. 3, pp. 316-329, 2007.

15. J. C. Gore, J. Xu, D. C. Colvin, T. E. Yankeelov, E. C. Parsons, and M. D. Does, "Characterization of tissue structure at varying length scales using temporal diffusion spectroscopy," *NMR in Biomedicine*, vol. 23, no. 7, pp. 745-756, 2010.
16. J. Xu, M. D. Does, and J. C. Gore, "Dependence of temporal diffusion spectra on microstructural properties of biological tissues," *Magnetic Resonance Imaging*, vol. 29, no. 3, pp. 380-390, 2011.
17. J. Xu, M. D. Does, and J. C. Gore, "Quantitative characterization of tissue microstructure with temporal diffusion spectroscopy," *Journal of Magnetic Resonance*, vol. 200, no. 2, pp. 189-197, Oct 2009.
18. B. Balinov, B. Jonsson, P. Linse, and O. Soderman, "The NMR self-diffusion method applied to restricted diffusion. Simulation of echo attenuation from molecules in spheres and between planes," *Journal of Magnetic Resonance, Series A*, vol. 104, no. 1, pp. 17-25, 1993.
19. Y. Assaf, T. Blumenfeld-Katzir, Y. Yovel, and P. J. Basser, "AxCaliber: a method for measuring axon diameter distribution from diffusion MRI," *Magnetic Resonance in Medicine*, vol. 59, no. 6, pp. 1347-1354, 2008.
20. D. C. Alexander, P. L. Hubbard, M. G. Hall, E. A. Moore, M. Ptito, G. J. M. Parker, T. B. Dyrby. "Orientationally invariant indices of axon diameter and density from diffusion MRI," *NeuroImage*, vol. 52, no. 4, pp. 1374-1389, 2010.
21. G. J. Stanisiz, G. A. Wright, R. M. Henkelman, and A. Szafer, "An analytical model of restricted diffusion in bovine optic nerve," *Magnetic Resonance in Medicine*, vol. 37, no. 1, pp. 103-111, 1997.
22. D. Barazany, P. J. Basser, and Y. Assaf, "In vivo measurement of axon diameter distribution in the corpus callosum of rat brain," *Brain*, vol. 132, no. 5, pp. 1210-1220, 2009.
23. H. Zhang, P. L. Hubbard, G. J. Parker, and D. C. Alexander, "Axon diameter mapping in the presence of orientation dispersion with diffusion MRI," *NeuroImage*, vol. 56, no. 3, pp. 1301-1315, 2011.
24. M. Mercredi, T. J. Vincent, C. P. Bidinosti, and M. Martin, "Assessing the accuracy of using oscillating gradient spin echo sequences with AxCaliber to infer micron-sized axon diameters," *Magnetic Resonance Materials in Physics, Biology and Medicine*, vol. 30, no. 1, pp. 1-14, Feb 2017.
25. M. G. Hall and D. C. Alexander, "Convergence and parameter choice for Monte-Carlo simulations of diffusion MRI," *IEEE Transactions on Medical Imaging*, vol. 28, no. 9, pp. 1354-1364, 2009.
26. L. E. Smart and E. A. Moore, *Solid State Chemistry: An Introduction*, 3rd ed. Boca Raton: CRC press, 2012.
27. E. Mittemeijer, "Chapter 9: Phase Transformations," in *Fundamentals of Materials Science: The Microstructure-Property Relationship Using Metals as Model Systems*, Heidelberg: Springer-Verlag, 2010.

28. O. Reynaud, K. V. Winters, D. M. Hoang, Y. Z. Wadghiri, D. S. Novikov, and S. G. Kim, "Surface-to-volume ratio mapping of tumor microstructure using oscillating gradient diffusion weighted imaging," *Magnetic Resonance in Medicine*, vol. 76, no. 1, pp. 237-247, Jul 2016.
29. P. P. Mitra, P. N. Sen, and L. M. Schwartz, "Short-time behavior of the diffusion coefficient as a geometrical probe of porous media," *Physical Review B*, vol. 47, no. 14, p. 8565, 1993.
30. P. P. Mitra, P. N. Sen, L. M. Schwartz, and P. Le Doussal, "Diffusion propagator as a probe of the structure of porous media," *Physical Review Letters*, vol. 68, no. 24, p. 3555, 1992.
31. G. Innocenti, R. Caminiti, and F. Aboitiz, "Comments on the paper by Horowitz et al.(2014)," *Brain Structure and Function*, vol. 220, no. 3, p. 1789, 2015.
32. D. J. Schaefer, J. D. Bourland, and J. A. Nyenhuis, "Review of Patient Safety in Time-Varying Gradient Fields," *Journal of Magnetic Resonance Imaging*, vol. 12, no. 1, pp. 20-29, 2000.
33. I. Drobnjak, B. Siow, and D. C. Alexander, "Optimizing gradient waveforms for microstructure sensitivity in diffusion-weighted MR," *Journal of Magnetic Resonance*, vol. 206, no. 1, pp. 41-51, 2010.
34. B. Gross and R. Kosfeld, "Anwendung der spin-echo-methode der messung der selbstdiffusion," *Messtechnik*, vol. 77, pp. 171-177, 1969.
35. P. Callaghan, C. Eccles, and Y. Xia, "NMR microscopy of dynamic displacements: k-space and q-space imaging," *Journal of Physics E: Scientific Instruments*, vol. 21, no. 8, p. 820, 1988.
36. P. J. Basser, "Inferring microstructural features and the physiological state of tissues from diffusion-weighted images," *NMR in Biomedicine*, vol. 8, no. 7, pp. 333-344, 1995.
37. Y. Cohen and Y. Assaf, "High b-value q-space analyzed diffusion-weighted MRS and MRI in neuronal tissues—a technical review," *NMR in Biomedicine*, vol. 15, no. 7-8, pp. 516-542, 2002.
38. J. C. Gore, A. W. Anderson, M. D. Does, D. F. Gochberg, J. M. Joers, R. P. Kennan, E. C. Parsons, and M. Schachter, "The relationship of problems in biomedical MRI to the study of porous media," *Magnetic Resonance Imaging*, vol. 19, no. 3-4, pp. 295-300, Apr-May 2001.
39. M. Schachter, M. D. Does, A. W. Anderson, and J. C. Gore, "Measurements of restricted diffusion using an oscillating gradient spin-echo sequence," *Journal of Magnetic Resonance*, vol. 147, no. 2, pp. 232-237, Dec 2000.
40. M. D. Does, E. C. Parsons, and J. C. Gore, "Oscillating gradient measurements of water diffusion in normal and globally ischemic rat brain," *Magnetic Resonance in Medicine*, vol. 49, no. 2, pp. 206-215, Feb 2003.

41. J. Kershaw, C. Leuze, T. Obata, I. Kanno, and I. Aoki, "Changes to the fractional anisotropy and mean diffusivity of in vivo rat brain measured at short effective diffusion-times," *Proc Intl Soc Mag Reson Med*, vol. 19, p. 409, 2011.
42. B. Siow, I. Drobnjak, A. Chatterjee, M. F. Lythgoe, and D. C. Alexander, "Estimation of pore size in a microstructure phantom using the optimised gradient waveform diffusion weighted NMR sequence," *Journal of Magnetic Resonance*, vol. 214, pp. 51-60, 2012.
43. E. C. Parsons, M. D. Does, and J. C. Gore, "Temporal diffusion spectroscopy: Theory and implementation in restricted systems using oscillating gradients," *Magnetic Resonance in Medicine*, vol. 55, no. 1, pp. 75-84, 2006.
44. S. Portnoy, J. Flint, S. Blackband, and G. Stanisz, "Oscillating and pulsed gradient diffusion magnetic resonance microscopy over an extended b-value range: Implications for the characterization of tissue microstructure," *Magnetic Resonance in Medicine*, vol. 69, no. 4, pp. 1131-1145, 2013.
45. J. Stepišnik, "Time-dependent self-diffusion by NMR spin-echo," *Physica B: Condensed Matter*, vol. 183, no. 4, pp. 343-350, 1993.
46. J. Laboy, University of Wisconsin-Madison. (2011, August). *Crystalline Lattices* [Online]. Available: <https://www.chem.wisc.edu/areas/clc/general/103/crystalLattices/lattices.htm#>
47. B. Harbick, L. Suh, and J. Fong. (2017, June). *Closest Packed Structures* [Online]. Available: https://chem.libretexts.org/Core/Physical_and_Theoretical_Chemistry/Physical_Properties_of_Matter/States_of_Matter/Properties_of_Solids/Crystal_Lattice/Closest_Pack_Structures
48. A. L. Sukstanskii, "Exact analytical results for ADC with oscillating diffusion sensitizing gradients," *Journal of Magnetic Resonance*, vol. 234, pp. 135-140, 2013.

Chapter 4

First OGSE Diffusion Spectroscopy Experiments

The experiments explained in this chapter were used to design phantoms, understand the relationship between phantom sizes and gradient frequencies, and to decide on pulse sequence parameters. With each experiment, we learned what did not work and changed what was needed to make the oscillating gradient spin echo (OGSE) diffusion spectroscopy measurements. The experiments in this chapter gave no results for the sizes of the tubes, and imprecise results for the smaller regions of interest (ROIs) that were drawn for the 3 μm bead sample. The information gained from those experiments enabled the experiments described in Chapters 5 and 6 which successfully inferred sizes in samples.

The first OGSE temporal diffusion spectroscopy experiments were performed to prove its ability to infer the size of very small structures on the order of microns. Using a frequency range of 50 Hz to 1 kHz with gradient strengths up to 909 mT/m (90% of g_{max} , $g_{max} = 1.01\text{T/m}$), pore sizes between 3 μm beads were inferred, and were within the range ($\sim 5 \mu\text{m}$) that other studies have reported. Based on the imprecise results that were given with the 3 μm bead phantom, as well as the lack of results in the tubes and microfluidic device, changes in the parameters used were necessary to improve results. Similar to other studies that infer micron-sized samples [1], there is an overestimation of small diameters and an underestimation of large diameters. The tube phantom and the microfluidic device used in these experiments did not provide any meaningful results due to their large diameters with respect to the high frequencies that were used in the experiments. Therefore the new phantoms were required to work with the known

parameters to reflect the simple geometries which could easily be incorporated into the AxCaliber and ActiveAx models. Such phantoms need to have tubes with smaller inner diameters ($< 5 \mu\text{m}$) that would be appropriate for testing OGSE to infer micron-sized diameters.

4.1 Methods

This section describes the three phantoms from which these temporal diffusion spectroscopy measurements using OGSE were made. Also the MR imaging and analysis methods used to collect and analyze these data are described here. The procedure for each phantom are summarized in a general outline as shown in Figure 4.1.

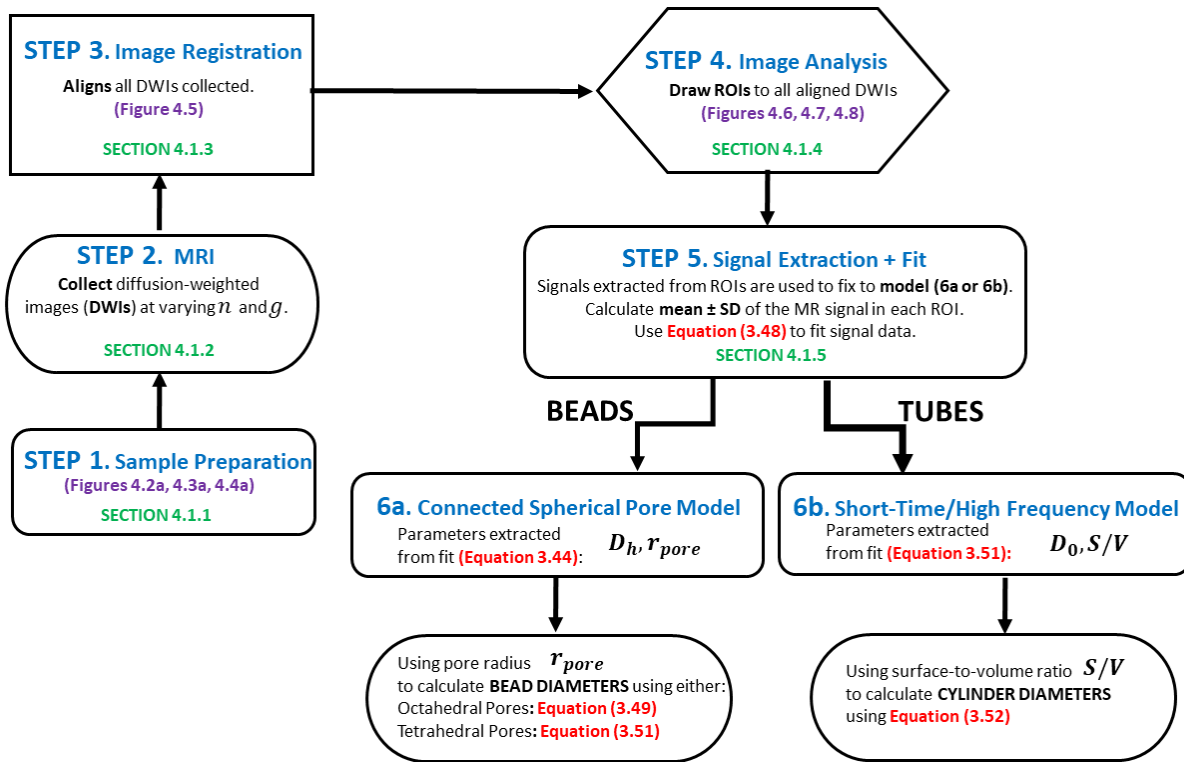


Figure 4.1: General outline of methods used for each experiment.

4.1.1 Description of the Samples

To test the apodised cosine OGSE sequence, phantoms were created to see their ability to determine the size of pores and calculating the corresponding diameters using Equations (3.49) and (3.50). Closely packed beads were used to infer the pore sizes between them and then determine their corresponding bead diameters. The diameter of cylindrical tubes were also inferred, first with microcapillary pipettes, and then with a custom-made microfluidic device acquired from Francis Lin's lab (Physics & Astronomy, University of Manitoba). The goal was to create phantoms with pores $<10\ \mu\text{m}$ in diameter and verify that the OGSE sequence can infer the size of axon diameters within this range.

4.1.1.1 3 μm Beads

Polystyrene beads in water which were $3\ \mu\text{m}$ diameter (10% solid, Sigma Aldrich, Inc., Oakville ON) were placed into a $500\ \mu\text{L}$ microcentrifuge tube (Cole-Parmer Canada, Montreal QC). Beads were transferred into this sample tube using a pipette. The tube was centrifuged a total of 4 times in 10 - 15 second intervals at a speed of 5000 rpm. Between each interval, any excess water was removed at the top of the sample tube and then more bead solution was added. This continued until the sample tube was filled well past the tapered end of the tube and allowing for the bead solution to be packed halfway up the widest width of the tube. After the last centrifuging, the water that remained at the top of the sample tube and more water was added to ensure the tube was full (Figure 4.2a).

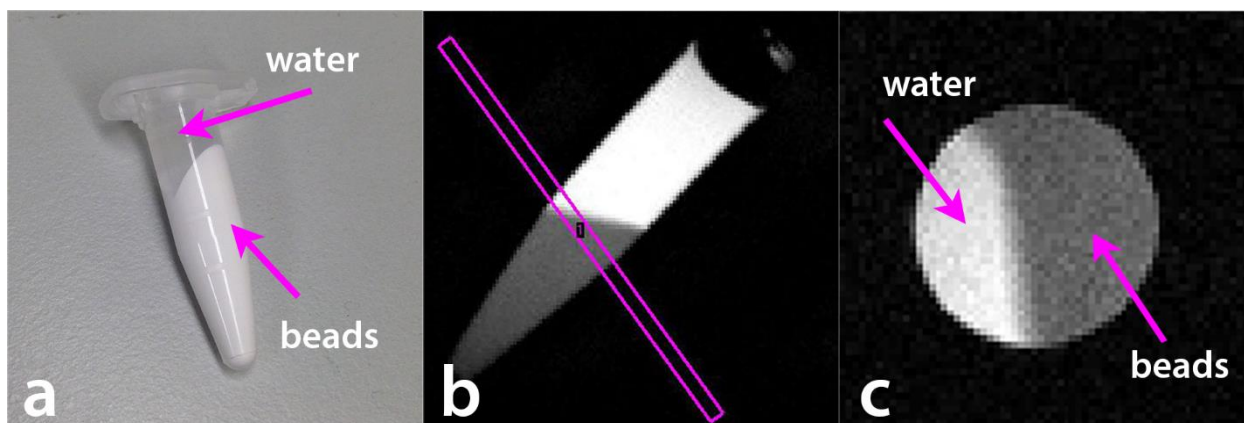


Figure 4.2: 3 μm bead phantom. (a) Optical image of the 3 μm bead phantom. Polystyrene beads (3 μm diameter, Sigma Aldrich) in water were transferred into a sample tube with a pipette and centrifuged. (b) MR image showing the image slice used in experiment. The slice was taken to include the bead only and water only portions of the sample. (c) MR image of the image slice cross section taken from (b).

4.1.1.2 Microcapillary Pipettes

Ten Kimble© microcapillary pipettes (Sigma Aldrich, Inc., Oakville ON) were used in total, with each filled with copper sulfate (CuSO_4) solution (Bruker Biospin, Milton ON, $\text{CuSO}_4 \times 2 \text{H}_2\text{O}$, 1 g/L). The inner diameter of the tubes was approximately 780 μm . Tubes were bundled together using tape, and each end of the pipette was secured with plastic adhesive putty to keep the solution within and prevent drying. This tube bundle was contained within a 15 mL sample tube (Figure 4.3a) before being placed into the 3.5 cm diameter bird cage RF coil.

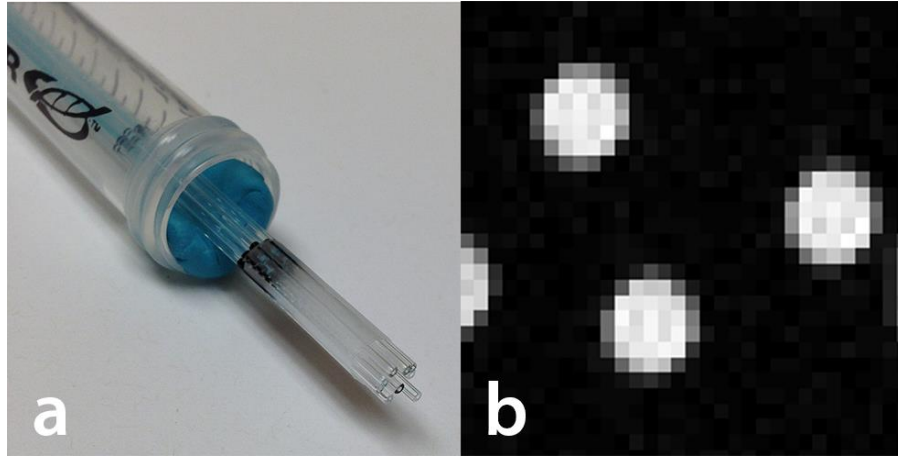


Figure 4.3: Tube phantom. (a) Optical image of the tube phantom. Microcapillary pipettes (10 tubes, Sigma Aldrich) each were filled with CuSO_4 solution (Bruker Biospin). Tubes were bundled together using tape, with the ends being secured with plastic adhesive putty to keep the solution with the open ends of the tube and prevent drying. This sample was then contained within a 15 mL sample tube before being placed into the 3.5 cm diameter bird cage RF coil. (b) MR image of the slice cross section taken for the experiment.

4.1.1.3 Microfluidic Device

A simple microfluidic device created by Francis Lin's lab (Physics & Astronomy, University of Manitoba) was used. This device consisted of a 'Y' type fluidic channel, as mentioned in [2] and contained channels for fluid that formed a 3- pronged forked shape. The main fluidic channel has dimensions of $100 \mu\text{m}$ (H) \times $350 \mu\text{m}$ (W) \times 12 mm (L). This device was filled with CuSO_4 solution (Bruker Biospin, Milton ON, $\text{CuSO}_4 \times 2 \text{ H}_2\text{O}$, 1 g/L) by placing a pipet tip attached to a syringe into the three inlets (1 mm diameter holes) of the device (Figure 4.4a). For stability during the experiment, this device was secured within a 45 mL sample tube before being placed within the 3.5 cm diameter bird cage RF coil.

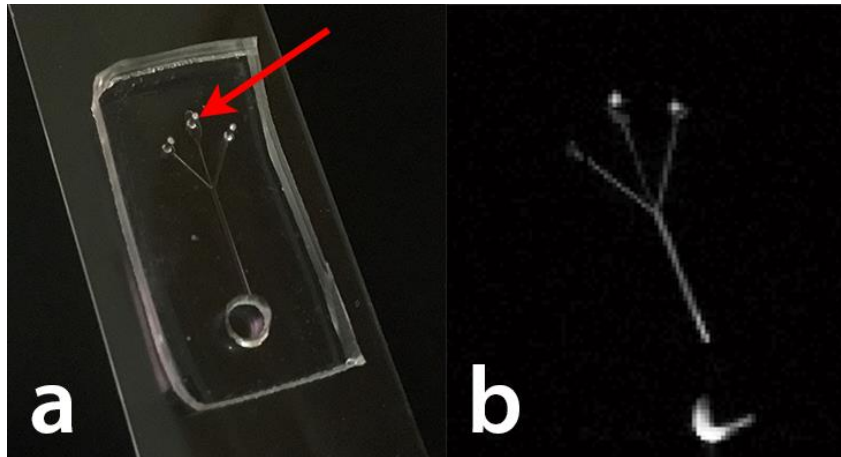


Figure 4.4: Microfluidic device. (a) Optical image of the microfluidic device. The channels in the device were injected using a modified syringe with CuSO_4 solution through the inlets as indicated by the red arrow. This device was then placed within a 45 mL sample tube before being placed within the 3.5 cm diameter bird cage RF coil. (b) MR image of the slice cross section taken for the experiment

4.1.2 MRI Parameters

Experiments were performed using a 7 T Bruker Avance III NMR system with Paravision 5.0, a BGA6 gradient set with maximum gradient strength, g_{max} , of 1.01 T/m (or 430357 Hz/cm), and a 3.5 cm diameter bird cage RF coil (Bruker Biospin, Milton, ON). A schematic of the magnet, gradient set, and RF coil configuration can be found in Appendix A.1. For all the experiments in this chapter, the apodised cosine sequence was used, as described in Section 3.5.3. The specific parameters used for each phantom are described in this subsection, and are also presented in tables found in Appendix B.1.1 and B.1.2.

Gradient strengths g_i (where $i = 0 - 4$) were a percentage of the maximum gradient strength g_{max} . The gradient strengths were chosen to account for enough change in the decay between

all the points for the gradient pulse and also to maintain reasonable SNR. Explanation for the calculation of the maximum number of points for each period is explained in Appendix B.1.

Visually, these gradient strengths allowed for a lot of signal decay with good SNR in the images, giving as much signal decay as possible and detectable signal decay between images with increasing gradient strengths.

4.1.2.1 Bead Phantom Parameters

The number of sinusoidal waves in each 20 ms apodised cosine [3] gradient pulse ranged from $n = 1$ to 20, in steps of 1 corresponding to frequencies of $n/20$ ms or 50 Hz to 1 kHz. Five gradient strengths were used for each frequency and were separated by 24.52 ms (Appendix B.1.1)

The phantom was placed at a slight angle in order to fit inside the RF coil, and was done to allow the chosen slice to simultaneously encompass the regions of the packed beads and the water (Figure 4.2b). The chosen slice was 1 mm thick, $(2\text{ cm})^2$ in-plane FOV, with a 128×128 matrix that was used for $156\ \mu\text{m}$ in-plane resolution. Other parameters were $TE = 50$ ms, $TR = 1250$ ms, number of averages (NA) = 2, and an acquisition time of 26.67 minutes per scan. A total of 160 scans were performed, or 8 sets were obtained (each set contained 20 frequencies each using 5 gradient strengths). Overall this experiment collected a total of 800 images, with a total imaging time of ~ 72 hours.

4.1.2.2 Tube Phantom Parameters

The number of sinusoidal waves in each 60 ms apodised cosine gradient pulse ranged from $n = 1$ to 20, in steps of 1 corresponding to frequencies of $n/60$ ms or 16.7 Hz to 333 kHz. Five gradient strengths were used for each frequency and were separated by 64.52 ms (Appendix B.1.2). The tube phantom was contained within a 15 mL sample tube before being placed into the RF coil.

The chosen slice taken perpendicular to the direction of the tubes was 3.0 mm thick, $(3.2 \text{ mm})^2$ in-plane FOV, with a 32×32 matrix that was used for 100 μm in-plane resolution. Other parameters were $TE = 169.066$ ms, $TR = 1250$ ms, $NA = 8$, and an acquisition time of 26.67 minutes per scan. In total 180 scans or 9 sets of scans were performed which collected 900 images having with a total imaging time of ~ 81 hours.

4.1.2.3 Microfluidic Device Parameters

As with the bead sample, the number of sinusoidal waves in each 20 ms apodised cosine [3] gradient pulse ranged from $n = 1$ to 20, in steps of 1 corresponding to frequencies of $n/20$ ms or 50 Hz to 1 kHz. Five gradient strengths were used for each frequency and were separated by 24.52 ms (Appendix B.1.1).

The chosen slice was a 3.0 mm thick, $(3 \text{ cm})^2$ in-plane FOV, with a 128×128 matrix that was used for 234 μm in-plane resolution. Other parameters were $TE = 50$ ms, $TR = 1250$ ms, $NA = 2$, and an acquisition time per scan of 26.67 minutes. In total 120 scans or 6 sets of scans were performed, which collected a total of 600 images, and had a total imaging time of ~ 54 hours.

4.1.3 Image Registration

As with previous data sets using multiple images collected in the Martin lab over a period of several hours or days, image registration was used [4]. Images collected over several days can be shifted a fraction of a voxel due to the Larmor frequency drift and slight alignment issues of the RF coil within the gradient insert can cause the sample to move. In order to account for any shift during these long imaging sessions, an image registration method was used in Matlab (Mathworks, Natick, MA) [4]. The image registration was also performed to provide consistency between all the experiments in this project. This custom-built image registration tool was used to calculate an affine transformation matrix automatically to match the 2D target images ($g_1 - g_4$ images) to the 2D reference image (g_0 image) [4]. Figure 4.5a shows how the reference image, which is the first g_0 image obtained from the first imaging scan was used to align all other images obtained by the subsequent scans, called the target images. For example in the 3 μm bead experiment (Figure 4.5a), the first image obtained during the first imaging scan was used as the reference image to register all of the other target images from subsequent scans. In this example, comparing the reference image to the target image, which was taken from a later imaging scan (scan #140), the shift in the beads within the sample tube is evident.

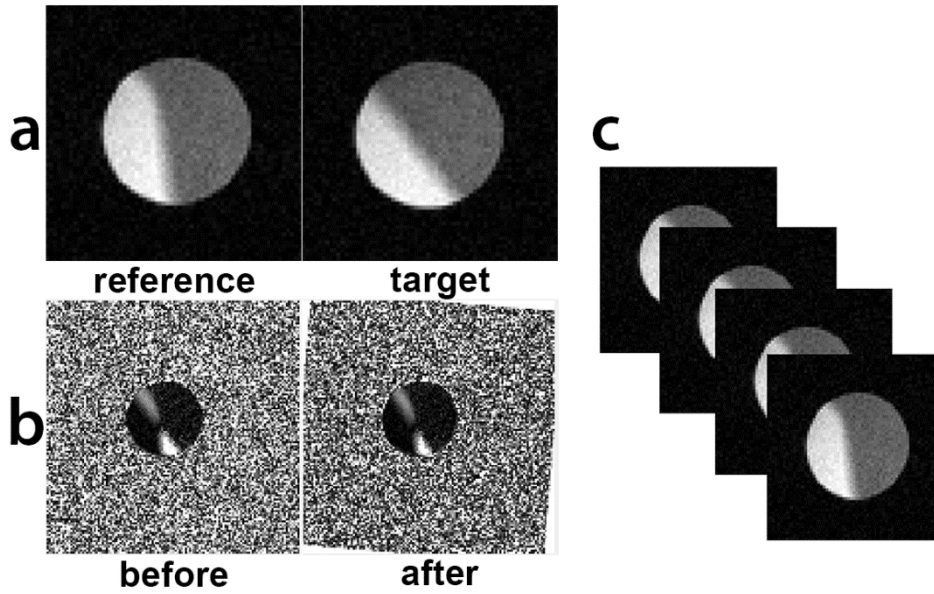


Figure 4.5: Image registration procedure. (a) Reference and target images show how the images have shifted during the long imaging sessions. The first g_0 image from the first imaging scan was used as the reference image. All other images used in each experiment are the target images. In this figure, the target image was taken from the last of the 140 image scans. (c) Percent difference image shows the differences between the target and reference images and how they overlap. After image registration, the reference image has been aligned to the target image, as shown. (c) All target images are registered to the reference image in the data set.

An affine transformation matrix was used to represent the translation, scale, and shear of the x- and y-directions, as well as the rotation. Parameters were used as starting points for the auto-registration. Auto-registration is bounded by user-defined values for each parameter, which can be manually changed at any point to redraw the images. This program minimizes the difference between the two images.

Once image registration has been performed, these registered images are then used to extract information from the signals by arbitrarily drawing regions of interest (ROIs) within the MR images (Figure 4.5c).

4.1.4 Image Analysis

Regions of interest (ROIs) were drawn in the images as described in Sections 4.1.4.1 - 4.1.4.3. For all the phantoms used in the experiments, the mean \pm standard deviation was calculated for all the signals within the ROIs and was then used in the fits explained in Section 4.1.5. Caution was used when drawing the ROIs for the noise to ensure the ROI was placed outside of any region containing artefacts such as ghosting.

4.1.4.1 Bead Phantom Analysis

For the MR images of the 3 μm beads (Figure 4.2c), ROIs were arbitrarily drawn in the water region of the bead sample (black ROI), in the bead region of the bead sample (magenta ROI), and in the background to get a measure of the noise, which is referred to as the noise ROI (red ROI) (Figure 4.6).

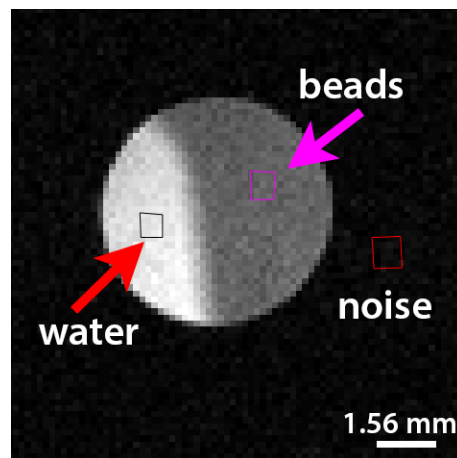


Figure 4.6: MR image was used to draw the ROIs. ROIs were created from in the water region of the bead sample (black ROI), in the bead region of the bead sample (magenta ROI), and in the noise (red ROI). The signal used in the fits was from the bead region. The signal from the water region was used as a control to ensure the measured diffusion coefficient was constant throughout the experiment and as the free diffusion coefficient used in the model.

4.1.4.2 Tube Phantom Analysis

From the MR images obtained (Figure 4.3b), ROIs were arbitrarily drawn within the sample of the microcapillary pipettes (ROIs 1 - 3), and in the background to get a measure of the noise, referred to as the noise ROI (ROI 4) (Figure 4.7).

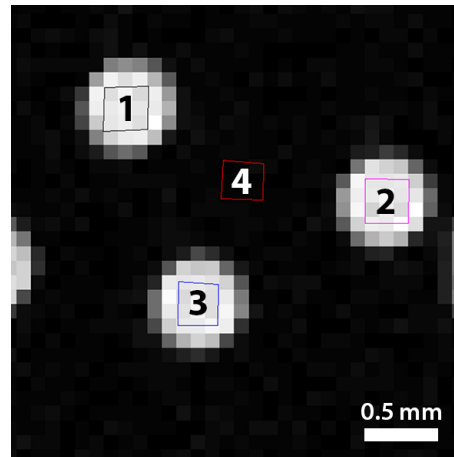


Figure 4.7: ROIs were chosen in the outside noise (ROI 4), and within the sample containing the CuSO_4 solution (ROIs 1-3). Mean and SD of the signals in these ROIs were calculated

4.1.4.3 Microfluidic Device Analysis

Using the MR images obtained (Figure 4.4b), ROIs were drawn to encompass all of the channels of the device (ROIs 2-6), and in the background to get a measure of the noise, referred to as the noise ROI (ROI 1) (Figure 4.8).

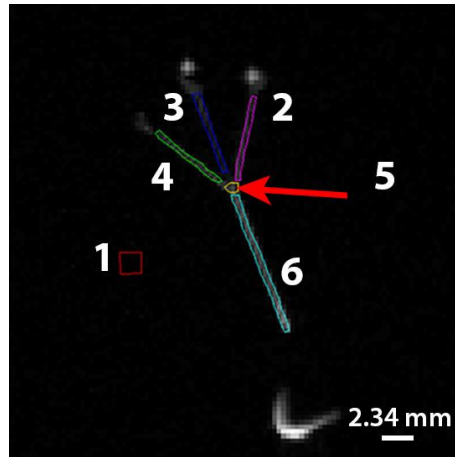


Figure 4.8: ROIs were drawn on this MR image along the channels of the device (ROI 2-6) and the noise outside the sample (ROI 1). Mean and SD of the signals in these ROIs were calculated.

4.1.5 Signal Extraction and Fit

Regions of interest (ROIs) were drawn in the images as described in Sections 4.1.4.1 - 4.1.4.3.

For all the phantoms used in the experiment, the mean \pm standard deviation (SD) was calculated for all of the signals extracted from all the voxels contained within the ROIs. The signals are represented as the intensity in the images. These signals were fitted to Equation (3.48) to obtain the ADC in each voxel as a function of frequency. Using Equation (3.48), the log of the signal versus b-value from the oscillating gradients was fitted to a straight line and the negative of the slope was used as the ADC for each measurement for the water ROIs. The mean and standard deviation of the other ROIs were used in the fits to extract sample parameters as described below.

In the bead experiment, as described in Section 3.5.4, using the connected spherical pore extra-cellular model (Equation (3.44)), the signals obtained from the ROIs of the bead region were used to fit this model to extract the parameters: long-time diffusion coefficient D_h and the pore

radius. The signal from the water regions were used as a control to ensure the measured diffusion coefficient was constant throughout the experiment and also used as the free diffusion coefficient, D_0 in the model. Using the two types of interstitial holes, i.e. the octahedral and tetrahedral holes (Section 3.5.4), pore size was related to bead diameter using their respective equations (Equations (3.49) and (3.50)).

In both the tubes and microfluidic device experiments, as described in Section 3.5.5, using the short-time or high frequency model, Equation (3.51), the signals obtained from the ROIs of the tube regions were used to fit this model to extract the parameters: D_0 and S/V . The signal from the water regions were used as a control to ensure the measured diffusion coefficient was constant throughout the experiment and also used as the free diffusion coefficient, D_0 in the model. The surface-to-volume ratio was related to the cylinder diameter using Equation (3.52).

4.1.5.1 Bead Phantoms Fit

Signal data were fitted by the model with nonlinear least-squares regression using the Optimization Toolbox in Matlab (Mathworks, Natick, MA). The long-time diffusion coefficient was constrained to the range $[0, 2] \mu\text{m}^2/\text{ms}$ where the diffusion coefficient of free water at room temperature is $2 \mu\text{m}^2/\text{ms}$. The long-time diffusion coefficient is smaller than the free diffusion coefficient. Thus values of long-time diffusion coefficients greater than $2 \mu\text{m}^2/\text{ms}$ were not physical possibilities. The pore radius was constrained to the range $[0, 5] \mu\text{m}$ because it was expected to be no larger than the bead radius.

4.1.5.2 Tube Phantom and Microfluidic Device Fits

Signal data were fitted by the model with nonlinear least-squares regression using the Optimization Toolbox in Matlab (Mathworks, Natick, MA). The diffusion coefficient was constrained to the range $[0, 3] \mu\text{m}^2/\text{ms}$. The surface-to-volume ratio (S/V) was constrained to the range $[0, 0.2] \mu\text{m}^{-1}$ for similar reasons as the beads.

4.2 Results

The results for each of the three phantoms are summarized in this section. Plots of the apparent diffusion coefficient vs OGSE frequency are presented. For the bead phantom, the pore radius and corresponding bead diameter, and the long-time diffusion coefficient inferred from the data are presented. The tube phantom and microfluidic device experiments however did not produce reasonable results.

4.2.1 Bead Phantom Results

Using the 800 images similar to the one shown in Figure 4.2c, signals were extracted from each ROI and fitted with Equation (3.48) to obtain the ADC in each voxel as a function of frequency. As mentioned in Section 4.1.5, ADC was obtained using the signals obtained from the drawn ROI, and the ADC versus frequency is plotted (Figure 4.9). The fit was obtained using Equation (3.44) (Section 3.5.4) and is shown with a dashed blue line in Figure 4.9. The fit determined that the pore radius between beads was $0.6 \pm 0.5 \mu\text{m}$, containing water diffusing at $1.4 \pm 0.1 \mu\text{m}^2/\text{ms}$.

This pore radius corresponds to bead diameters ranging from $3 \pm 2 \mu\text{m}$ to $5 \pm 4 \mu\text{m}$ (using Equations (3.49) and (3.50) respectively).

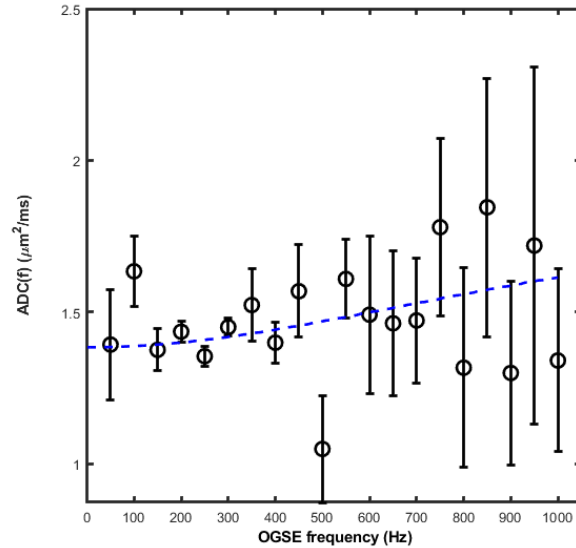


Figure 4.9: The diffusion spectrum for the bead sample. ADC of water surrounding the beads is plotted versus frequency. The fit to Equation (3.44) is shown with the dashed blue line. Data points are mean \pm standard deviation of the ADC for each frequency. The pore radius was found to be $0.6 \pm 0.2 \mu\text{m}$ with long-time diffusion coefficient $1.38 \pm 0.06 \mu\text{m}^2/\text{ms}$. The standard deviation in measurements at higher frequencies increases because of the smaller signal decay between measurements.

4.2.2 Tube Phantom Results

Using the 900 images similar to the one shown in Figure 4.3b, signals were extracted from each ROI and fitted with Equation (3.48) to obtain the ADC in each voxel as a function of frequency. The diffusion spectrum of the water in the tube samples was assumed to follow the equation for cylinders, Equation (3.51). However, for the tube data, the diffusion was constant at the free diffusion coefficient. Thus the fit did not produce reasonable results. We believe that the frequencies used in the experiments was too high to allow for restricted diffusion to occur within

the tubes. Restricted diffusion is necessary for the fits used to determine the tube diameter measurements. These high frequencies used, which correspond to short diffusion times made the water within the $\sim 780 \mu\text{m}$ inner diameter tubes to experience unrestricted diffusion during the measurements, as shown in Figure 4.10.

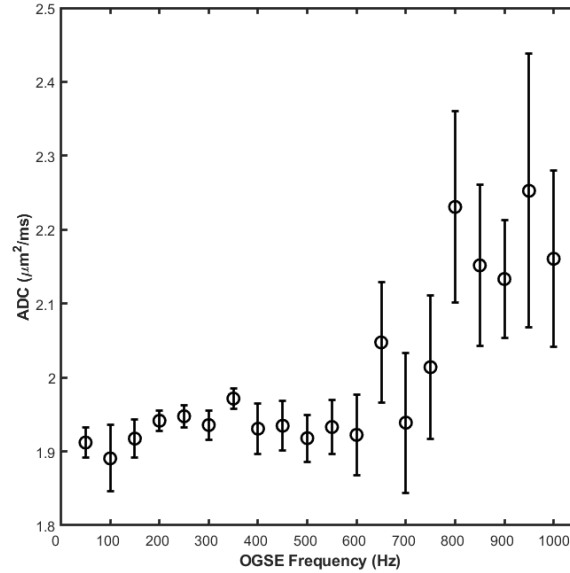


Figure 4.10: The diffusion spectrum for the tube sample. ADC of water contained within the microcapillary pipettes is plotted versus frequency. The fits did not produce meaningful results. Frequencies used in this experiment were too high. Tube inner diameters were too large $\sim 780 \mu\text{m}$. Thus the solution in the tubes only experienced unrestricted diffusion

4.2.3 Microfluidic Device Results

Using the 600 images similar to the one shown in Figure 4.4b, signals were extracted from each ROI and fitted with Equation (3.48) to obtain the ADC in each voxel as a function of frequency. Similar to the microcapillary pipettes, the size of these channels ($\sim 250 \mu\text{m}$) was still too large for the high frequencies we are using. The fits did not produce meaningful results.

4.3 Discussion

In the bead experiment which studied extracellular water, the error bars in the ADC were large, especially for the high frequencies that were used (Figure 4.9). These experiments collected images for approximately 72 hours and because of this long imaging time collecting more sets of images which could be averaged together with the other sets of images was not practical. In the next chapter, analysis was re-done using much larger regions of interest to help increase the signal-to-noise ratio of the signal used in the fits. Another problem that arose from this experiment was that the bead phantom was oriented in such a way so that the top part of the tube contained pure water while the bottom part of the tube contained beads packed in water. The sample tube was too large to stand vertically into the RF transceiver coil and it was instead placed at an angle. However, due to the long imaging session in conjunction with the movement of the RF coil over time, this caused the sample tube to tip over or shake, changing the packing of the beads and the bead-water boundary. Because of this, the experiments performed on the bead phantoms in Chapter 5 separated the beads from the water, by placing an external water tube and then bundled together with the bead samples.

The tube experiments were used to test OGSE for intracellular water. The diameters of the microcapillary pipettes and the channels in the microfluidic device were much too large for the frequencies used in the experiment. Based on the extracellular experiment on the bead phantom, we need to have tube phantoms with the same diameter range, between 3 and 10 μm .

4.3.1 Preparation of the Smaller Tube Phantom

The experiments in this chapter described so far has suggested that tubes with smaller inner diameters were needed in order to test the frequencies used in these OGSE experiments. Smaller tubes were needed rather than smaller frequencies because the ultimate goal of this work is to infer micron-sized axon diameters.

Capillary tubing (Polymicro Technologies/ Molex Inc., Phoenix, AZ) of inner diameters of 2, and 5 μm , both with an outer diameter of 151 μm were used in the experiment in Chapter 5.

However, because of the size of the inner diameters of the tubing, filling these tubes proved to be difficult. There were two attempts to fill the tubing mentioned in the subsections below. In Chapter 5, the tube phantom that was used in the experiment was created using the second attempt discussed in Section 4.3.1.2.

4.3.1.1 Filling the tubing (First Attempt)

Capillary tubing (2 and 5 μm) were cut into 2 cm pieces (approximately 50 pieces each) and initially were injected with copper sulfate (CuSO_4) using a modified syringe [5]. CuSO_4 was used because it was easier to see it being filled instead of using just water. This injection method proved to be difficult because the diameters of the tubing were so small that it was impossible to manually inject each of the tubes with the syringe by hand. Instead, these 2 cm pieces were then soaked in the CuSO_4 for a week, with the hopes that the tubes would be filled by capillary action as shown in Figure 4.11.

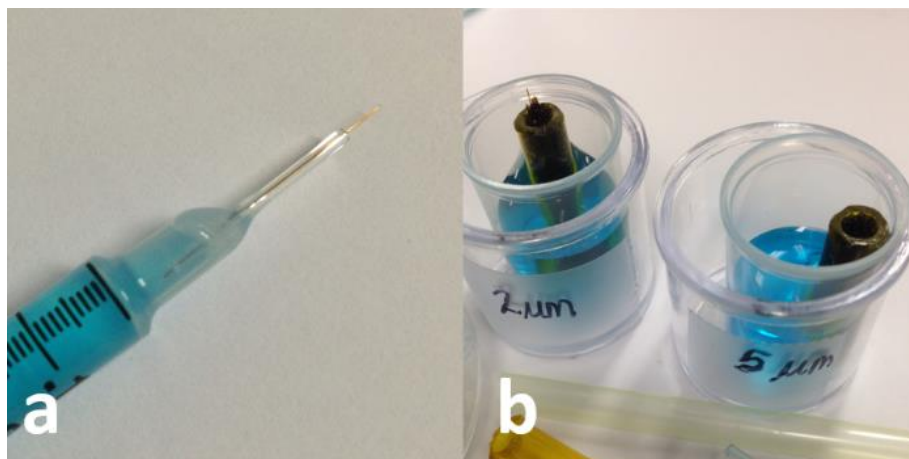


Figure 4.11: (a) Capillary tubing (inner diameters of 2 and 5 μm) were cut into 2 cm pieces and CuSO_4 was injected using a modified syringe [5]. (b) Manually injecting the solution within the tubing proved difficult and therefore these pieces were soaked in CuSO_4 .

Unfortunately, most of the tubes were not completely filled from capillary action because the CuSO_4 solution was evaporating while the tubes were being soaked. When the CuSO_4 solution evaporated it might have left residue as it dried in the tubes causing the tubing to clog, resulting in a sample that was not usable.

4.3.1.2 Filling the tubing (Second Attempt)

The capillary tubing was cut into 50 cm pieces (approximate) and filled with water using a modified syringe [5] attached to extension clamps to ensure the filtered water was being pushed into the capillary tubing (Figure 4.12). Due to the very small size of the inner diameter tubing, 3-pronged extension clamps (Cole-Parmer, Montreal QC) were necessary to push the filtered water continuously into the tubing. These pieces of tubing were left overnight up to 48 hours to fill. Initial testing on filling these tubes were done in Dr. Doug Craig's lab (Chemistry, University of Winnipeg), where the first set of tubing was filled using filtered water with

fluorescein dye that could be viewed under a laser-induced fluorescence detector [5] to ensure that the tubing was indeed being filled using this method.



Figure 4.12: Capillary tubing was filled with filtered water using a modified syringe [5] and a 3- pronged extension clamp to push the filtered water into the tubing.

Tubing was then cut into 2 cm pieces (1341 in total), and then packed with a 500 μ L plastic microcentrifuge tube (Cole-Parmer Canada, Montreal QC). Only the 5 μ m tubing was used in this experiment as explained in Chapter 5.

Initially these tubing were meant to measure the ‘intracellular’ water within the inner diameters of the tubing but the volume within each of the tubes in the sample was not large enough to produce a measurable signal. Thus the intracellular water could not contribute to the measured signal. This sample was instead used for the experiments on ‘extracellular’ water, for measurements of the outer diameter as discussed in Chapter 5. The tubes themselves were meant to model axons while the space between the tubes was meant to model the extracellular compartment.

4.4 Conclusions

This chapter explained the preliminary experiments which helped design the OGSE experiments as described in the following chapters. While the results from these preliminary experiments were unsatisfactory, they provided very useful information about sample sizes for the frequency ranges being studied. Bead diameters were inferred to be in the expected range but the precision of the results needed improvement.

References

1. M. Mercredi, T. J. Vincent, C. P. Bidinosti, and M. Martin, "Assessing the accuracy of using oscillating gradient spin echo sequences with AxCaliber to infer micron-sized axon diameters," *Magnetic Resonance Materials in Physics, Biology and Medicine*, vol. 30, no. 1, pp. 1-14, Feb 2017.
2. F. Lin and E. C. Butcher, "T cell chemotaxis in a simple microfluidic device," *Lab on a Chip*, vol. 6, no. 11, pp. 1462-1469, 2006.
3. M. D. Does, E. C. Parsons, and J. C. Gore, "Oscillating gradient measurements of water diffusion in normal and globally ischemic rat brain," *Magnetic Resonance in Medicine*, vol. 49, no. 2, pp. 206-215, Feb 2003.
4. J. D. Thiessen, Y. Zhang, H. Zhang, L. Wang, R. Buist, M. R. Del Bigio, J. Kong, X.-M. Li, and M. Martin, "Quantitative MRI and ultrastructural examination of the cuprizone mouse model of demyelination," *NMR in Biomedicine*, vol. 26, no. 11, pp. 1562-1581, 2013.
5. D. B. Craig, "A simple system for the measurement of the distribution of activities of individual molecules of E. coli β -galactosidase," *Analytical Methods*, vol. 4, no. 1, pp. 85-88, 2012.

Chapter 5

Inferring Diameters of Spheres and Cylinders using

Extracellular water

The data discussed in this chapter constitute the majority of the data accepted for publication in the journal *Magnetic Resonance Materials in Physics, Biology and Medicine* [1].

This thesis has explained the need for *in vivo* axon diameter measurements and their potential for clinical use. Previous measurements used the PGSE sequence that was insensitive to clinically relevant axons. Monte Carlo simulations [2] indicated the feasibility of using OGSE to make inferences of micron-sized axon diameters using the gradient strengths available on our BGA6 gradient set from Bruker Biospin (Bruker Biospin, Ltd., Milton, ON). The measurements in Chapter 4 using bead phantoms demonstrated the feasibility of these methods to infer micron-sized restrictions in samples and provided insight into means of improving the methods. The experiments in this chapter were designed to study other improvements to the model.

A common problem with MRI temporal diffusion spectroscopy methods has been the underestimation of the diameter of larger axons [3, 4]. This underestimation is a result of incorrect modelling of extracellular water [2] which appears to contribute the dominant effect for determining sizes [5-8]. The extracellular water in these models is assumed to undergo hindered diffusion with the apparent diffusion coefficient of the extracellular water (ADC_e) being constant with diffusion time [4, 9, 10] or linear with diffusion time [3]. Note that the diffusion time used in PGSE is related to the inverse of the gradient frequency in the OGSE sequence. While for the

long diffusion times used in some single diffusion encoding diffusion sequences this approximation of constant or linear ADC_e appears valid, as diffusion times are shortened or higher frequencies are used, this assumption breaks down. In a previous simulation study it was observed that as the diffusion frequency increased, corresponding to shorter diffusion times, the extracellular water apparent diffusion coefficient increased non-linearly. This was because the diffusion became less hindered and more free due to the extracellular water was not experiencing the complete extracellular space [2]. This caused the diffusion to be modeled incorrectly which resulted in the incorrect inferences of the axon diameter distributions. Restricting the range of diffusion frequencies used in experiments so that the extracellular water experienced hindered diffusion with a constant apparent diffusion coefficient for all measurements allowed the inference of axon diameter distributions to be more accurate at the expense of limiting the range of sizes that could be inferred [2]. Thus, it is desired to allow for non-linearly time varying apparent diffusion coefficients of the extracellular water.

In this chapter, data from two different geometrical phantoms (beads and tubes) are presented which were required with OGSE sequences to determine the sizes of pores in the samples. The apodised cosine OGSE [11, 12] was used to infer the pore size between closely packed bead and the corresponding bead diameter, as well as the inference of the diameter of cylindrical tubes. In this model we no longer assume the ADC_e is constant with diffusion time (or frequency).

Instead the model is changed so that ADC_e can change with diffusion time. For the bead samples, the connected spherical pore model is used. In this model, the pores are modelled as spheres and signal is fitted to the equations for water diffusing in spheres, but with the addition of a long time tortuosity term [13]. The extracellular water in the cylindrical sample was modelled to be in the short time regime [14, 15].

The validity of the measurements of pore radii using the bead samples was studied using other micron-sized beads (6 and 10 μm). This experiment also used an external water tube to separate the water from the beads and overcome the problem that occurred with the 3 μm bead phantom. Based on the previous experiments on the tube phantom, a second tube phantom was created with tubes of a smaller inner diameter (5 μm). Two extracellular models were tested to infer diameters on micron-sized phantoms. The first model, the connected spherical pore model (Section 3.5.4), was used to extract the pore radius used to determine the corresponding bead diameters for micron-sized bead phantoms. The second model, the short-time/high frequency model (Section 3.5.5), extracted the surface-to-volume ratio (S/V) that was used to determine the corresponding tube diameters for micron-sized tube phantoms. The results from these experiments provided a better idea of the resolution limit and the range of gradient strengths and frequencies are required.

5.1 Methods

This section describes the four phantoms used to measure temporal diffusion spectroscopy with the oscillating gradient spin echo (OGSE) method. Also, the MRI acquisition and analysis methods are described here. The procedure for each phantom are summarized in a general outline shown in Figure 5.1.

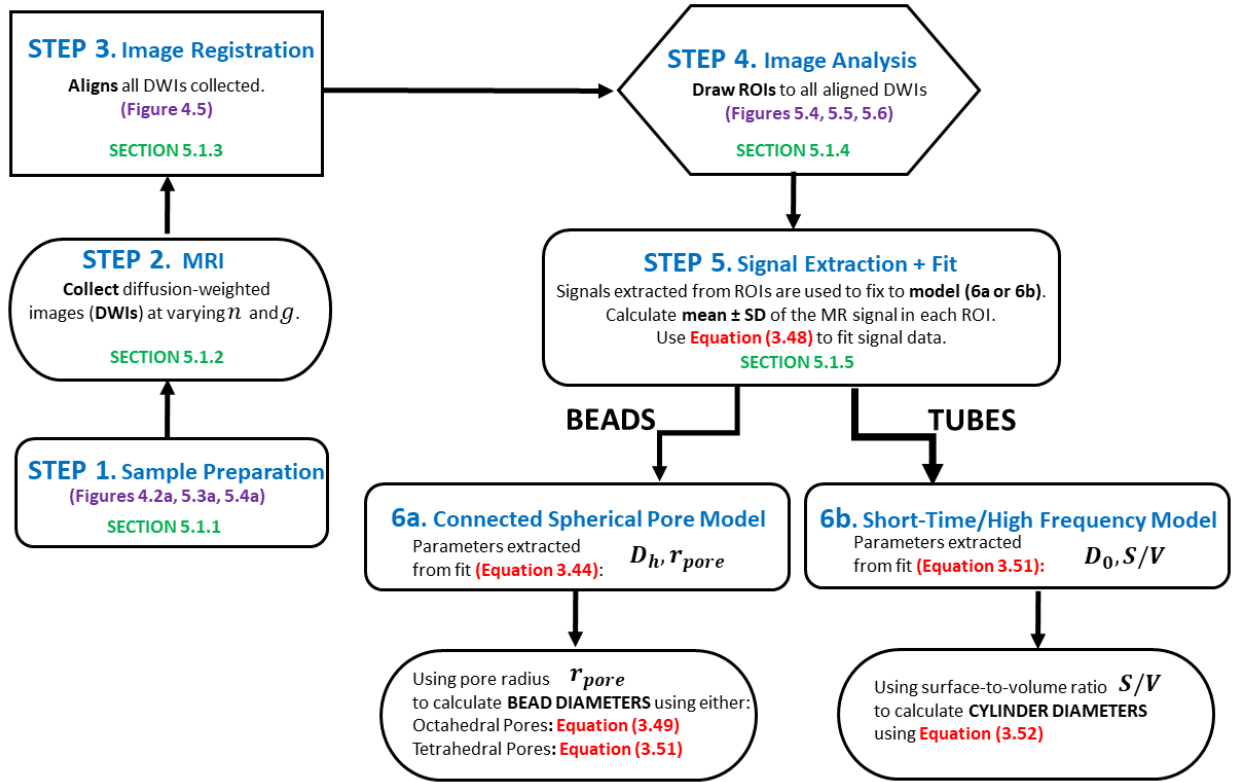


Figure 5.1: General outline of methods used for each experiment.

5.1.1 Description of the Samples

All samples used in the experiments described in this chapter have water only in one compartment, the extracellular compartment. Three bead phantoms comprised of packed polystyrene beads, and a tube phantom consisting of a sample tube packed with capillary tubing were studied.

5.1.1.1 3 μm Beads

The images from the closely packed polystyrene bead phantom in Chapter 4 were re-analyzed in this chapter (Section 4.1.1.1). Because these studies were made to test the “extracellular” model, the bead phantom was chosen so that the beads represent the cells and the space between the beads represented the “extracellular” compartment. The water in the pores between the beads was modeled as “extracellular” water in the analytical equation described in Section 3.5.4. The polystyrene beads contained no water therefore “intracellular” water was not included in the model.

The ROIs for the 3 μm bead phantom from Section 4.1.4.1 were redone with much larger ROIs that encompassed most of the sample (see Section 5.1.4.1 and Figure 5.4). This offered better a signal-to-noise ratio which in turn offered more precise inferences of pore sizes.

5.1.1.2 6 and 10 μm Beads

The validity of the measurements of the pore radii using the beads was studied by creating a new phantom that had two different sized beads that were imaged simultaneously. Polystyrene beads in water were used, of 6 and 10 μm diameters (2.5 % solid, Polysciences Inc., Warrington PA) and each were placed into their own 500 μL microcentrifuge/sample tube (Cole-Parmer Canada, Montreal, QC). To pack the beads in the water, the 6 and 10 μm bead samples were centrifuged for a total of 27 and 33 times respectively, each time for 15- 20 seconds at 5000 rpm. Between each interval, any excess water was removed, and more bead solution was added.

To serve as a control, another sample tube was filled with water using a 750 μm diameter capillary tube filled with CuSO_4 placed beside the 6 μm diameter bead sample, this was used to distinguish between the two bead samples as shown in the optical image (Figure 5.2a). These samples were then held together using Teflon tape to ensure that it could fit and stand upright within the RF coil. The samples were placed within the RF coil so that the tubes stood up vertically as best as possible, to prevent any shifting of the beads within the sample.

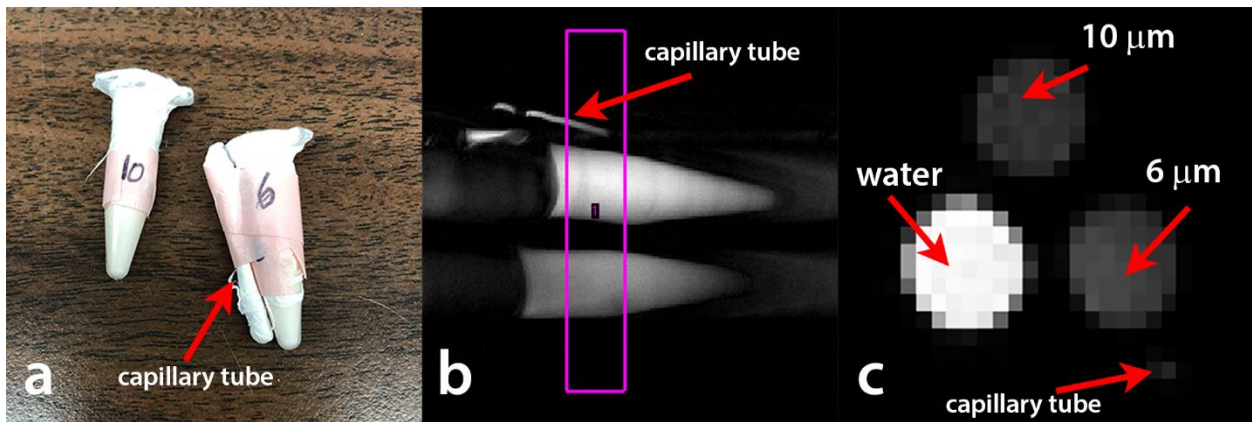


Figure 5.2: 6 and 10 μm bead phantom. (a) Optical image of the 6 μm and 10 μm bead phantom. 6 μm and 10 μm diameter polystyrene beads (Polysciences, Inc., 2.5% solid) were packed into its own 500 μL microcentrifuge tube using a centrifuge. An additional sample tube was filled with only water and used as a control region (not shown). To distinguish between the two beads samples, a 2 cm piece of capillary tubing was filled with CuSO_4 was fixed to the 6 μm bead sample. The entire sample was taped together in place before being placed into the coil. The polystyrene beads contained no water so no “intracellular” water was included in the model. (b) MR image showing the image slice used in the experiment. A 5 mm thick slice was taken to include the 6 and 10 μm bead samples and the water sample, and the capillary tube. (c) MR image of the cross section taken for the experiment [1].

5.1.1.3 Microcapillary Tubing

Capillary tubing (Polymicro Technologies/ Molex Inc., Phoenix, AZ) was used having inner and outer diameters of 5 μm and 151 μm , respectively. The microcapillary tubing was filled with

filtered water, injected using a modified syringe [16]. Tubing was cut into 2 cm pieces (1341 in total), and then packed into a sample tube, which was a 500 μL plastic microcentrifuge tube (Cole-Parmer Canada, Montreal QC).

The tubes themselves were meant to model axons while the space between the tubes was meant to model the extracellular compartment. The volume of water within each of the tubes was not large enough to produce a measurable signal and thus we concluded no “intracellular” water would contribute to the measured signal, as previously mentioned in Section 4.3.1.2.

The tubes were instead soaked in filtered water before being placed into a bird cage RF coil in order to create extracellular water from which the signal could be measured. Two additional 750 μm inner diameter tubes filled with filtered water were placed near the sample tube and used as a control. An optical image of the tube phantom is shown in Figure 5.3a.

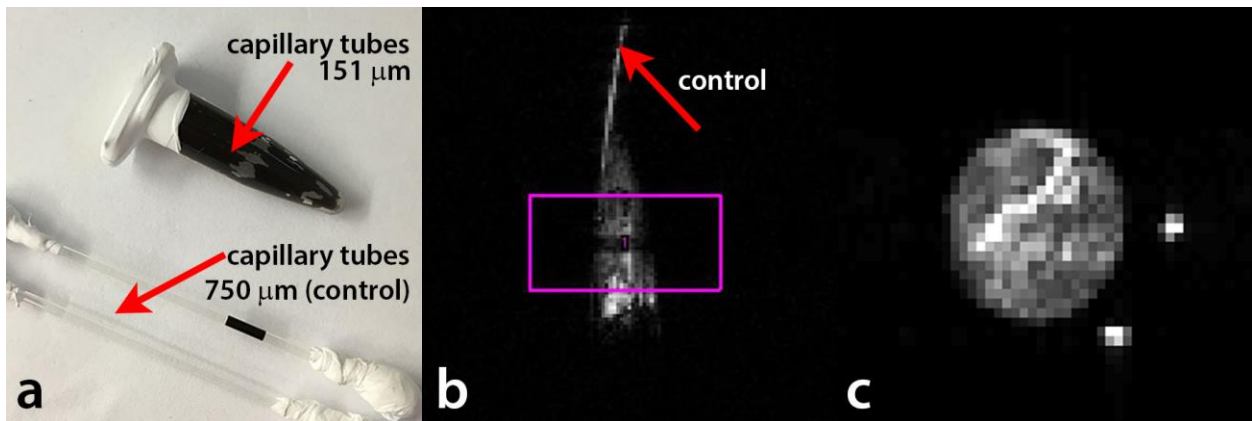


Figure 5.3: Tube phantom. (a) Optical image of the tube phantom. 2 cm pieces of capillary tubing (ID 5 μm , OD 151 μm) was cut packed into a sample tube (1341 in total). Tubes were soaked with water, and two additional capillary tubes (ID 750 μm) were filled alongside the sample tube to serve as a control. All were taped together and put at a slight angle to fit into the RF coil (not shown). (b) MR image showing the image slice used in the experiment. A 10 mm thick slice was taken to include the packed 151 μm capillary tubing sample and the two 750 μm tubes used as a control. (c) MR image of the cross section taken for the experiment [1].

5.1.2 MRI Parameters

Experiments were performed using a 7 T Bruker Avance III NMR system with Paravision 5.0, a BGA6 gradient set with maximum gradient strength, g_{max} , of 1.01 T/m (or 430357 Hz/cm), and a 3.5 cm diameter bird cage RF coil (Bruker Biospin, Milton, ON). A schematic of the magnet, gradient set, and RF coil configuration can be found in Appendix A.1. The apodised cosine sequence used for all experiments in this chapter is described in Section 3.5.3. The specific parameters for each phantom are described in this subsection, and are also presented in tables found in Appendix B.1.1 and B.1.3.

5.1.2.1 3 μm Bead Phantom Parameters

The images obtained for the 3 μm bead phantom were the same as those mentioned in Section 4.1.2.1 and thus used the same MRI parameters and slice selection as shown in Figure 4.2b.

5.1.2.2 6 and 10 μm Bead Phantom Parameters

One slice was chosen at 5 mm thick, $(2.56 \text{ cm})^2$ in-plane FOV, with a 64×64 matrix which was used for 800 μm in-plane resolution. This slice was chosen to contain a region of both the packed beads, and the water tube as shown in the MR image of Figure 5.2b. The number of sinusoidal waves in each 20 ms apodised cosine [11, 12] gradient pulse ranged from $n = 1$ to 20, in steps of 1 corresponding to frequencies of $n/20\text{ms}$ or 50 Hz to 1 kHz. Five gradient strengths were used for each frequency and the gradient pulses were separated by 24.52 ms (Appendix

B.1.1). Other parameters were TE = 50 ms, TR = 1250 ms, NA = 2, with an acquisition time per scan of 6.67 minutes.

In comparison to the first experiment on the 3 μm beads, this experiment used a larger slice thickness with a lower in-plane resolution. Therefore only one set of images, as described above, was collected. Another set of images with n=15 to 20 in steps of 1 were collected. In total all of the signals from all 26 scans and their respective frequencies were used in the fit. The extra set of higher numbers of sinusoidal waves was added because the b-values, due to the oscillating gradients with higher frequencies, were smaller than those due to the oscillating gradients with lower frequencies, which resulted in larger uncertainties in the measurements at higher frequencies. In total, 130 images were collected, with a total imaging time for this experiment of 3.03 hours.

5.1.2.3 Tube Phantom Parameters

One slice at 10 mm thick, $(2.0 \text{ cm})^2$ in-plane FOV, with a 64×64 matrix was used for 312.5 μm in-plane resolution. The chosen slice was perpendicular to the tubes as shown in the MR image of Figure 5.3b. Other parameters were TE = 89.066 ms, TR = 1250 ms, NA = 4, with acquisition time of 26.67 minutes per scan.

The number of sinusoidal waves in each 40 ms apodised cosine [11, 12] gradient pulse ranged from n = 1 to 20, in steps of 1 corresponding to frequencies of n/40ms or 25 Hz to 500 Hz. Five gradient strengths were used for each frequency and the gradient pulses were separated by 44.52 ms (Appendix B.1.3). The b-values from the oscillating gradient pulses were 0, 60, 120,

180, 240 s/mm². In total, 9 sets of images were obtained collecting a total of 900 images, with a total imaging time of ~ 81 hours.

5.1.3 Image Registration

Image registration was used in these data sets obtained for all the bead and tube phantoms, as previously described in Chapter 4 (Section 4.1.3). The 3 μ m bead sample tube could not fit completely vertical within the RF coil and was therefore placed at a slight angle. This caused the bead solution to slide very slowly throughout the experiment. As the sample tube rotated from vertical toward the horizontal, the border between the beads and water shifted. Due to the length of time to collect the large number of images for each experiment, the shift in the beads was apparent, so image registration was required. The image registration was also used to correct for the Larmor frequency drift which resulted in a shift of approximately one-ninth of a voxel from the start to the end of the experiment. For the other samples, we registered our images for consistency, although the total Larmor frequency drift was very small (less than 1/9th of a voxel, 43 Hz/5 days or 0.358 Hz/hour) and to account for motion of the sample.

5.1.4 Image Analysis

Regions of interest (ROIs) were arbitrarily drawn in the images as described below. For all the phantoms used in the experiments, the mean \pm standard deviation was calculated for the signals in the ROIs. This information was then used in the fits explained in Section 4.1.5. Caution was

used when drawing the ROIs for the noise to ensure the ROI was placed outside of any region containing artefacts such as ghosting.

5.1.4.1 3 μm Bead Phantom Analysis

The 3 μm bead images were analyzed as described in Section 4.1.4.1, however this time the signals obtained from the larger ROIs were used instead, as shown in the MR image of Figure 5.4. The signals used for the fits were taken from the ROI contained within the bead region as described in Sections 4.1.5 and 5.1.5.

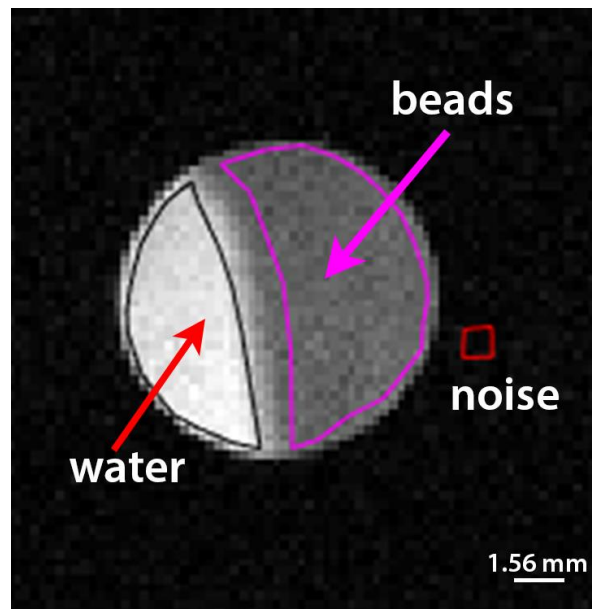


Figure 5.4: Larger ROIs were drawn in the water region of the bead sample (black ROI), in the bead region of the bead sample (magenta ROI), and in the noise (red ROI). The signal used in the fits was from the bead region. The signal from the water region was used as a control to ensure the measured diffusion coefficient was constant throughout the experiment and as the free diffusion coefficient used in the model [1].

5.1.4.2 6 and 10 μm Bead Phantom Analysis

ROIs were created for the 10 μm beads sample (ROI 1) and 6 μm beads sample (ROI 2), the water sample (ROI 3), and the noise (ROI 4), as shown in the MR image of Figure 5.2c. ROI 5 was the capillary tube that was filled with CuSO_4 , which was used primarily used to distinguish between the two bead samples and therefore not used in analysis. The signals that were used for the fits were taken from the ROI contained within the bead regions as described in Section 4.1.5. The signals from the water regions were used as a control to ensure the measured diffusion coefficient was constant throughout the experiment and as the free diffusion coefficient used in the model.

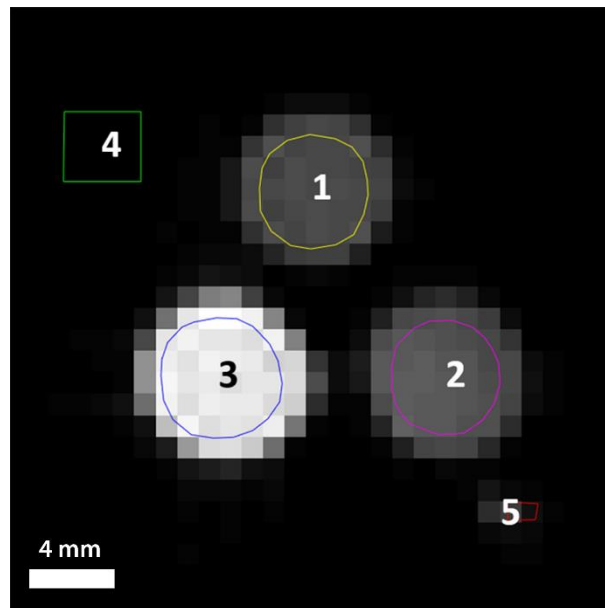


Figure 5.5: ROIs were created for each of the two beads samples (ROIs 1 and 2), the water sample (ROI 3), and the noise (ROI 4). ROI 5 (capillary tube) was not used in analysis and only served to distinguish between the two bead samples. The signals obtained from the ROIs were used in the fits was from the tube region. The signal from the water region was used as a control to ensure the measured diffusion coefficient was constant throughout the experiment and as the free diffusion coefficient used in the model [1].

5.1.4.3 Tube Phantom Analysis

ROIs were arbitrarily drawn within the sample tube (ROIs 1-10), in one of the 750 μm water capillary tubes (ROI 11), and in the noise (ROI 12), as shown in the MR image of Figure 5.3c. Again the signals used in the fits came from the ROIs in the sample tube. The signal from the water region was used as a control to ensure the measured diffusion coefficient was constant throughout the experiment.

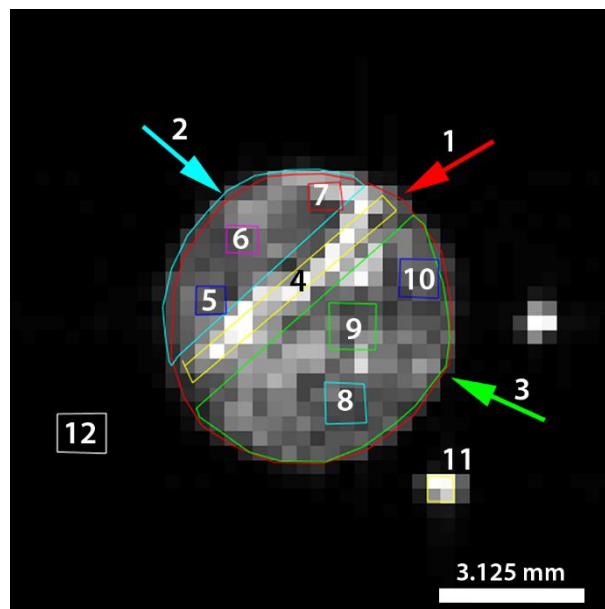


Figure 5.6: ROIs were created within the tube sample (ROIs 1-10), in one of the 750 μm water capillary tube (ROI 11), and in the noise (ROI 12). The signals used in the fits came from ROIs 6, 7 and 10. Signal from the water region from ROI 11 was used as a control to ensure the measured diffusion coefficient was constant throughout the experiment [1]

5.1.5 Signal Extraction and Fit

Regions of interest (ROIs) were drawn in the images described in Sections 5.1.4.1 - 5.1.4.3. For all the phantoms used in the experiment, the mean \pm standard deviation (SD) was calculated of all the signals extracted from all the voxels contained within the ROIs. These signals were fitted with Equation (3.48) to obtain the ADC in each voxel as a function of frequency. Using Equation (3.48), the log of the signal versus b-value from the oscillating gradients was fitted to a straight line and the negative of the slope was used as the ADC for each measurement for the water ROIs. The mean and standard deviation of the other ROIs for each sample were used in the analytical equations to fit the geometry as discussed in Section 3.5.4 for the beads, and Section 3.5.5 for the tubes. Section 4.1.5 also explains how the signals were extracted and used in the fits to determine bead and cylinder diameters for the experiments.

5.1.5.1 Bead Phantoms fit

Signal data were fitted by the model with nonlinear least-squares regression using the Optimization Toolbox in Matlab (Mathworks, Natick, MA). The long-time diffusion coefficient was constrained to the range $[0, 2] \mu\text{m}^2/\text{ms}$. The diffusion coefficient of free water at room temperature is $2 \mu\text{m}^2/\text{ms}$. The long-time diffusion coefficient is smaller than the free diffusion coefficient. Thus values of long-time diffusion coefficients greater than $2 \mu\text{m}^2/\text{ms}$ were not physical possibilities. The pore radius was constrained to the range $[0, 5] \mu\text{m}$ because it was expected to be no larger than the bead radius.

5.1.5.2 Tube Phantom Fit

Signal data were fitted by the model with nonlinear least-squares regression using the Optimization Toolbox in Matlab (Mathworks, Natick, MA). The diffusion coefficient was constrained to the range $[0, 3] \mu\text{m}^2/\text{ms}$. The surface-to-volume ratio (S/V) was constrained to the range $[0, 0.2] \mu\text{m}^{-1}$ for similar reasons as the beads.

5.2 Results

The results from all samples are explained in this section. Once again plots of the apparent diffusion coefficient vs OGSE frequency are presented. The parameters inferred from the fits, such as pore radii, surface-to-volume ratios, and diffusion coefficients are presented. The corresponding bead radii and tube diameters are also given. The inferred pore radii from all three samples are plotted against the actual bead radius to compare the results of the method at different frequencies.

5.2.1 Beads Phantom Results

For the first bead experiment, using the 900 images similar to the one shown in Figure 4.2c, signals were extracted from each ROI and fitted with Equation (3.48) to obtain the ADC in each voxel as a function of frequency. ADC versus frequency is plotted for the $3 \mu\text{m}$ beads (Figure 5.7a). The fit was obtained using Equation (3.44) (Section 3.5.4) and is shown with the dashed

line in Figure 5.4. The pore radius was inferred to be $0.60 \pm 0.08 \mu\text{m}$ with long-time diffusion coefficient $1.38 \pm 0.02 \mu\text{m}^2/\text{ms}$. The corresponding bead diameters for the measured pore size are $2.9 \pm 0.4 \mu\text{m}$ to $5.3 \pm 0.7 \mu\text{m}$, depending on the type of pore.

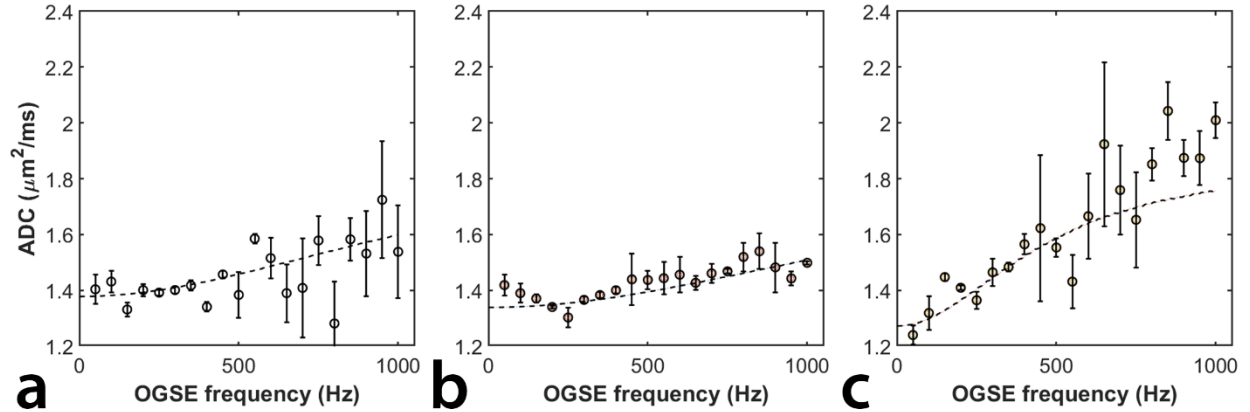


Figure 5.7: The diffusion spectrum for the bead sample. ADC of water surrounding the beads is plotted versus frequency for the $3 \mu\text{m}$ beads (a), $6 \mu\text{m}$ beads (b) and $10 \mu\text{m}$ beads (c). The fit is shown with the dashed line. Data points are mean \pm standard deviation of the ADC for each frequency. The inferred pore radius and long-time diffusion coefficients for each of the beads are outlined in Table 5.1. Measurements made at higher frequencies used smaller OGSE b-values compared to those made at lower frequencies. Thus the amount of signal decay between the measurement with the lowest and highest OGSE b-value was smaller at higher frequencies. The standard deviation in measurements at higher frequencies increases because of the smaller signal decay. Clearly, the ADC shows frequency dependence in all samples [1].

For the second bead experiment, using the 130 images similar to the one shown in Figure 5.3c, signals were extracted from each ROI and fitted by Equation (3.48) to obtain the ADC in each voxel as a function of frequency. Here, the ADC versus frequency is plotted, with the fit shown as the dashed line in Figure 5.7 (b,c). For the $6 \mu\text{m}$ beads, the pore radius was inferred to be $0.54 \pm 0.06 \mu\text{m}$, with a long-time diffusion coefficient of $1.34 \pm 0.02 \mu\text{m}^2/\text{ms}$. For the $10 \mu\text{m}$ beads, the pore radius was inferred to be $1.0 \pm 0.1 \mu\text{m}$, with a long-time diffusion coefficient of $1.27 \pm 0.06 \mu\text{m}^2/\text{ms}$.

The corresponding bead diameters for the measured pore size are $2.6 \pm 0.3 \mu\text{m}$ to $4.8 \pm 0.6 \mu\text{m}$, and $4.9 \pm 0.7 \mu\text{m}$ to $9 \pm 1 \mu\text{m}$, for the 6 and 10 μm beads respectively.

The diffusion coefficients in the water ROIs of the two bead experiments remained fairly constant throughout image acquisition with an average of $2.0 \pm 0.1 \mu\text{m}^2/\text{ms}$ for the first experiment, and of $1.97 \pm 0.06 \mu\text{m}^2/\text{ms}$ for the second experiment. This is likely due to a change in temperature of the sample of less than one degree Kelvin [17]. The results from the fits for all bead experiments are summarized in Table 5.1.

Table 5.1: Beads. Inferred pore radius, long time diffusion coefficients and corresponding bead diameters. The inferred pore radii and long-time diffusion coefficients from the fits are listed for each of the three bead samples. The resulting bead diameters based on pore radii for two different types of pores are also listed.

Actual Bead Diameter (μm)	Pore radius (μm) r_{pore}	Bead diameter (μm) Octahedral holes $d_{bead} = \frac{2 \cdot r_{pore}}{0.414}$	Bead diameter (μm) Tetrahedral holes $d_{bead} = \frac{2 \cdot r_{pore}}{0.225}$	Long-time diffusion coefficient ($\mu\text{m}^2/\text{ms}$)
3	0.60 ± 0.08	2.9 ± 0.4	5.3 ± 0.7	1.38 ± 0.02
6	0.54 ± 0.06	2.6 ± 0.3	4.8 ± 0.6	1.34 ± 0.02
10	1.0 ± 0.1	4.9 ± 0.7	9 ± 1	1.27 ± 0.06

During the 72 hours used to collect the bead data in the first experiment, the image rotated 27 degrees from the first to the final image. Over time, the boundary between the beads and water drifted because the sample was not completely vertical and the sample rotated slowly. Over the 3.03 hour period used to collect the bead data in the second experiment, the image shifted 1.2 voxels from the first to final image. The shift began to occur after the n=9 image. For the tubes experiment, the tube sample shifted less than 1 voxel (0.9 voxels) during the 81 hours of data collection.

The inferred pore radii for all the bead samples are plotted against the known bead radius in Figure 5.8. In square packed lattices the relationship between the pore radius and bead radius is linear. A linear fit to the data is also shown in Figure 5.8. The slope of the fitted line is 0.08 ± 0.04 which agrees well with 0.084, the slope of the best fit line from another study [4]. The inferred pore radius for the 3 μm and 6 μm diameter beads was very similar whereas the pore radius for the 10 μm diameter beads could be distinguished from the other two bead samples. This suggests that the resolution limit for pore radius for this method with these gradient frequencies and strengths is between 0.5 μm and 1 μm .

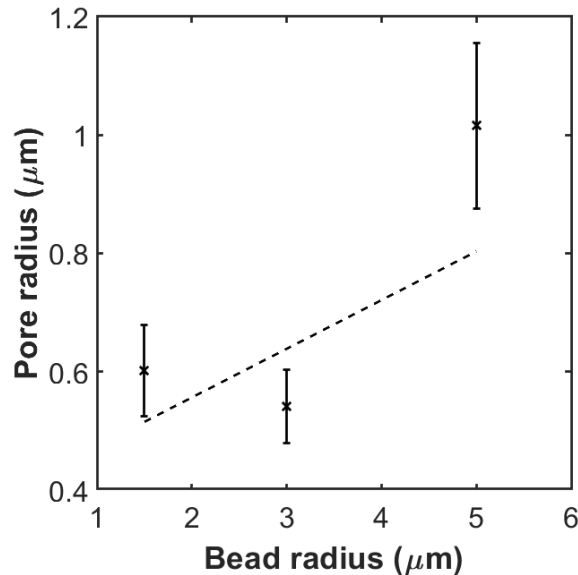


Figure 5.8: Pore radius vs bead radius. A linear relationship between the pore and bead radii should exist with tightly packed beads. This plot shows the inferred radius vs the actual bead radius. The fitted line is the best fit from a linear least squared fit, with the slope of 0.08 ± 0.04 which agrees well with 0.084, the slope of the best fit line from another study [4]. The inferred pore radius for both the 3 μm and 6 μm diameter beads were similar in comparison, whereas the 10 μm diameter beads could be distinguished from the other two bead samples. This suggests that the resolution limit for pore radius for this method with these gradient frequencies and strengths is between 0.5 μm and 1 μm [1].

5.2.2 Tube Phantom Results

Using the 900 images similar to the one shown in Figure 5.3c, signals were extracted from each ROI and fitted by Equation (3.48) to obtain the ADC in each voxel as a function of frequency. ADC versus frequency plotted for ROI 6, ROI 7, and ROI 10 and the fit shown by the dashed line (Figure 5.9).

Figure 5.6 shows the difference in contrast in the ROIs within the sample tube which is likely due to the differences in packing of the tubes as well as the possible orientation dispersion of the tubes. Thus it is very important to know the spatial variation in the packing fraction of tubes in the sample. A total of 1341 capillary tubes with diameter 151 μm fit inside the 6.56 mm diameter microcentrifuge tube. Thus the average packing fraction of $[1341 \cdot \pi \cdot (0.151)^2 / \pi \cdot (6.56)^2] \times 100 = 71.05\%$ was used to relate the inferred surface-to-volume ratio of the tube sample to the diameter of the capillary tubes.

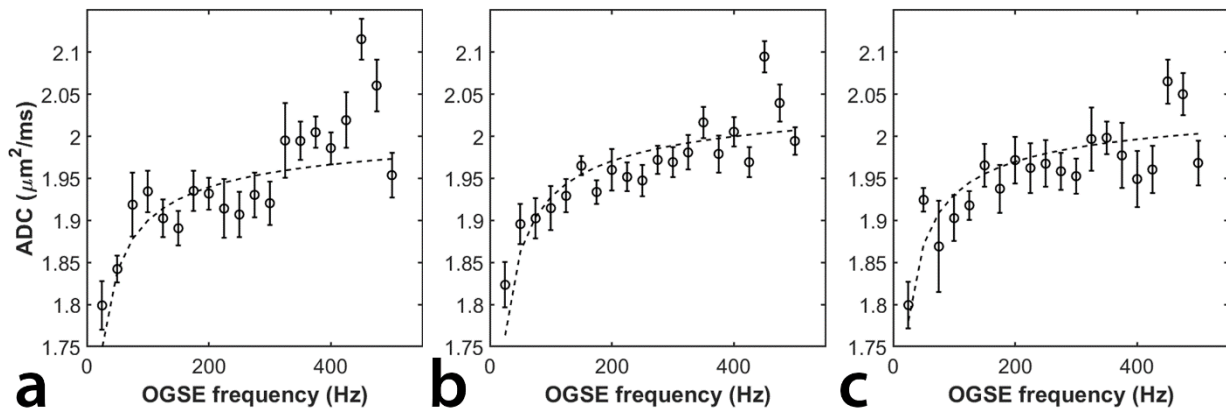


Figure 5.9: The diffusion spectrum for the tube sample. ADC of water surrounding the tubes is plotted versus frequency for ROI 6 (a), ROI 7 (b), and ROI 10 (c). The fit is shown with the dashed line. Data points are mean \pm standard deviation of the ADC for each frequency. Table 5.2 outlines the following for the ROIs within the tube sample: inferred surface-to-volume ratios of the spaces between the tubes, and their corresponding tube diameters assuming 71.05% hexagonal packing, as well as the diffusion. The data show similar trends in all ROIs with ADC increasing with frequency. Clearly the ADC is frequency dependent [1].

The inferred surface-to-volume ratios and the corresponding bead diameter as well as the apparent diffusion coefficient of water in the pores in each of the ROIs can be found in Table 5.2. The average surface-to-volume ratio over all the ROIs was $0.06 \pm 0.02 \mu\text{m}^{-1}$. The average tube diameter over all ROIs was $180 \pm 70 \mu\text{m}$. The average intrinsic diffusion coefficient over all ROIs was $2.02 \pm 0.03 \mu\text{m}^2/\text{ms}$.

Table 5.2: Tubes. Inferred surface-to-volume ratios (S/V), tube diameters, and diffusion coefficients of water. The inferred S/V and the apparent diffusion coefficient of water in the pores in each of the ROIs. Corresponding bead diameters were obtained from the S/V of each of the ROIs, assuming 71.05% hexagonal packing.

ROI #	S/V (μm^{-1})	Tube diameter (μm)	Diffusion coefficient, D ($\mu\text{m}^2/\text{ms}$)
1	0.051 ± 0.004	192 ± 17	2.010 ± 0.006
2	0.068 ± 0.009	145 ± 20	2.03 ± 0.01
3	0.041 ± 0.007	239 ± 38	2.01 ± 0.01
4	0.05 ± 0.01	182 ± 34	1.98 ± 0.01
5	0.04 ± 0.02	261 ± 128	1.97 ± 0.02
6	0.10 ± 0.01	103 ± 15	2.03 ± 0.01
7	0.101 ± 0.009	98 ± 9	2.07 ± 0.01
8	0.03 ± 0.01	281 ± 83	1.98 ± 0.01
9	0.05 ± 0.01	183 ± 39	2.05 ± 0.01
10	0.09 ± 0.01	106 ± 17	2.06 ± 0.01

5.3 Discussion

A previous study investigated using OGSE and diffusion spectroscopy to infer the inner diameter of similar tubes [18]. Our simulation data indicated extracellular water was being modeled incorrectly for our data because of the choice of diffusion frequencies [2]. Here we presented three experiments, two with beads (spheres) and one with tubes (cylinders) with only extracellular water in order to test the model with our limited range of frequencies. In the case of the beads, the fitted value of bead diameter was consistent with the diameter of the beads themselves but could not distinguish the 3 μm beads from the 6 μm beads. In the case of the cylinders, the fitted value of the tube diameter was larger than the tube diameter but still within one standard deviation. This could be due to the choice in the range of frequencies that were used. The frequency range being studied was targeted for objects the size of the inner diameter of the tubes and not the outer diameter. Unfortunately tubes with outer diameters in the micron-sized range were unavailable at the time of the experiments. Nonetheless, data were still consistent and they suggest that both the upper limit and lower limit of the OGSE frequencies should be chosen carefully based on the extracellular size.

The percent uncertainty in the bead diameter measurements is 13% for the 3 μm beads, 11% for the 6 μm beads and 14% for the 10 μm . The percent error in the bead diameters is 3.1% to 78% for the 3 μm beads, 20% to 57% for the 6 μm beads and 10% to 51% for the 10 μm beads.

At the gradient strengths and oscillating frequencies used for these experiments, the resolution limit of the radii for this method is between 0.54 μm and 1 μm . This is because the size of the pores in the sample with the 3 μm beads could not be distinguished from the size of the pores in the sample with the 6 μm beads, whereas the size of the pores in the 10 μm bead sample could be

distinguished from the other two samples. Higher gradient strengths or oscillating gradient frequencies need to be used to decrease this resolution limit.

The percent uncertainty in the 10 μm beads was larger than the 6 μm beads even though data from the two samples were in the same images. We believe this is because the water within the pores of the 10 μm beads could diffuse farther than in the pores of the 6 μm beads which would cause more signal decay in the voxels for the 10 μm beads than the voxels in the 6 μm beads. This would result in lower signal-to-noise ratio (SNR) in the area of the image containing the 10 μm bead sample than the area containing the 6 μm bead sample. Figure 5.10 shows the difference in the SNR between the 6 μm and 10 μm beads. Lower SNR shows up darker in the 10 μm bead sample.

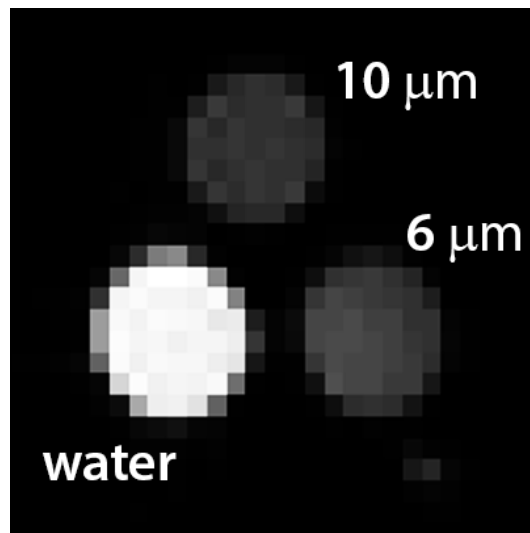


Figure 5.10: MR image of the water, 6 μm and 10 μm bead samples. The 10 μm bead samples appears darker in this MR image in comparison to the 6 μm beads, which indicates a lower SNR for the 10 μm bead samples.

The data in Figure 5.8 do not appear completely linear although the slope of the best fit line matches well with a previous study which also did not produce a robust linear relationship [4]. As with this previous study, this is likely due to the resolution limit. The finite intercept is also likely due to loosely packed beads and/or the resolution limit.

The diameter of the tubes depends on the packing fraction. Thus it is necessary to know the packing fraction of the tubes in the sample. For measurements in the central nervous system (CNS), it will be necessary to map axon diameter densities to infer axon diameters in white matter tracts. These densities vary throughout the CNS and between species of animals [19, 20]. Therefore, electron microscopy studies should be done in parallel to temporal diffusion spectroscopy as the methods are developed.

The current study collected many images (800 for the 3 μm beads, 130 for the 6 μm and 10 μm beads and 900 for the tubes). That many images required a long time to collect (72 hours for the 3 μm beads, 3.03 hours for the 6 μm and 10 μm beads and 81 hours for the tubes). The method, as followed using the parameters described in this thesis, is not clinically feasible because imaging sessions need to be short for patient comfort and economical use of the MRI time. Future studies could include investigating reducing the number of gradient strengths and oscillating gradient frequencies used to optimize the data collection time, similar to the simulation work done in the Martin lab [21]. Measurements could be made on brain tissue samples using the reduced range of frequencies suggested in our previous work [2] and tested here.

White matter tissue is composed largely of myelinated axons, and glial cells. The phantoms used in this study are meant to model only one aspect of white matter. The tubes and beads, which modelled axons and cells respectively, did not contain water, so our model had only the

“extracellular” water. Thus this study targeted only one aspect of white matter models and phantoms. Future studies will need to focus on more accurate models that will include intracellular water, exchange between compartments, axon orientation dispersion, and axon and cell diameter distributions, to name only a few properties. Nonetheless, this study does show that it is possible to model the extracellular water apparent diffusion coefficient as hindered and not constant or linear with frequency. The more complex model for the extracellular water diffusion, which allows the diffusion coefficient to vary non-linearly with frequency, provided geometrical results consistent with the phantoms. More measurements will be required when this model of the extracellular water is added to the full model, which includes intracellular water diffusion because of the extra complexity and extra parameters. Therefore a careful study is needed to determine whether this more complex model provides sufficiently better results to necessitate the extra imaging time.

Models of white matter tissue are more complex than the geometric models used in the phantoms presented here which consists of beads and tubes. In principle, the more complicated the model, the more precise the results. Because model parameters need to be constrained, more complicated models worsen the ability to infer the smaller axon diameters. Others have tested complicated models which more accurately reflect tissue, such as allowing exchange between compartments [22-24]. White matter angular orientation dispersion [22, 25, 26], and axonal undulation [22, 27], have also been studied. Future experiments and phantoms could examine these more complicated models using OGSE to develop models more closely related to tissue. This study was designed to test another model of the extracellular water diffusion. As such, bead and capillary tube phantoms were used because they allowed for water only in the “extracellular” compartments. When the full model is tested, more complex phantoms will be needed.

5.4 Conclusion

Restricting frequency ranges so that the extracellular water diffusion can be modelled as constant allows for the inferences of structure diameters on the micron-scale. The pore radius between the 3, 6 and 10 μm beads were $0.60 \pm 0.08 \mu\text{m}$, $0.54 \pm 0.06 \mu\text{m}$, and $1.0 \pm 0.1 \mu\text{m}$ respectively, with corresponding long-time diffusion coefficients of $1.38 \pm 0.02 \mu\text{m}^2/\text{ms}$, $1.32 \pm 0.02 \mu\text{m}^2/\text{ms}$ and $1.27 \pm 0.06 \mu\text{m}^2/\text{ms}$. These correspond to bead diameters ranging from $2.9 \pm 0.4 \mu\text{m}$ to $5.3 \pm 0.7 \mu\text{m}$ for the 3 μm beads, $2.6 \pm 0.3 \mu\text{m}$ to $4.8 \pm 0.6 \mu\text{m}$, for the 6 μm beads, and $4.9 \pm 0.7 \mu\text{m}$ to $9 \pm 1 \mu\text{m}$ for the 10 μm beads. The surface-to-volume ratio of the 151 μm diameter tubes was inferred to be $0.06 \pm 0.02 \mu\text{m}^{-1}$, containing water diffusing at $2.02 \pm 0.03 \mu\text{m}^2/\text{ms}$. This corresponds to a tube diameter of $180 \pm 70 \mu\text{m}$. The resolution limit for pore radius with this range was between 0.5 μm and 1 μm . Future experiments should also consider the extracellular size when choosing the upper and lower limits of the OGSE frequencies.

References

1. S. L. Herrera, M. Mercredi, R. Buist R, and M. Martin. “Inferring diameters of spheres and cylinders using interstitial water”. *Magnetic Resonance Materials in Physics, Biology and Medicine*. 2018. <https://doi.org/10.1007/s10334-018-0685-9>
2. M. Mercredi, T. J. Vincent, C. P. Bidinosti, and M. Martin, “Assessing the accuracy of using oscillating gradient spin echo sequences with AxCaliber to infer micron-sized axon diameters,” *Magnetic Resonance Materials in Physics, Biology and Medicine*, vol. 30, no. 1, pp. 1-14, Feb 2017.
3. J. Xu, H. Li, K. D. Harkins, X. Jiang, J. Xie, H. Kang, M. D. Does, “Mapping mean axon diameter and axonal volume fraction by MRI using temporal diffusion spectroscopy,” *NeuroImage*, vol. 103, pp. 10-19, Dec 2014.
4. E. C. Parsons, M. D. Does, and J. C. Gore, “Modified oscillating gradient pulses for direct sampling of the diffusion spectrum suitable for imaging sequences,” *Magnetic Resonance Imaging*, vol. 21, no. 3, pp. 279-285, 2003.
5. D. S. Novikov, V. G. Kiselev, and S. N. Jespersen, “On modeling,” *Magnetic Resonance in Medicine*, vol. 79, no. 6, pp. 3172-3193, 2018.
6. L. M. Burcaw, E. Fieremans, and D. S. Novikov, “Mesoscopic structure of neuronal tracts from time-dependent diffusion,” *NeuroImage*, vol. 114, pp. 18-37, 2015.
7. E. Fieremans, L. M. Burcaw, H.-H. Lee, G. Lemberskiy, J. Veraart, and D. S. Novikov, “In vivo observation and biophysical interpretation of time-dependent diffusion in human white matter,” *NeuroImage*, vol. 129, pp. 414-427, 2016.
8. H.-H. Lee, E. Fieremans, and D. S. Novikov, “What dominates the time dependence of diffusion transverse to axons: Intra-or extra-axonal water?” *NeuroImage*, 2017.
9. Y. Assaf, T. Blumenfeld-Katzir, Y. Yovel, and P. J. Basser, “AxCaliber: a method for measuring axon diameter distribution from diffusion MRI,” *Magnetic Resonance in Medicine*, vol. 59, no. 6, pp. 1347-1354, 2008.
10. D. C. Alexander, P. L. Hubbard, M. G. Hall, E. A. Moore, M. Ptito, G. J. M. Parker, T. B. Dyrby. “Orientationally invariant indices of axon diameter and density from diffusion MRI,” *NeuroImage*, vol. 52, no. 4, pp. 1374-1389, 2010.
11. M. Schachter, M. D. Does, A. W. Anderson, and J. C. Gore, “Measurements of restricted diffusion using an oscillating gradient spin-echo sequence,” *Journal of Magnetic Resonance*, vol. 147, no. 2, pp. 232-237, Dec 2000.
12. M. D. Does, E. C. Parsons, and J. C. Gore, “Oscillating gradient measurements of water diffusion in normal and globally ischemic rat brain,” *Magnetic Resonance in Medicine*, vol. 49, no. 2, pp. 206-215, Feb 2003.

13. E. C. Parsons, M. D. Does, and J. C. Gore, "Temporal diffusion spectroscopy: Theory and implementation in restricted systems using oscillating gradients," *Magnetic Resonance in Medicine*, vol. 55, no. 1, pp. 75-84, 2006.
14. O. Reynaud, K. V. Winters, D. M. Hoang, Y. Z. Wadghiri, D. S. Novikov, and S. G. Kim, "Surface-to-volume ratio mapping of tumor microstructure using oscillating gradient diffusion weighted imaging," *Magnetic Resonance in Medicine*, vol. 76, no. 1, pp. 237-247, Jul 2016.
15. A. L. Sukstanskii, "Exact analytical results for ADC with oscillating diffusion sensitizing gradients," *Journal of Magnetic Resonance*, vol. 234, pp. 135-140, 2013.
16. D. B. Craig, "A simple system for the measurement of the distribution of activities of individual molecules of E. coli β -galactosidase," *Analytical Methods*, vol. 4, no. 1, pp. 85-88, 2012.
17. M. Holz, S. R. Heil, and A. Sacco, "Temperature-dependent self-diffusion coefficients of water and six selected molecular liquids for calibration in accurate ^1H NMR PFG measurements," *Physical Chemistry Chemical Physics*, vol. 2, no. 20, pp. 4740-4742, 2000.
18. H. Li, J. C. Gore, and J. Xu, "Fast and robust measurement of microstructural dimensions using temporal diffusion spectroscopy," *Journal of Magnetic Resonance*, vol. 242, pp. 4-9, 2014.
19. ScienceDirect, Elsevier B.V. (2018) *Packing Density* [Online]. Available: <https://www.sciencedirect.com/topics/agricultural-and-biological-sciences/packing-density>.
20. Y. Assaf and Y. Cohen, "Chapter 9 - Inferring Microstructural Information of White Matter from Diffusion MRI," in *Diffusion MRI* (2nd ed.). Elsevier, Inc. 2014, pp. 185-208.
21. M. Mercredi and M. Martin, "Toward faster inference of micron-scale axon diameters using Monte Carlo simulations," *Magnetic Resonance Materials in Physics, Biology and Medicine*, pp. 1-20, 2018. <https://doi.org/10.1007/s10334-018-0680-1>
22. M. Nilsson, D. van Westen, F. Ståhlberg, P. C. Sundgren, and J. Lätt, "The role of tissue microstructure and water exchange in biophysical modelling of diffusion in white matter," *Magnetic Resonance Materials in Physics, Biology and Medicine*, vol. 26, no. 4, pp. 345-370, 2013.
23. M. Nilsson, J. Lätt, E. Nordh, R. Wirestam, F. Ståhlberg, and S. Brockstedt, "On the effects of a varied diffusion time in vivo: is the diffusion in white matter restricted?" *Magnetic Resonance Imaging*, vol. 27, no. 2, pp. 176-187, 2009.
24. M. Nilsson, E. Alerstam, R. Wirestam, F. Sta, S. Brockstedt, and J. Lätt, "Evaluating the accuracy and precision of a two-compartment Kärger model using Monte Carlo simulations," *Journal of Magnetic Resonance*, vol. 206, no. 1, pp. 59-67, 2010.
25. H. Zhang, D. Barazany, Y. Assaf, H. Lundell, D. Alexander, and T. Dyrby, "A comparative study of axon diameter imaging techniques using diffusion MRI" in *ISMRM*, Montreal, QC, 2011.

26. L. Avram, Y. Assaf, and Y. Cohen, "The effect of rotational angle and experimental parameters on the diffraction patterns and micro-structural information obtained from q-space diffusion NMR: implication for diffusion in white matter fibers," *Journal of Magnetic Resonance*, vol. 169, no. 1, pp. 30-38, 2004.
27. M. Nilsson, J. Lätt, F. Ståhlberg, D. Westen, and H. Hagslätt, "The importance of axonal undulation in diffusion MR measurements: a Monte Carlo simulation study," *NMR in Biomedicine*, vol. 25, no. 5, pp. 795-805, 2012.

Chapter 6

Axon Diameter Measurements in the Human Corpus

Callosum using Oscillating Gradient Spin Echo

Sequences

6.1 Background

This thesis developed experimental verification of the ability of oscillating gradient spin echo (OGSE) sequences to infer smaller (micron-scale) restriction sizes in samples. The ultimate goal of this project was to be able to infer micron-sized axon diameters in live brains. In this chapter the first measurements on human brain are presented. The experiments produced results that indicated the ability of this method to infer smaller axons than other methods and also indicated areas of improvements that are necessary in order to apply this method to live brains. To our knowledge, at the time the data were collected, this was the first study using OG for inferences of human axon diameters.

The brain is divided into two hemispheres which are connected by a thick bundle of nerve fibres called the corpus callosum that acts as a neural bridge by ensuring both sides of the brain can communicate and send signals to each other. The corpus callosum, located in the white matter of the cerebrum, the largest white matter structure in the brain, is approximately 10 cm long at the midline, with 200-250 million axons (nerve fibres) in the average corpus callosum [1]. Damage to the corpus callosum causes the brain's hemispheres to not be able to communicate properly

causing a loss of a range of functions to occur, such as changes in speech, visual perception, and memory [1-4].

The experiment presented in this chapter used the standard ActiveAx [5] and AxCaliber [6] methods with OGSE. Although previous experiments indicated that the model for extra-axonal water breaks down in these standard models [7]. The experiments presented in this chapter have the extra-axonal water modelled incorrectly as a constant. The phantoms used in the experiments of Chapters 4 and 5 was used to test the OGSE method in this more simple form. When this method is optimized further, more imaging time can be devoted to collecting data with more frequencies and gradient strengths to include a more complicated model of the extra-axonal water diffusion.

This experiment tested the basic model on brain tissue using the standard ActiveAx and AxCaliber methods by switching from the PGSE to OGSE sequences. This experiment helped determine if the parameters used were sufficient for measurements of micron-sized axons. Comparing the MR results to histology was used to determine if the means of preparing and imaging the sample, as well as the electron microscopy (EM) methods used were appropriate, and if any improvements would be required for any of these methods. The results from this experiment was used to determine if axonal orientation dispersion could be important to be modeled, and if the model might produce acceptable results in the regions other than axons such as those studied in this chapter (ependymal layer and cortex).

6.2 Methods

This section describes the human brain sample that was imaged. The imaging sequences and parameters used to collect the data and the analysis methods used to infer the axon diameters are described. The fits to the data to infer axon diameters are explained. Finally the histological methods to verify the results are explained. The procedure for this experiment is summarized in an outline shown in Figure 6.1.

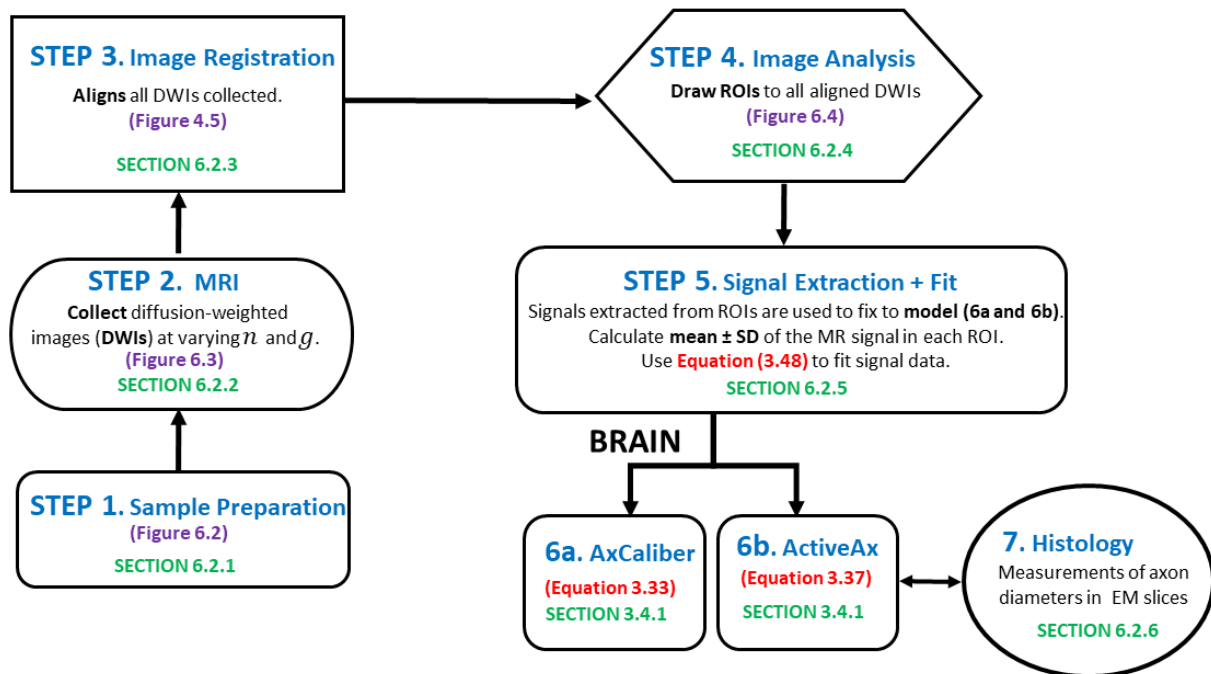


Figure 6.1: General outline of methods used for the experiment.

6.2.1 Tissue Sample Preparation

A portion of the corpus callosum from an autopsy of human brain was collected, under the protocol approved by the institutional health research ethics board along with the consent obtained from the family members. This portion of the corpus callosum did not demonstrate any pathological changes and was kept in formalin for approximately 10-14 days before being prepared for imaging. An optical image of the portion of the human corpus callosum is shown in Figure 6.2. In the 24 hours before the MRI experiment, the formalin was replaced with phosphate-buffered saline (PBS). For imaging, the tissue was subsequently placed into a 15 mL sample tube filled with 2% w/v (weight/volume) agarose gel (Sigma-Aldrich, St. Louis, Missouri) to stabilize the tissue in the centre of the sample tube so that it could be aligned to the centre of the RF coil prior to imaging [8].



Figure 6.2: Human corpus callosum sample. Optical image of the portion of the human brain autopsy sample containing the corpus callosum was used in this experiment.

6.2.2 MRI Parameters

As with the other experiments presented in this thesis, the sample was imaged using a 7 T Bruker Avance III NMR system with Paravision 5.0 with a BGA6 gradient set with a maximum gradient strength of 430357 Hz/cm, and a 3.5 cm diameter bird cage RF coil. A schematic of the magnet, gradient set, and RF coil configuration can be found in Appendix A.1. The experiment used the sinusoidal oscillating gradient spin echo sequence [9, 10] (Section 3.5.2). The specific parameters for this experiment are described in this subsection, and are also presented in the table found in Appendix B.1.4.

One slice was chosen at 1 mm thick, $(2.56 \text{ cm})^2$ in-plane FOV, with a 128×128 matrix which used for 200 μm in-plane resolution. This slice was taken approximately perpendicular to the direction of the axons within the corpus callosum (CC). This slice also included regions of white matter and ependymal layer (EL) and cortex (CX) (Figure 6.3a,b, EL region not shown). Other pulse sequence parameters included TE = 89.066 ms, TR = 1250 ms, NA = 4, with an acquisition time per scan of 32 minutes.

The number of sinusoidal waves in each 20 ms sine gradient pulse ranged from $n = 1$ to 15, in steps of 1 corresponding to frequencies of $n/20$ ms or 50 Hz to 750 Hz. Each set consisted of 15 scans which corresponded to the number of sinusoidal waves of the gradient pulse. Six gradient strengths were used for each frequency and the gradient pulses were separated by 24.52 ms. For $n = 1$, the gradient strengths were (0, 99, 88, 76, 61 and 44) % of g_{max} , and for $n > 1$, the gradient strengths were (0, 50, 45, 39, 33 and 22)% of g_{max} . Appendix B.1.4 shows a table of these parameters. In total 14 sets of scans were obtained collecting a total of 1260 images (Figure 6.3c). Total imaging time was 112 hours or 4.67 days.

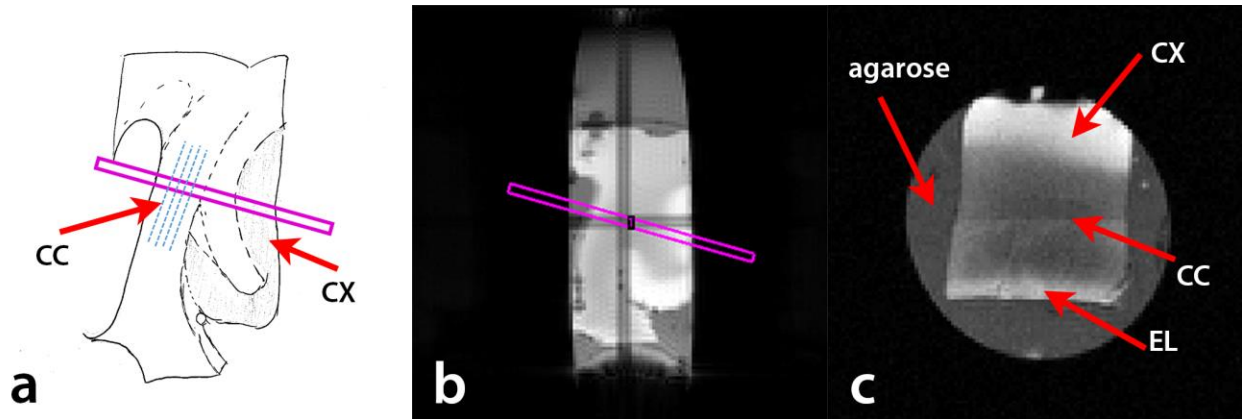


Figure 6.3. Human corpus callosum sample. (a) Drawing of the image slice taken for the experiment. The slice taken (magenta box) was selected to be approximately perpendicular to the direction of the axons (blue lines) within the corpus callosum. (b) MR image of the slice taken from scanner to contain the corpus callosum (CC), endymal layer (EL), and cortex (CX) regions. (c) MR image of the cross section taken from the MR slice from (b).

6.2.3 Image Registration

As with the images from the experiments discussed in Chapters 4 and 5, a custom-built image registration tool was used [11] to align all images to the $b=0$ diffusion-weighted images using a rigid affine transformation matrix determined automatically by maximizing the 2D correlation coefficient. Image registration, as was previously explained in Section 4.1.3, was used for consistency with the other experiments, and also to account for any shift in the sample that may have occurred during the days-long imaging session.

6.2.4 Image Analysis

Regions of interest (ROIs) were drawn in the corpus callosum, ependymal layer, and cortex, as well as within the agarose as shown in Figure 6.4. Using the 1260 images similar to the one shown in Figure 6.3, signals were extracted from each ROI and fitted with Equation (3.48) to obtain the ADC in each voxel as a function of frequency. The mean \pm standard deviation was calculated for the signals in the ROIs, which was then used in the fits as explained in Section 4.1.5. Caution was used when drawing the ROIs for the noise to ensure the ROI was placed outside of any region containing artefacts such as ghosting.

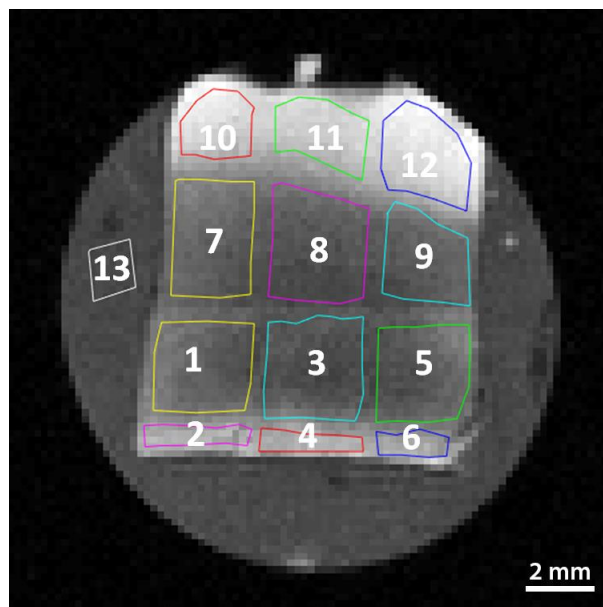


Figure 6.4: Regions of interest (ROIs) were drawn in the corpus callosum (1,3,5, 7-9), ependymal layer (2,4,6) and cortex (10-12) , as well as the agarose which was used as a control (13).

6.2.5 Signal Extraction and Fit

Signals were fitted using two models, a two compartment ActiveAx model [5] and AxCaliber model [6] described in Section 3.4, using least squares minimization, and the mean axon diameters were extracted. Again, it should be noted that these models assume that the extra-axonal apparent diffusion coefficient is constant with frequency. It has been shown that this assumption breaks down with the frequency range used in these experiments [7]. Chapter 4, and moreso in Chapter 5, described models which allowed the extra-axonal water to vary with frequency [12]. These models however were tested on phantoms containing only extra-axonal water. More work will be needed to add these frequency varying extra-axonal diffusion coefficient models into the ActiveAx and AxCaliber models, and more images will need to be collected to do so. Thus, for the experiments presented in this chapter, the ActiveAx and AxCaliber models were used assuming constant extra-axonal apparent diffusion coefficients.

6.2.6 Histology

Electron microscopy (EM) slices with 2000x magnification were studied (10 in total) from the region of the corpus callosum above the corresponding MR image slice, as shown by the blue box in Figure 6.5.

Axon diameters were manually measured using ImageJ software (National Institutes of Health, Bethesda, Maryland) by drawing lines across the smallest diameter perpendicular to the cells that could be identified as axons (Figure 6.6). A grid was used to divide the slice in sections and for ease in performing the measurements. The entire slice was examined and the measurements

were taken on all structures that were determined to be axons. Table 6.1 shows the number of measurements taken on each EM slice. For each slice, two sets of measurements were taken. For the first set, the measurements were taken by drawing the line across the smallest diameter of the cells, as shown in Figure 6.6a. The second set of measurements were taken by drawing a different line and much larger than the first set and are drawn on top of the first set of measurements, as shown in Figure 6.6b. This second set of measurements was added to the first set of measurements to see if changing the direction of the measurement and/or having a larger measurement would agree more with the MR results. Doing so would take into account the axons not being exactly perpendicular to the gradient during imaging (see Section 6.4). Table 6.1 shows the total number of measurements taken on each EM slice and the corresponding mean axon diameters (mean \pm standard deviation) for the first set of measurements. . This first measurement set was used in the comparisons with the MR data, and were used to calculate the final results.

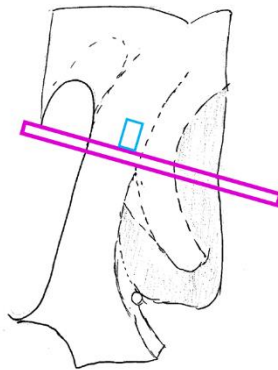


Figure 6.5: Slice selection (blue box) for EM of the corpus callosum was taken above the corresponding MR image slice (magenta box)

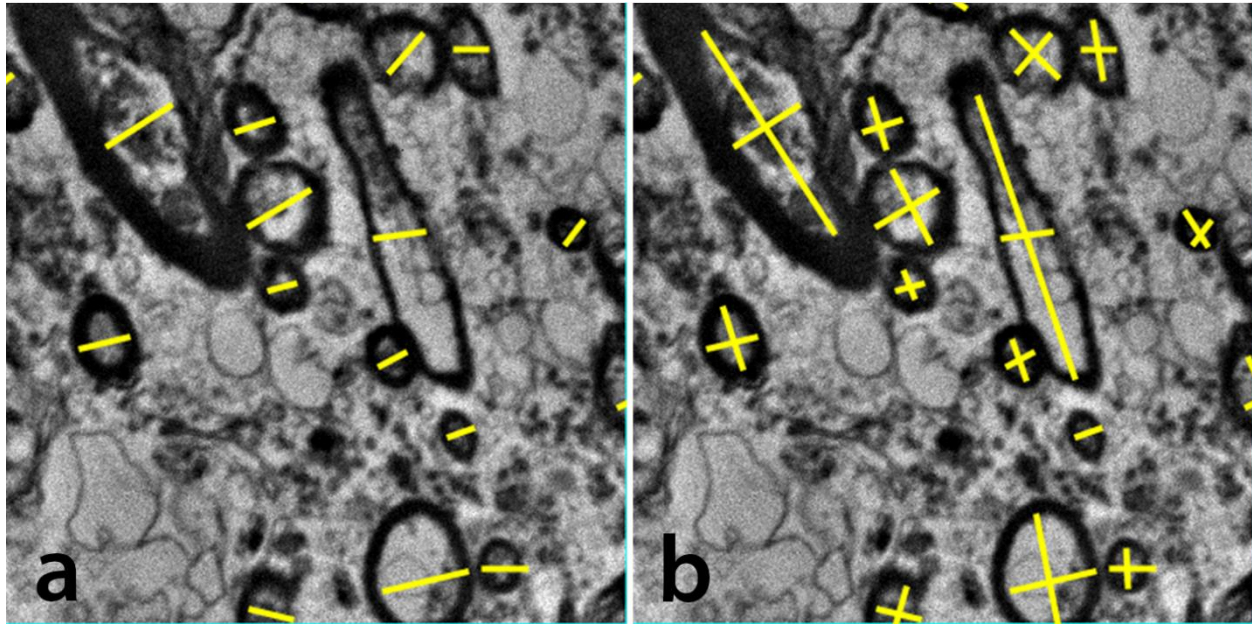


Figure 6.6: Measurements of axon diameters taken on EM images. (a) First set of measurements were taken on the smallest diameter of the cell. (b) Second set were measurements taken on the largest diameter of the cell and included in the first set of measurements. The yellow lines represent the lines drawn to make the axon diameter measurements. Note that in (b) each axon has two yellow lines, one representing the smallest diameter from (a), and the other the largest diameter of the cross section of the axon.

Table 6.1: Total number of measurements for each EM image slice and the mean axon diameters of each slice (mean \pm standard deviation) for the first set of measurements.

Slice	# of measurements	Mean axon diameter (μm)
1	704	0.7 ± 0.4
2	686	0.7 ± 0.4
3	665	0.8 ± 0.4
4	638	0.8 ± 0.4
5	593	0.8 ± 0.5
6	652	0.8 ± 0.4
7	600	0.8 ± 0.4
8	577	0.8 ± 0.4
9	564	0.8 ± 0.5
10	606	0.8 ± 0.4
overall average diameter (mm)		0.8 ± 0.4

6.3 Results

This section stated the results of the fits of the signal to the model for each of the ROIs. It also presented the results of the histological analysis in a similar form to the MR results. The results of both histological analyses are presented for only the corpus callosum in comparison with the MR data which will be made in the discussion section.

6.3.1 MR / Fit Results

Using the ActiveAx [13] model (Equation (3.37)), the calculated fitted mean effective diameter for axons in the ROIs in the corpus callosum ranged from $1.8 \pm 0.1 \mu\text{m}$ to $2.34 \pm 0.04 \mu\text{m}$, with an average of $2.0 \pm 0.2 \mu\text{m}$. The mean effective diameter for ependymal cells in the ROIs in the ependymal layer ranged from $2.58 \pm 0.06 \mu\text{m}$ to $2.80 \pm 0.06 \mu\text{m}$. No consistent results for the cortex were found which indicated the model was unable to find a reliable result. This was expected because the cells in the cortex do not resemble the parallel cylinders that this model assumes. A table of the effective mean axon diameter (AxD) results can be found in Table 6.2.

Using the AxCaliber [7] model (Equation (3.33)), the axon diameter distribution indicated that the size of axons in the corpus callosum ranged from 0.9 to 3 μm , whereas histological measurements indicated that the diameter of axons in the corpus callosum ranged from $0.14 \pm 0.02 \mu\text{m}$ to $6.00 \pm 0.02 \mu\text{m}$.

Table 6.2: The fitted effective mean diameters (AxD) for each ROI within the human brain sample, consisting of the corpus callosum (CC), ependymal layer (EL), and cortex (CX). Overall average of the ROIs in the corpus callosum only was $2.0 \pm 0.2 \mu\text{m}$.

Region	ROI	Mean Diameter (μm)
CC	1	2.34 ± 0.04
	3	2.24 ± 0.06
	5	2.06 ± 0.06
	7	1.87 ± 0.09
	8	1.9 ± 0.1
	9	1.8 ± 0.1
EL	2	2.86 ± 0.06
	4	2.88 ± 0.05
	6	2.58 ± 0.06
CX	10	*
	11	*
	12	*

* model unable to find result

6.3.2 Histology Results

The measurements made on the EM image slices (Section 6.2.6) of the corpus callosum found axon diameters in the range of 0.14 to $6 \mu\text{m}$, with an average overall of $0.8 \pm 0.4 \mu\text{m}$, which is consistent with other histology measurements [14]. Using Equation (3.37), the calculated AxD of the histological samples was found to be $1.43 \pm 0.02 \mu\text{m}$. Comparing this result to the MR images, the fitted AxD ranged from $1.8 \pm 0.1 \mu\text{m}$ to $2.34 \pm 0.04 \mu\text{m}$ with an average of $2.0 \pm 0.2 \mu\text{m}$. The fitted AxD from the MR images is almost $0.4 \mu\text{m}$ to $1 \mu\text{m}$ higher than the AxD measured from histology.

6.4 Discussion

The MR inferred AxD was larger than the measured AxD from histology. Measurements indicating diameters which were larger than the actual diameter are possible if the MR imaging gradient was not completely perpendicular to the axons. Thus a second set of measurements was taken on the histological sample in order to determine if the gradient direction which was not perpendicular to the axons could account for the larger diameters. Results are shown in Table 6.3. The average axon diameters increased but not enough such that the gradient direction alone could not account for this difference. On the other hand, the AxD from this second set of measurements increased drastically to $5.52 \pm 0.02\mu\text{m}$. This value is much larger than any AxD found with MRI. This indicates that angle has a large effect on AxD. If the histology was not performed at the exact same angle as the gradient, the diffusion which the water molecules experienced could be more different. A careful analysis will be needed in the future to ensure that the angles in the histology match as closely as possible with the MR acquisition.

Table 6.3: Second set of measurements from EM images of axon diameters (mean \pm standard deviation)

Slice	# of measurements	Axon diameter (μm)
1	1376	1.1 ± 1.2
2	1352	1.1 ± 1.1
3	1301	1 ± 1
4	1259	1.3 ± 1.3
5	1151	1.3 ± 1.5
6	1281	1.3 ± 1.2
7	1197	1.4 ± 1.4
8	1140	1.4 ± 1.3
9	1125	1.4 ± 1.3
10	1203	1.4 ± 1.2
overall average diameter (mm)		1.3 ± 1.3

One thing to note is that the sine-OGSE method was mistakenly used instead of the apodised cosine-OGSE method. This user error could be avoided in the future with improvements to the coding of the pulse sequence.

Another thing to note is that the region of the corpus callosum was different in the EM images from the MR images. The EM images were taken in a region above the MR imaging slice and therefore the direction of the axons could be different in these. That being said, the EM sections were taken to match the direction of the imaging plane as closely as possible. Any variation could cause small changes in the angle of the EM images and MR images and thus in the relative difference in axon diameter measurements. While there was no significant difference between the AxD measured histologically in the 10 slices, slices 1 and 2 had a slightly smaller AxD than in the other slices. Thus it is also possible for the axon diameters to vary with position and thus to be different in the MR image and in the histological images. Axons are not parallel cylinders, and therefore it was also possible that for the position of the image the axons could have been at many different angles to the image plane.

These results indicate this method is sensitive to axons in the 2 μm range which is smaller than previous measurements [5, 6, 13, 15]. It is possible that the MR method could not detect axons much different than 2 μm and thus these measurements are only of the axons in the 2 μm range. Higher gradient frequencies will be needed for future studies to probe even smaller diameters and more work needs to be done to optimize the choices of gradient amplitudes, gradient frequencies, and SNR to make a method which can be used on live animals. A frequency-varying extra-axonal diffusion coefficient should be studied with this model.

Nonetheless, detecting these smaller axons which constitute the majority of cortical connections [16] makes these measurements clinically relevant. This is the first step toward inferences of micron-sized axon diameters in the human corpus callosum. Chapter 7 will discuss some of the needed improvements to this method so it can become clinically relevant.

6.5 Conclusions

Micron-sized axon diameters in human corpus callosum were inferred using OGSE diffusion spectroscopy. The mean effective diameter (AxD) for axons in the corpus callosum in the selected regions of interest ranged from: $1.8 \pm 0.1 \mu\text{m}$ to $2.34 \pm 0.04 \mu\text{m}$ with an average of $2.0 \pm 0.2 \mu\text{m}$. The AxD for ependymal cells in the ependymal layer ranged from $2.58 \pm 0.06 \mu\text{m}$ to $2.88 \pm 0.06 \mu\text{m}$. Using MRI, axons were found to range between $0.9 \mu\text{m}$ and $3 \mu\text{m}$. From the histological techniques performed on the corpus callosum, this gave axon diameters ranging from $0.14 \pm 0.02 \mu\text{m}$ to $6.00 \pm 0.02 \mu\text{m}$, with an average overall of $0.8 \pm 0.4 \mu\text{m}$. The calculated AxD for axons in the corpus callosum found from histology was $1.43 \pm 0.02 \mu\text{m}$ if the measurement was made perpendicular to all axons. The calculated AxD rose to $5.52 \pm 0.02 \mu\text{m}$ if the measurement angle relative to the axons was allowed to vary. Based on these results, this is the first step toward inferences of micron-sized axon diameters *in vivo*.

References

1. E. Luders, P. M. Thompson, and A. W. Toga, "The development of the corpus callosum in the healthy human brain," *Journal of Neuroscience*, vol. 30, no. 33, pp. 10985-10990, 2010.
2. Queensland Brain Institute - The University of Queensland (2017, November). *Corpus Callosum* [Online]. Available: <https://qbi.uq.edu.au/brain/brain-anatomy/corpus-callosum>
3. F. Aboitiz, A. B. Scheibel, R. S. Fisher, and E. Zaidel, "Fiber composition of the human corpus callosum," *Brain Research*, vol. 598, no. 1, pp. 143-153, 1992.
4. E. Luders and A. W. Toga, "Chapter 9 - Sex Differences in Brain Anatomy," in *Progress in Brain Research*, I. Savic, New York: Elsevier, 2010, vol. 186, pp. 2-12.
5. D. C. Alexander, P. L. Hubbard, M. G. Hall, E. A. Moore, M. Ptito, G. J. M. Parker, T. B. Dyrby. "Orientationally invariant indices of axon diameter and density from diffusion MRI," *NeuroImage*, vol. 52, no. 4, pp. 1374-1389, 2010.
6. Y. Assaf, T. Blumenfeld-Katzir, Y. Yovel, and P. J. Basser, "AxCaliber: a method for measuring axon diameter distribution from diffusion MRI," *Magnetic Resonance in Medicine*, vol. 59, no. 6, pp. 1347-1354, 2008.
7. M. Mercredi, T. J. Vincent, C. P. Bidinosti, and M. Martin, "Assessing the accuracy of using oscillating gradient spin echo sequences with AxCaliber to infer micron-sized axon diameters," *Magnetic Resonance Materials in Physics, Biology and Medicine*, vol. 30, no. 1, pp. 1-14, Feb 2017.
8. K. M. Matsuda, A. Lopes-Calças, T. Magyar, Z. O'Brien-Moran, R. Buist, M. Martin, "Ex vivo tissue imaging for radiology-pathology correlation: a pilot study with a small bore 7-T MRI in a rare pigmented ganglioglioma exhibiting complex MR signal characteristics associated with melanin and hemosiderin," *Journal of Medical Imaging*, vol. 4, no. 3, p. 036001, 2017.
9. M. Schachter, M. D. Does, A. W. Anderson, and J. C. Gore, "Measurements of restricted diffusion using an oscillating gradient spin-echo sequence," *Journal of Magnetic Resonance*, vol. 147, no. 2, pp. 232-237, Dec 2000.
10. M. D. Does, E. C. Parsons, and J. C. Gore, "Oscillating gradient measurements of water diffusion in normal and globally ischemic rat brain," *Magnetic Resonance in Medicine*, vol. 49, no. 2, pp. 206-215, Feb 2003.
11. J. D. Thiessen, Y. Zhang, H. Zhang, L. Wang, R. Buist, M. R. Del Bigio, J. Kong, X.-M. Li, and M. Martin, "Quantitative MRI and ultrastructural examination of the cuprizone mouse model of demyelination," *NMR in Biomedicine*, vol. 26, no. 11, pp. 1562-1581, 2013.

12. S. L. Herrera, M. Mercredi, R. Buist R, and M. Martin. “Inferring diameters of spheres and cylinders using interstitial water”. *Magnetic Resonance Materials in Physics, Biology and Medicine*. 2018. <https://doi.org/10.1007/s10334-018-0685-9>
13. J. Xu, H. Li, K. D. Harkins, X. Jiang, J. Xie, H. Kang, M. D. Does, “Mapping mean axon diameter and axonal volume fraction by MRI using temporal diffusion spectroscopy,” *NeuroImage*, vol. 103, pp. 10-19, Dec 2014.
14. D. Liewald, R. Miller, N. Logothetis, H.-J. Wagner, and A. Schüz, “Distribution of axon diameters in cortical white matter: an electron-microscopic study on three human brains and a macaque,” *Biological Cybernetics*, vol. 108, no. 5, pp. 541-557, 2014.
15. E. C. Parsons, M. D. Does, and J. C. Gore, “Temporal diffusion spectroscopy: Theory and implementation in restricted systems using oscillating gradients,” *Magnetic Resonance in Medicine*, vol. 55, no. 1, pp. 75-84, 2006.
16. G. Innocenti, R. Caminiti, and F. Aboitiz, “Comments on the paper by Horowitz et al.(2014),” *Brain Structure and Function*, vol. 220, no. 3, p. 1789, 2015.

Chapter 7

Conclusions and Future Directions

This chapter summarizes the results of the experiments described in this thesis. Proposals are made for improvements for future experiments. Suggestions are proposed for future improvements to the model for more accurate descriptions of tissues.

7.1 Conclusions

The experiments in this thesis demonstrated the ability of models to take advantage of the oscillating gradient spin echo (OGSE) sequences to infer micron level restriction sizes.

The initial experiments in Chapter 4 guided the selection of pulse sequence and imaging parameters to give an idea of the parameters needed for measuring micron-sized restrictions. Measurements were made on water diffusing between 3 μm polystyrene spheres. The gradient frequencies and amplitudes used were appropriate to infer the 3 μm bead pore sizes of 0.6 ± 0.5 μm corresponding to bead diameters ranging from 3 ± 2 μm to 5 ± 4 μm . However the large uncertainties in these values suggested a better signal-to-noise (SNR) ratio would be required to help make the results more accurate. Measurements made on the water diffusing inside various tubes indicated the gradient frequency range was not appropriate for inferences of the diameter of the tubes that were 250 μm and larger.

The second set of experiments in Chapter 5 used the information from the first set to choose the imaging and gradient parameters for measurements of water diffusing between 3, 6, and 10 μm beads, and also in the 150 μm tubes. This method showed its ability to infer the bead and tube diameters in these experiments. For the bead phantom experiments, pore sizes of $0.60 \pm 0.08 \mu\text{m}$, $0.54 \pm 0.06 \mu\text{m}$ and $1.0 \pm 0.1 \mu\text{m}$ which corresponded to bead diameters of $2.9 \pm 0.4 \mu\text{m}$ to $5.3 \pm 0.7 \mu\text{m}$, $2.6 \pm 0.3 \mu\text{m}$ to $4.8 \pm 0.6 \mu\text{m}$, and $4.9 \pm 0.7 \mu\text{m}$ to $9 \pm 1 \mu\text{m}$. For the tube phantom experiment, the inferred surface-to-volume ratio of $0.06 \pm 0.02 \mu\text{m}^{-1}$ corresponded to a tube diameter of $180 \pm 70 \mu\text{m}$. From these experiments, the results indicated that the method had a resolution limit which was greater than 0.5 μm given that the pore sizes between the 3 μm and 6 μm beads were indistinguishable. When comparing the inferences made in the bead experiments to the tube experiments, there were more accurate inferences on the diameters of the beads rather than in the diameters of the tubes. This suggests that this method is better optimized for the micron-sized samples used in the beads, rather than the 150 μm size samples of the tubes.

The final experiment tested the method on a portion of the human corpus callosum (Chapter 6). Using the ActiveAx method, the mean effective diameter (AxD) for axons in the corpus callosum ranged from $1.8 \pm 0.1 \mu\text{m}$ to $2.34 \pm 0.04 \mu\text{m}$ in the regions of interest selected. The AxD for ependymal cells in the ependymal layer ranged from $2.58 \pm 0.06 \mu\text{m}$ to $2.88 \pm 0.06 \mu\text{m}$. Histological measurements gave a calculated AxD of $1.43 \pm 0.02 \mu\text{m}$. A second round of histological measurements which represented diffusion at an angle much different from perpendicular to the axons gave a calculated AxD of $5.5 \pm 0.02 \mu\text{m}$. Using the AxCaliber method, axons were found to range between 0.9 μm and 3 μm with MRI. Using the histological measurements in the EM slices of the corpus callosum, showed axon diameters in the range between $0.14 \pm 0.02 \mu\text{m}$ and $6 \pm 0.02 \mu\text{m}$, with an average overall of $0.8 \pm 0.4 \mu\text{m}$. The results

suggest that the resolution limit of the method needs to be decreased and careful attention could be given to the axon direction when selecting the regions needed for both the MR image and EM image data.

7.2 Improvements for Future Experiments

In this section, several suggestions for improvements to future experiments are described. These suggestions are based on problems observed when performing the experiments presented in this thesis. As explained below, the inclusion of a water tube, a means to reduce water evaporation, temperature control, a means to secure the sample in the magnet bore, more sample monitoring during long imaging sessions, better preparation of samples, a better understanding of the resolution limit, and improved coding of the pulse sequence, are all discussed in this section to improve future experiments.

7.2.1 A Water Tube

Ensuring a water tube is visible in the image allows for a control ROI to verify the water diffusion coefficient is as expected. Variations in the water diffusion coefficient with time or frequency indicated problems with the images such as temperature fluctuations (see Section 7.2.3), evaporation (see Section 7.2.2), Larmor frequency drift, movement of the sample or the coil, eddy currents, etc. It could be possible to correct for the Larmor frequency drift and movements, and the water sample could be used to verify the correction.

In Chapter 4, rather than including an extra water tube which would increase the field of view and thus decrease the resolution of the image, the sample tube was oriented in such a way so that the top part of the tube contained pure water while the bottom part of the tube contained beads packed in water. Several problems occurred with this method. The sample tube was too large to fit in the radiofrequency (RF) coil vertically. Instead it was placed at an angle which caused the beads to drift in the sample and become less packed. If future samples are made this way, the sample tubes must be small enough to stand vertically in the RF coil. Also, as observed in some of the experiments presented in this thesis, and later discussed in Section 7.2.4, during the long imaging sessions, the sample tube within the RF coil moved. This motion caused the tube to tip over or shake, changing the packing of the beads and the bead-water boundary. Thus, if imaging sessions are long enough for these types of problems, it is suggested that future experiments separate the beads from the water with the use of a water tube.

7.2.2 Evaporation of Water

In Chapter 5 sample tubes filled with water were tested. For the most part, this was an improvement for the control region especially when it was easy to find an imaging plane that contained the sample tube(s) and the water tube, however there were still two main flaws with this approach. The first was that the water tube should be carefully sealed to prevent any evaporation. The sample tubes also tended to have some form of evaporation which made the sample useless over time despite being sealed. Either better seals are needed for the sample tubes or a very small layer of water is needed at the top of the sample tube while carefully avoiding the problems discussed in Section 7.2.1. Another problem would be the addition of the

extra tube that has the possibility of increasing the field of view of the image which would in turn potentially decrease the resolution.

7.2.3 Temperature

While there is a simple relationship between the diffusion coefficient of water and temperature [1] there is no known simple relationship in a complex sample. Thus corrections for temperature variations are not easy to make. Therefore it is important to keep the temperature of the sample constant. A temperature probe near the sample could give a better indication of any temperature fluctuations during the experiment. Proper and consistent recording of the temperature during the entirety of the experiment is also recommended. Also a more sophisticated system could be used where the temperature probe provides feedback to a heating or cooling system to maintain the temperature.

7.2.4 Securing the Sample in the Magnet Bore

Image registration and visual inspection both suggested that some of the phantoms/samples moved significantly during the imaging sessions. There were several possible reasons for this motion and all can be prevented with repairs to the hardware. The RF coil has a locking mechanism which should keep the coil in place within the gradient coil. Unfortunately, this locking mechanism was broken for all of the experiments presented in this thesis. To remedy this, an attempt to secure the coil to the gradients was done by inserting tape and paper, but this

obviously was not strong enough to withstand the vibrations from the gradient during the experiment. This locking mechanism in the coil should be fixed for future experiments.

The gradient coil itself also caused sample motion. The weight of the cables coming from the gradient coil caused the RF coil housing the sample to tilt during the experiments. This was because the gradient coil cables were coming out of the same end of the bore as the cables from the RF coil. It is also possible that vibrations from the gradient pulses caused motion. Future experiments could find a way to hang the gradient cables in such a way that they do not pull the gradient coil off-balance. For experiments described in this thesis, systematic corrections were applied to the data so that the error in the end was a small fraction of a voxel.

7.2.5 Monitoring Sample and Imaging throughout the Experiment

So far Section 7.2 detailed several scenarios that can go wrong with the sample and the images during the course of an experiment. For days-long imaging sessions, like the ones presented in this thesis, the probability of something going wrong is much higher than when compared to much shorter imaging sessions. Thus, the collection of images should be divided into short groups so the images could be monitored for signs of problems. In this thesis, each individual scan was set to be no longer than 35 minutes. The images are checked the images at least every 4-8 hours during the day and after 12 hours of overnight imaging. If the images showed signs of problems, such as large motion of the sample which cannot easily be corrected through image

registration, or loss of signal due to evaporation, the imaging session should be stopped and the problems fixed. This will allow some of the data to be usable before starting again.

7.2.6 Preparation of the Bead Phantoms

The sample tubes that housed the phantoms used for the bead experiments were centrifuge tubes with a tapered end. Cylindrical tubes with a consistent diameter are better suited for MRI experiments so that an imaging slice taken perpendicular to the tube could be made of any width. This would allow for all voxels to contain the same volume of the bead sample. This shape of tube would also reduce the cost of the sample, ensuring that all beads in the sample could be imaged and would reduce the wasting of the very expensive bead solution.

The bead solutions purchased from the suppliers to create the phantoms studied in the experiments detailed in this thesis were very dilute, ranging from 2.5% to 10% in concentration. Because of the concentration, the sample made from the bead solution of 2.5% solid had to be centrifuged between 27 and 33 times, adding new solution each time to make the beads closely packed and fill the sample tube. Whereas the 3 μm beads at 10% solid only needed to be centrifuged 4 times. Increasing the speed of centrifuge to a higher speed (from 5000 to 12,000 rpm) caused the centrifuge tube to break and therefore the lower speed was used to prevent any breakage. In addition, obvious layering or inconsistent packing of the beads was visible in the samples which was caused from the multiple centrifuging and the extra solution being added each time. This layering indicated that there could be gaps or holes within the sample, and more importantly the packing was not uniform throughout the sample. Thus, the model used to describe the phantom was not correct and could result in inaccurate inferences of diameters.

More concentrated solutions of beads could not be found for the experiments in this thesis.

Future experiments should consider customized bead solutions to create the samples.

7.2.7 Preparation of the Tube Phantoms

The tubes with hollow inner sections could not successfully be filled in any way to perform experiments in this thesis. Many processes were attempted that failed. The final process might have succeeded in filling the tubes, but if it did, the volume fraction of water within the sample was too small to be detected with MRI.

Although the method of filling the tubes using the extension clamps made it easier to push the filtered water into the capillary tubes, there was no guarantee that the tubes actually filled entirely. Even if it were successful, the water within the tubes might have evaporated or come out when the 50 cm long tubing was filled, or when the tubing was eventually cut into the 2 cm pieces. With the total number of tubes that were packed into the sample tube (1341, in total), filling each 2 cm tube individually would be time consuming and there would be no guarantee that the tubes would still be full of water by the time all of them were filled.

These tubes were not soaked in filtered water as they were done in the first attempt as described in Section 4.3.1.1. Using the filtered water in lieu of the CuSO_4 might have worked better because if the water evaporated it would not leave behind residue to clog the tubing. If this was attempted, care should be taken to dry each piece of tubing so that there will be no water outside the cylinders in the sample at the time of the imaging experiment.

Even if the sample could be created with water inside the cylinders only, the volume fraction of the water appeared to be too small to detect with MRI for these 151 μm tubes. For instance, for 2 μm inner diameter tubes, the volume fraction of water in a tube is

$$\frac{\pi \cdot (2\mu\text{m})^2 \cdot \text{slice thickness}}{[\pi \cdot (151\mu\text{m})^2 \cdot \text{slice thickness}]} = \left(\frac{2}{151}\right)^2 = 1.75 \times 10^{-4}$$

For the 5 μm inner diameter tubes this increased to $\left(\frac{5}{151}\right)^2 = 1.1 \times 10^{-3}$.

And for the 10 μm inner diameter tubes $\left(\frac{10}{151}\right)^2 = 25 \cdot 1.75 \times 10^{-4} = 4.93 \times 10^{-3}$.

The volume fraction of water in the imaging slice would be much less than this because the packing fraction of the tubes in the sample was less than 100%.

For example, the packing fraction of 71.05% in the experiments presented in Chapter 5 resulted in a $0.7105 \cdot 1.1 \times 10^{-3} = 7.79 \times 10^{-4}$ volume fraction of water in those experiments which was too small to be detected by the MRI. Others have done experiments with the water inside the cylinders only [2, 3]. We have had conversations with these groups to understand how they were able to detect an MR signal from these samples. For instance, one group suggested removing some of the coating on the walls of the tubes to make the outer diameter of the tubes smaller so that more tubes could be packed into the sample. Determining the minimum volume fraction which would create a detectable and usable MR signal for these experiments would set a goal for this outer diameter. Although care should be used with these tubes because with thinner coating, the tubes are more fragile and could easily break. Further discussions and meetings with these groups should take place, or a collaboration should be formed if samples are needed with water inside the cylinders. While no other tubing was available for the experiments in this thesis,

another search for thinner tubes or custom-made tubes could provide another alternative to create the phantom.

The same type of sample tube that was used to house the bead phantoms in all the bead experiments was also used in the tube phantoms due to their availability. These sample tubes were tapered at one end, which caused varying packing fractions throughout the sample and the angle of the tubes within the sample to vary. Cylindrical tubes of consistent diameter or width are better suited for MRI experiments so that an imaging slice taken perpendicular to the tubes could be made of any width. This would allow for the voxels to contain the same volume within the tube phantom. It would also allow for the gradient direction to be perpendicular to all tubes in the phantom which was required for the model. This type of sample tube would also prevent the microcapillary tubes from breaking or bending because they could be inserted all in the same direction and be parallel to one another.

Given that the packing fraction is an important piece of information used to relate the parameters from the fit it is necessary to calculate this packing fraction carefully. In addition to using cylindrical sample tubes rather than the tapered tubes when making the phantom, it is necessary to count the total number of tubes so that an exact number can be used in the calculations for packing fraction for all future experiments.

7.2.8 Resolution Limit of the Method

Three bead diameters, 3 μm , 6 μm , and 10 μm , were tested in the experiments in this thesis. The sizes of the pores between the 3 μm and 6 μm beads were indistinguishable with this method.

More bead samples with varying diameters should be studied to obtain a more accurate measure of the upper and lower resolution limit and to confirm that the pore radius and bead radius of the sample has a linear relationship.

To understand the resolution limit better, further experiments could be performed to improve the resolution limit using different gradient frequencies. A relationship between resolution limit and gradient frequencies could be obtained so that when planning an experiment to infer sample sizes in a known range, the selection of gradient frequencies could be easily chosen.

White matter in the brain will not have axons all of the same diameter, which was observed in the histology measurements in Chapter 6. Thus a single phantom containing beads of many different diameters could be studied to determine if the distribution of bead diameters could be found. The number and range gradient frequencies and amplitudes could be optimized for different distributions of diameters.

7.2.9 Preparation of the Brain Sample

For future experiments using brain samples, preparation should be done in a similar fashion to other samples used for imaging in this lab [4]. For instance, markers that are visible in the histological images and the MR images can be used so that the histology and MR image planes can be aligned and the depth of tissue processing and angle of tissue cutting can easily be found [4]. A neuropathologist should be consulted to choose the direction of the slice and gradient so that a slice can contain a uniform amount of corpus callosum and the gradient direction can be chosen perpendicular to the axons. Section 7.3 discusses changes to the model that would more closely match the tissue, given that, clearly within this sample the axons were not perfect parallel cylinders required for the ActiveAx and AxCaliber methods.

If the axon diameter variation with position is determined to be small, or not of importance to the study, larger ROIs should be chosen so that a signal with more precise SNR could be used in the fits to infer axon diameter. This could be done in a similar fashion to the 3 μm bead sample explained in Chapters 4 and 5, or to have a simple ROI for each region in the brain sample, where the entire corpus callosum can be encompassed using a single ROI. The neuropathologist should be consulted to define the ROIs to ensure the regions correspond to those that are important for the study. In addition to larger ROIs, if position dependence of axon diameters is not of interest, larger slice thicknesses could be used to obtain better SNR for more accurate results.

7.2.10 Improvements to the Coding of the Pulse Sequence

The code which allows the MRI machine to run OGSE sequences could be improved. For instance, in its current form, we did not have access to the b-value calculator. This meant that gradient values and b-values had to be calculated manually. If the Bruker Paravision code could include OGSE sequences, b-values could be calculated automatically. This would also help with data collection. Ideally the images collected to calculate the ADC at any given frequency would be spaced evenly in b. In fact, it would be best if all frequencies used the same b . Thus if b-values could be entered into the code rather than gradient amplitudes, this could easily be done. If the highest and lowest b-values could be selected as well as the number of b-values to be used for a given frequency, having the code automatically calculate the b-values so they are evenly spaced would reduce the user error in the experiments.

Another automated part of the code is the addition of multiple periods to the code. The user could specify the number of gradient periods as well as which periods to use in one scan. This would help to avoid user error. The method for creating sinusoidal waves in the Paravision code is to specify amplitudes as a function of time. In order to ensure the gradients end with an amplitude of 0 and the sine waves on either side of the cosine wave in the apodised cosine wave form start at 0 and end at 1, the number of points per period must be a multiple of 4 times the number of periods (re: Appendix B). The code currently has the number of points entered manually so it is subject to user error. I suggest when the new version of the OGSE sequences is released in Paravision that the number of points is calculated automatically.

7.2.11 Quality Assurance

Students should be careful when drawing the noise ROI to ensure that it is in a proper region of the background. Adjusting the contrast and brightness of the image so that the artefacts such as ghosting are visible should help when placing the ROI.

B_0 inhomogeneities should not have a large effect on the measurements because of the symmetric nature of the pulse sequence [5], and careful shimming. The use of a volume birdcage RF coil on a small sample should reduce the effects of B_1 inhomogeneities on the measurements [6]. Nonetheless, the effects of these inhomogeneities can be studied using a large water tube sample and calculating an ADC pixel map over the entire sample. Lack of uniformity could give an indication of any errors due to these inhomogeneities and other effects.

7.2.12 Considerations for Live Brain Experiments

The experiment performed in Chapter 6 used formalin-fixed tissue. Formalin cross-links proteins. After formalin is removed, these cross-links remain. This caused the ADC to be lower and more uniform between the tissues with formalin treatment than without treatment [7, 8].

Also the experiments in Chapter 6 were performed at room temperature where the ADC of free water is approximately $2 \mu\text{m}/\text{ms}^2$. For live brain measurements, the experiments were performed at body temperature (37°C) at which the ADC of the free water is $3 \mu\text{m}/\text{ms}^2$, and thus even smaller frequencies will be needed [1]

7.3 Improvements to the Model

The models used in these experiments assume two compartments with no exchange between compartments. In the full AxCaliber and ActiveAx models, axons are assumed to be parallel, impermeable cylinders [9, 10]. Extra-axonal water is incorrectly assumed to have a constant hindered diffusion coefficient with diffusion time or frequency [9, 10]. These models are obviously flawed when describing white matter. Although changing the model for a more accurate description of the tissue will introduce more fit parameters in the fit which could make the precision and/or accuracy of the inferences of axons worse. Thus, careful study is needed of more complex models to determine if the complexity provides more accurate results. This section describes some possible additions and changes to the model which could be studied.

7.3.1 Axon Orientation Dispersion and Axon Undulation

Axons are not long parallel cylinders. At the International Society for Magnetic Resonance in Medicine (ISMRM) Workshop on Diffusion as a Probe of Tissue Microstructure Workshop, in 2013, one plenary talk showed 3D detailed EM images of white matter [11]. It was shown that axons are more like a twisted tangled mess. To account for this in the model, others have changed the term in the exponential to account for the signal from the intra-axonal diffusion, which will allow for an angle distribution rather than a fixed angle of 90^0 [12]. With pulse gradient spin echo (PGSE) sequences, it has been shown that the model for axon dispersion overestimates the axon diameters because water molecules have time to sample one or more complete undulations (tens of microns) during the diffusion time, so that the effective restriction

length is actually larger than the axon diameter [13, 14]. Switching to OGSE should shorten the diffusion time enough to overcome this problem. Some axons vary in diameter, such as the optic nerve which varies up to a factor of two in diameter over a distance of 12 μm [13, 15]. A similar argument can be made for the improvement in accuracy of the diameter inferences when OGSE is used for such axons. It is thus expected that the resolution limit of these methods should be reduced when switching from PGSE to OGSE.

7.3.2 Shortening Imaging Time Toward A Clinically Relevant Time

The measurements presented in this thesis required a lot of imaging time for high precision. In the clinic, short imaging times are desired so that more people can be imaged in a single day, and also those that are ill do not experience the discomfort of long imaging sessions. Thus shorter imaging times are desired.

For the second bead experiments, images were collected with poor resolution which allowed for a high SNR and thus fewer images were collected and averaged in order to find more precise sizes in the sample. It is possible that collecting fewer images using fewer gradient strengths, fewer OGSE frequencies, fewer averages and, as we saw in Chapter 5, less resolution could provide similar or better precision in a shorter amount of time. Other studies were conducted in the Martin lab using some of the data presented in this thesis [16-20]. These studies indicated that fewer images can be collected without significantly altering the precision of the results.

Thus the next set of experiments would aim to find the optimized set of frequencies and gradient strengths for the expected sizes in a given sample or phantom.

Other studies in the Martin lab examined the effects of noise on the precision of the results [16, 17]. The ultimate goal is to optimize the method for each sample depending on the diameters of axons in that sample and the precision at which the measurements need to be made. The SNR had a strong effect on the precision of smaller axons ($\sim 1\mu\text{m}$) and less of an effect on the precision of larger axons ($\sim 3\mu\text{m}$). It is possible that with a different, higher range of frequencies, the SNR would have less of an effect on the $\sim 1\mu\text{m}$ axons. Being able to use lower SNR would allow either for shorter imaging times or for higher resolution.

7.3.3 Diffusion Tensor Imaging (DTI)

Diffusion tensor imaging (DTI) and the diffusion tensor can be measured to find the direction of fibres in the brain (Section 3.3.3). Given that there is axon dispersion and undulation, the different directions of the gradient in each voxel would be needed if the desire to have a gradient perpendicular to all the axons in a particular voxel. The experiment in Chapter 6 gave an indication of how difficult it is to get the gradient direction perfectly perpendicular to the axons. Using DTI the principal diffusion directions can be found in each voxel to allow for easy discovery of the perpendicular direction in each voxel. Data in each voxel from the perpendicular direction could be studied to infer axon diameters.

7.4 Final Conclusions

This thesis presented a method to infer micron-sized restrictions in samples. The final chapter discussed a means to shorten imaging time so the method might one day be clinically useful. In this chapter several methods and suggestions for future work and improvements to the experiments and data analysis were described.

References

1. M. Holz, S. R. Heil, and A. Sacco, "Temperature-dependent self-diffusion coefficients of water and six selected molecular liquids for calibration in accurate ^1H NMR PFG measurements," *Physical Chemistry Chemical Physics*, 10.1039/B005319H vol. 2, no. 20, pp. 4740-4742, 2000.
2. -H. Li, J. C. Gore, and J. Xu, "Fast and robust measurement of microstructural dimensions using temporal diffusion spectroscopy," *Journal of Magnetic Resonance*, vol. 242, pp. 4-9, 2014.
3. B. Siow, I. Drobnjak, A. Chatterjee, M. F. Lythgoe, and D. C. Alexander, "Estimation of pore size in a microstructure phantom using the optimised gradient waveform diffusion weighted NMR sequence," *Journal of Magnetic Resonance*, vol. 214, pp. 51-60, 2012.
4. K. M. Matsuda, A. Lopes-Calças, T. Magyar, Z. O'Brien-Moran, R. Buist, M. Martin, "Ex vivo tissue imaging for radiology-pathology correlation: a pilot study with a small bore 7-T MRI in a rare pigmented ganglioglioma exhibiting complex MR signal characteristics associated with melanin and hemosiderin," *Journal of Medical Imaging*, vol. 4, no. 3, p. 036001, 2017.
5. X. Hong, W. T. Dixon, "Measuring diffusion in inhomogeneous systems in imaging mode using antisymmetric sensitizing gradients," *Journal of Magnetic Resonance*, vol. 99, pp. 561-570, 1992.
6. O. P. Yee, J. A. Nyenhuis, R. L. Strohine, "Magnetic field inhomogeneity effects on spin echo NMR diffusion measurements," *IEEE Transactions on Magnetics*, vol. 31, no. 6, pp. 3584-3586, 1995.
7. S.-W. Sun, J. J. Neil, H.-F. Liang, Y. Y. He, R. E. Schmidt, C. Y. Hsu, S.-K. Song, "Formalin fixation alters water diffusion coefficient magnitude but not anisotropy in infarcted brain," *Magnetic Resonance in Medicine*, vol. 53, pp. 1447-1451, 2005.
8. R. J. Dawe, D. A. Bennett, J. A. Schneider, S. K. Vasireddi, K. Arfanakis, "Postmortem MRI of human brain hemispheres: relaxation times during formaldehyde fixation." *Magnetic Resonance in Medicine*, vol. 61, pp. 810-818, 2009.
9. Y. Assaf, T. Blumenfeld-Katzir, Y. Yovel, and P. J. Basser, "AxCaliber: a method for measuring axon diameter distribution from diffusion MRI," *Magnetic Resonance in Medicine*, vol. 59, no. 6, pp. 1347-1354, 2008.
10. D. C. Alexander, P. L. Hubbard, M. G. Hall, E. A. Moore, M. Ptito, G. J. M. Parker, and T. B. Dyrby. "Orientationally invariant indices of axon diameter and density from diffusion MRI," *NeuroImage*, vol. 52, no. 4, pp. 1374-1389, 2010.
11. K. Zilles. "Visualization of Single Fibres & Fibre Tracts Using Ultra-High Resolution Polarizes Light Imaging," in *ISMRM Workshop - Diffusion as a Probe of Neural Tissue Microstructure*, Podstrana, Croatia, 2013.

12. M. Nilsson, S. Lasič, I. Drobňjak, D. Topgaard, and C.-F. Westin, “Resolution limit of cylinder diameter estimation by diffusion MRI: The impact of gradient waveform and orientation dispersion,” *NMR in Biomedicine*, vol. 30, no. 7, pp. e3711-n/a, 2017, Art. no. e3711.
13. M. Nilsson, D. van Westen, F. Stahlberg, P. C. Sundgren, and J. Latt, “The role of tissue microstructure and water exchange in biophysical modelling of diffusion,” *Magnetic Resonance Materials in Physics, Biology and Medicine*, vol. 26, no. 144, pp. 345-370, 2013.
14. M. Nilsson, J. Latt, F. Stahlberg F, D. van Westen, and H. Hagglatt, “The importance of axonal undulation in diffusion MR measurements: a Monte Carlo simulation study,” *NMR in Biomedicine*, vol. 25, no. 5, pp. 795-805, 2011.
15. J. A. Perge, K. Koch, R. Miller, P. Sterling, and V. Balasubramanian, “How the optic nerve allocates space, energy capacity, and information,” *Journal of Neuroscience*, vol. 29, no. 24, pp. 7917-7928, 2009.
16. M. Mercredi, T. J. Vincent, C. P. Bidinosti, and M. Martin, “Assessing the accuracy of using oscillating gradient spin echo sequences with AxCaliber to infer micron-sized axon diameters,” *Magnetic Resonance Materials in Physics, Biology and Medicine*, vol. 30, no. 1, pp. 1-14, Feb 2017.
17. M. Mercredi and M. Martin, “Toward faster inference of micron-scale axon diameters using Monte Carlo simulations,” *Magnetic Resonance Materials in Physics, Biology and Medicine*, pp. 1-20, 2018. <https://doi.org/10.1007/s10334-018-0680-1>
18. M. Mercredi, S. L. Herrera, R. Buist, K. Matsuda, and M. Martin, “Determining how varying the number of gradient strengths and frequencies affects fitted mean axon diameters in the corpus callosum using oscillating spin echo gradients”. in *ISMRM*, Paris, France, 2018.
19. M. Mercredi, S. L. Herrera, R. Buist, and M. Martin, “Determining surface to volume ratios in capillary tube samples using oscillating gradient spin echo sequences.” in *ISMRM*, Honolulu, HI. 2017
20. M. Mercredi, S. L. Herrera, R. Buist, and M. Martin, “Determining how varying the number of measured gradients affects fitted surface to volume ratios in tube samples using oscillating spin echo gradients.” in *ISMRM*, Honolulu, HI, 2017

List of Abbreviations

AD	Alzheimer's disease
ADC	apparent diffusion coefficient
ADC _e	apparent diffusion coefficient of the extracellular water
ADDs	axon diameter distributions
AxD	mean effective diameter
BCC	body centered cubic
CC	corpus callosum
CHARMED	composite hindered and restricted models of water diffusion
CNS	central nervous system
CSF	cerebrospinal fluid
CuSO ₄	copper sulfate
CX	cortex
DWI	diffusion-weighted imaging
EL	ependymal layer
EM	electron microscopy
FA	<i>Fractional anisotropy</i>
FCC	face centered cubic
FID	free induction decay
FOV	field of view
GEN	generalized waveforms
HARDI	high-angular-resolution diffusion imaging
HCP	hexagonal close packed
Hz	Hertz
ISMRM	International Society for Magnetic Resonance in Medicine
MRI	magnetic resonance imaging
MS	multiple sclerosis
NA	number of averages
NMR	nuclear magnetic resonance
OGSE	oscillating gradient spin echo
PBS	phosphate-buffered saline
PD	Proton density
PGSE	pulsed gradient spin echo sequence
RF	radio frequency
ROIs	Regions of interest
S/V	<i>surface-to-volume ratio</i>
SNR	signal-to-noise ratio

TE	the echo time
TR	repetition time
w/v	weight/volume

List of Symbols

B_0	external magnetic field
1H	nucleus of a hydrogen atom
μ	magnetic dipole moment
\vec{J}	angular momentum called spin
γ	gyromagnetic ratio (rads/sec)
$\bar{\gamma}$	gyromagnetic ratio (MHz/T)
f_0 or ω_0	Larmor frequency
\hbar	Planck's constant
I	nuclear spin quantum number
$R(\alpha)$	rotation matrix
\vec{M}	magnetization vector
M_z	Longitudinal magnetization
T_1	spin-lattice or longitudinal relaxation time
M_{xy}	transverse magnetization
T_2	spin-spin or transverse relaxation time
\vec{G}	gradient vector
\vec{r}	position vector
$S(t)$	signal
\vec{k}	k-space vector
$\langle s^2 \rangle$	mean squared displacement

n_d	spatial dimension in which motion is being studied
Δ	diffusion time
D	diffusion coefficient
ADC	apparent diffusion coefficient
k_b	Boltzmann constant
D_{free}	free self-diffusion coefficient
δ	gradient duration
g	gradient magnitude
ϕ	phase
ϵ	ramp rise time
λ_i	eigenvalues
ϵ_i	eigenvectors
$\lambda_{ }$	axial diffusivity
λ_{\perp}	radial diffusivity
FA	fractional diffusivity
b_{sin}	b-value for sine-OGSE
b_{cos}	b-value for ideal-cosine-OGSE
b_{acos}	b-value for apodised cosine-OGSE
$D(\omega)$	diffusion spectrum
r_{pore}	pore radius
D_0	intrinsic diffusion coefficient
g_{max}	maximum gradient strength

Appendix A

A.1 Schematic of the Experimental Setup

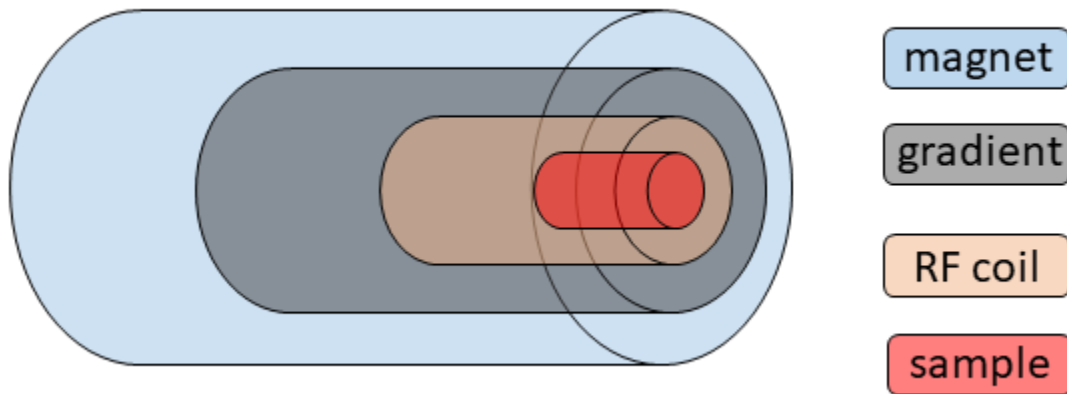


Figure A.1.1: Schematic of the 7T Bruker Magnet, BGA6 gradient insert, RF coil and sample. All experiments were performed using the 7T Bruker magnet. Phantoms and the brain sample were held within a sample tube/holder and then placed within the 3.5 cm RF coil. The BGA6 gradient set was locked into place within the 7T magnet. This BGA6 gradient set has a maximum gradient strength of $1.01 T/m$.

Appendix B

B.1 Calculation of Points

The gradient pulse is defined by a series of points spaced in time representing an amplitude that are needed to make the apodised cosine (or sine) wave. For a perfect wave, an infinite number of points should be used, however in Bruker, we can only change these points so quickly as described below.

Given a period n , we can calculate corresponding maximum number of points p , for each diffusion pulse length σ .

The number of points in a given time cannot be more than what the computer can handle to switch the gradient amplitudes. To ensure the gradients will not be switched faster than is possible, the time between points has to be greater than the minimum switching time of the gradients, which in Bruker is 0.01 ms. To ensure we are greater than this minimum switching time, we set our minimum switching time to 0.025 ms, so that the time between points t is

$$t = \frac{\sigma}{p} > 0.025 \text{ ms}$$

We need to also account for the $\frac{1}{4}$ period at the beginning and end of the apodised cosine wave because we need to ensure that the start and end of this $\frac{1}{4}$ period occurs at 1 and 0. Thus we need to have this maximum number be a multiple of 4. We also need to have the number of points be a multiple of the number of the periods such that (*# of points*) = $4N$.

To obtain the maximum number of points allowed for each diffusion pulse length:

$$\text{max points} = \sigma * \frac{1}{0.025 \text{ ms}} = \sigma * 40/\text{ms}$$

Therefore for a $\sigma = 20 \text{ ms}$ pulse the maximum number of points $\text{max points} = 20 \text{ ms} * 40/\text{ms} = 800 \text{ points}$. This is a multiple of 4 and a multiple of 1, so for the period of $n = 1$, we can use 800 points. For a period of $n = 3$, this 800 points is not a multiple of 3. The highest number below 800 that is a multiple of 3 is 792, which is what we used for the maximum number of points for a period of $n = 3$.

The following tables in the next sections show the parameters used in each of the experiments, showing the number of points chosen and the gradient strengths used for a given period.

B.1.1 Bead Phantoms and Microfluidic Device

Diffusion pulse length: $\sigma = 20 \text{ ms}$.

maximum *points* = $20 \text{ ms} * 40 = 800 \text{ points}$

periods (n)	points (p)	Gradient Strengths g_i (% of g_{\max})				
1	800	0	10	7	4	1.5
2	800	0	15	10	7	4
3	792	0	30	25	20	15
4	800	0	60	50	40	30
5	800	0	90	80	70	60
6	792	0	90	80	70	60
7	784	0	90	80	70	60
8	800	0	90	80	70	60
9	792	0	90	80	70	60
10	800	0	90	80	70	60
11	792	0	90	80	70	60
12	768	0	90	80	70	60
13	780	0	90	80	70	60
14	784	0	90	80	70	60
15	780	0	90	80	70	60
16	768	0	90	80	70	60
17	748	0	90	80	70	60
18	792	0	90	80	70	60
19	60	0	90	80	70	60
20	800	0	90	80	70	60

B.1.2 Microcapillary Pipettes

Diffusion pulse length: $\sigma = 60 \text{ ms}$.

maximum *points* = $60 \text{ ms} * 40 = 2400$ points

periods (n)	points (p)		Gradient Strengths g_i (% of g_{\max})			
1	2400	0	2.7	2.2	1.1	0.5
2	2400	0	3	2.7	2.2	1.1
3	2400	0	8	6	3.5	2.7
4	2400	0	12	8	6	3.5
5	2400	0	15	12	8	6
6	2400	0	17	15	12	8
7	2380	0	18	15	13	8
8	2400	0	20	17	15	10
9	2376	0	25	20	17	10
10	2400	0	30	25	20	15
11	2376	0	35	32	25	15
12	2400	0	37	31	25	15
13	2392	0	40	33	28	15
14	2352	0	42	36	30	20
15	2400	0	43	37	29	22
16	2368	0	46	39	30	22
17	2380	0	48	40	32	22
18	2376	0	50	44	34	22
19	2356	0	52	45	34	22
20	2400	0	55	47	38	25

B.1.3 Tube Phantom

Diffusion pulse length: $\sigma = 40 \text{ ms}$

maximum *points* = $40 \text{ ms} * 40 = 1600$ points

periods (n)	points (p)		Gradient Strengths g_i (% of g_{\max})			
1	1600	0	2.398	3.391	4.153	4.796
2	1600	0	4.633	6.552	8.025	9.266
3	1596	0	6.874	9.721	11.905	13.747
4	1600	0	9.115	12.891	15.788	18.231
5	1600	0	11.358	16.062	19.672	22.715
6	1584	0	13.600	19.233	23.556	27.200
7	1596	0	15.843	22.405	27.440	31.685
8	1600	0	18.085	25.577	31.325	36.171
9	1584	0	20.328	28.748	35.209	40.656
10	1600	0	22.571	31.920	39.094	45.142
11	1584	0	24.814	35.092	42.979	49.627
12	1584	0	27.057	38.264	46.863	54.113
13	1560	0	29.299	41.436	50.748	58.599
14	1568	0	31.542	44.607	54.633	63.084
15	1560	0	33.785	47.779	58.518	67.570
16	1600	0	36.028	50.951	62.402	72.056
17	1564	0	38.271	54.123	66.287	76.542
18	1584	0	40.514	57.295	70.172	81.028
19	1596	0	42.757	60.467	74.057	85.513
20	1600	0	45.000	63.639	77.942	89.999

B.1.4 Corpus Callosum

Diffusion pulse length: $\sigma = 20 \text{ ms}$

maximum *points* = $20 \text{ ms} * 40 = 800 \text{ points}$

periods (n)	points (p)		Gradient strengths g_i (% of g_{max})				
1	800	0	22.36	31.62	38.73	44.72	50
2	800	0	43.20	61.10	74.83	86.41	96.61
3	792	0	43.59	61.64	75.50	87.17	97.46
4	800	0	44.20	62.51	76.56	88.40	98.84
5	800	0	44.48	62.91	77.05	88.97	99.47
6	792	0	43.12	60.98	74.69	86.24	96.42
7	784	0	44.32	62.68	76.77	88.64	99.11
8	800	0	43.85	62.01	75.95	87.70	98.05
9	792	0	43.60	61.66	75.52	87.20	97.49
10	800	0	44.20	62.51	76.56	88.40	98.84
11	792	0	44.43	62.83	76.95	88.86	99.35
12	768	0	43.90	62.09	76.04	87.81	98.17
13	780	0	44.26	62.60	76.67	88.53	98.98
14	784	0	44.12	62.40	76.42	88.24	98.66
15	780	0	44.11	62.38	76.40	88.22	98.63